THE EFFECT OF WETTING TRANSPARENCY ON THE INTERFACIAL PHENOMENA BETWEEN WATER AND SOLID SURFACES: AN ATOMISTIC MODELING INVESTIGATION

A Dissertation
Presented to
The Academic Faculty

by

Bladimir Ramos-Alvarado

In Partial Fulfillment
of the Requirements for the Degree
Doctor of Philosophy in the
George W. Woodruff School of Mechanical Engineering

Georgia Institute of Technology
December 2016

THE EFFECT OF WETTING TRANSPARENCY ON THE INTERFACIAL PHENOMENA BETWEEN WATER AND SOLID SURFACES: AN ATOMISTIC MODELING INVESTIGATION

Approved by:

Dr. G. P. Peterson, Advisor
School of Mechanical Engineering
Georgia Institute of Technology

Dr. Satish Kumar, co-advisor
School of Mechanical Engineering
Georgia Institute of Technology

Dr. Zhuomin Zhang
School of Mechanical Engineering
Georgia Institute of Technology

Dr. Alexander Alexeev
School of Mechanical Engineering
Georgia Institute of Technology

Dr. Zhigang Jiang
School of Physics
Georgia Institute of Technology

Date Approved: June 27, 2016

To my mother†

ACKNOWLEDGEMENTS

I wish to thank Dr. G. P. “Bud” Peterson for giving me the opportunity of joining Georgia Tech and for his support through my PhD studies. I wish to thank Dr. Satish Kumar for his guidance while conducting my research and the rest of my committee for their significant input. I wish to thank the Mexican National Council on Science and Technology (CONACyT), the Mexican International Affairs Office, and the Goizueta Foundation for their economic support.

I wish to thank my wife Griselda Conejo-Lopez for her love and support throughout this experience; likewise, I want to express my gratitude to my son Isaac Ramos-Conejo for the many laughs and great times we had together that helped me forget the stress during the many difficult times I experienced. Son, you probably will not remember any of this, but someday, when you are old enough, I will share these experiences with you. I wish to thank Mrs. Valerie Peterson for her unconditional friendship, support, and guidance during my time at Georgia Tech. I wish to thank my good friend Daniel Lorenzini-Gutierrez for the many technical discussions we had during lunch time. Last but not least, I want to thank my good friends and neighbors from Tenth and Home, Family Housing.

TABLE OF CONTENTS

Page

ACKNOWLEDGEMENTS iv

LIST OF TABLES ix

LIST OF FIGURES x

LIST OF SYMBOLS AND ABBREVIATIONS xv

SUMMARY xvii

1 INTRODUCTION 1

1.1 Background and motivation 1

1.2 Review of concepts 6

1.3 Research objectives and summary of findings 9

1.4 Dissertation outline 12

2 LITERATURE SURVEY 14

2.1 Wettability modeling as a method for calibrating the solid-liquid interactions 14

2.1.1 Line tension effects in MD simulations of wettability 17

2.1.2 Calibration with experiments vs quantum calculations of the solid-liquid interaction potentials 19

2.1.3 Theoretical models of wettability 20

2.1.4 Experimental characterization of graphite and silicon surfaces 21

2.1.5 Summary of the literature review on wettability 22

2.2 Wettability transparency of graphene-coated surfaces 22

2.3 Hydrodynamics of nanoconfined liquids 24

2.3.1 Experimental investigations of hydrodynamic slip 25

2.3.2 Molecular mechanisms of hydrodynamic slip 30

2.3.3 Hydrodynamic slip dependence on surface wettability and roughness 32

2.3.4 Hydrodynamic slip dependence on shear rate 35

2.3.5 Hydrodynamic slip dependence on confinement size 37

2.3.6 Summary of the literature review on hydrodynamics of nanoconfined liquids 39

2.4 Solid-liquid interfacial thermal transport at the nanoscale 40

2.4.1 Effects of surface wettability (experimental investigations) 41

2.4.2 Effects of surface wettability (numerical investigations) 43

2.4.3 Effects of wall temperature (numerical investigations) 47

2.4.4 Theoretical model of thermal transport and wettability 48

2.4.5 Summary of the literature review on solid-liquid thermal transport 49

3 METHODS 51

3.1 Molecular dynamics 51

3.1.1 Overview of the method 52

3.1.2 Force calculation via empirical potentials 53

3.1.3 Integration of the equations 54

3.1.4 Thermostating 55

3.1.5 Periodic boundary conditions 55

3.1.6 Computational codes used 56

3.2 Water modeling 57

3.3 Atomistic modeling of wettability and postprocessing 59

3.3.1 Simulations set up 59

3.3.2 Postprocessing 60

3.4 Equilibrium and non-equilibrium modeling of the hydrodynamics of nanoconfined liquids 62

3.4.1 Equilibrium models for the calculation of hydrodynamic slip 62

3.4.2 Non-equilibrium modeling of nanoconfined liquid hydrodynamics 64

3.4.3 Simulations set up 65

3.5 Non-equilibrium modeling of thermal transport in nanoconfined liquids 66

3.5.1 Non-equilibrium MD modeling of thermal transport 66

3.5.2 Simulations set up 69

3.6 Summary 69

4 WETTABILITY OF GRAPHITIC CARBON AND SILICON SURFACES 71

4.1 A theoretical model of wettability based on the mean-field theory 71

4.2 Calibration of the atomic carbon-water interactions 76

4.3 Wettability of different silicon crystallographic planes 80

4.4 The wettability transparency of graphene-coated silicon surfaces 83

4.4.1 Macroscopic conditions required to observe wettability transparency 84

4.4.2 Microscopic conditions required to observe wettability transparency 86

4.5 Summary 93

5 HYDRODYNAMIC SLIP IN NANOCHANNELS AND ITS WETTABILITY DEPENDENCE 95

5.1 Critical assessment of the hydrodynamic slip length as a surface property 95

5.1.1 Calculation of the friction coefficient λ using different equilibrium theories 98

5.1.2 Calculation of the hydrodynamic slip length using equilibrium theories 102

5.1.3 Comparison between equilibrium and non-equilibrium calculations of hydrodynamic slip 107

5.2 Hydrodynamic slip and its relationship with wettability and the interfacial liquid structure 108

5.2.1 Revisiting the wettability of silicon surfaces and the wettability transparency of graphene-coated silicon 109

5.2.2 Hydrodynamic slip and wettability 113

5.2.3 Hydrodynamic slip and the interfacial liquid structure 117

5.3 Summary 123

6 THERMAL TRANSPORT IN NANOCONFINED WATER AND ITS WETTABILITY DEPENDENCE 126

6.1 Thermal boundary conductance calculations 126

6.2 Thermal boundary conductance between water and silicon under different wettability conditions 131

6.3 Thermal boundary conductance and the interfacial liquid structure 137

6.4 Summary 141

7 CONCLUSIONS 142

7.1 Summary and conclusions 142

7.2 Recommendations for future investigations 147

7.3 Final remarks 149

REFERENCES 151

LIST OF TABLES

Page

Table 3.1: Parameters for some water models. 59

Table 3.2: Summary of the equilibrium models for the calculation of hydrodynamic slip. 63

Table 4.1: Interfacial liquid particles concentration per unit area on silicon and graphene-coated silicon surfaces (nm^{-2}). 92

LIST OF FIGURES

Page

Figure 1.1: The percentage of interfacial atoms decreases as the system size increases and vice versa. 1

Figure 1.2: Geometry and balance of forces on a sessile drop formed on a flat surface. 6

Figure 1.3: Hydrodynamic (a) no-slip and (b) slip boundary conditions. 7

Figure 1.4: Temperature jump observed when heat flows between materials with dissimilar properties. 8

Figure 2.1: Sketch of the principle of operation of the SFA. A sphere of radius r immersed in a liquid experiences a force F_h as the distance h decreases when the sphere approaches at velocity v_a causing drainage of liquid. 25

Figure 3.1: Typical computational box with a representation of its periodic images. The computational box is the box highlighted in green and the circle represents the potential cutoff. 56

Figure 3.2: Schematics of the atomic structure employed in different water models. (a), (b), and (c) are planar models, while (d) is a tetrahedral model. 57

Figure 3.3: Cylindrical droplet wettability modeling stages: (a) initial configuration and (b) snapshot of a droplet in equilibrium. 60

Figure 3.4: Postprocessing steps for obtaining the contact angle from MD simulations: (a) binning of the x-z plane to perform the particles count, (b) density contours obtained time averaging the particles count, (c) determination of the liquid bulk density using the sigmoidal function, and (d) delimitation of the droplet's interface from the density contours. 62

Figure 3.5: (a) fixed and (b) periodic systems commonly use to investigate thermal transport across interfaces. 67

Figure 4.1: Conceptualization of the mean-field theory approach to reduce the complexity of the wettability phenomenon to a single-body problem. 72

Figure 4.2: Sketch of the shifting process performed to obtain the single-particle interaction potential (left panel) and the resulting shape of the potential after adding the individual atomic layer potentials (right panel). 74

Figure 4.3: (a) Comparison between the interfacial liquid density profiles obtained from MD simulations and the different theories. (b) Comparison between MD simulation results of wettability and implementations of different theories. 75

Figure 4.4: Implementation of the formalized multi-response postprocessing method for calculating the contact angle from MD simulations data. analysis of a water droplet made of 4,050 molecules with binning resolution of 2×2 Å (black lines), 1×1 Å (red lines), 0.5×0.5 Å (green lines), and 0.25×0.25 Å (blue lines). (a) Contact angle calculation as a function of time, (b) bulk liquid density as a function of time, (c) root mean squared error (RMSE) of the circular fit used to define the interface, and (d) RMSE of the sigmoidal fit (Equation (3.9)) used to obtain the bulk density of the liquid particles. 77

Figure 4.5: Size effects in the calculation of the contact angle on graphite surface and calibration of the contact angle using the scaling law $\varepsilon_{CO} \sim \theta$ [95]. Symbols: Werder et al. [95] results (circles); same case as in Ref. [95] using the MRPM and cylindrical droplets (squares). 80

Figure 4.6: Comparison between different investigations on the wettability of graphitic-carbon wettability and the theoretical predictions of the BCM. 80

Figure 4.7: Wettability of different silicon planes as a function of the silicon-water interaction strength. 82

Figure 4.8: Si(100) wettability analysis: (a) droplet density contours (g/cm3) where entrainment is observed on the lower plane, $z = 0$, and (b) snapshot of water molecules at the interface with Si(100). 83

Figure 4.9: (a) Unit cell for generating graphene-coated Si(111), (b) underlying structure of a graphene-coated Si(111) surface where h_1 and h_2 characterize the periodic triple bilayer, and (c) underlying structure of a graphene-coated Si(100) surface where h_3 is the inter-plane distance. 84

Figure 4.10: Wettability of graphene-coated silicon surfaces as a function of the silicon-water interaction strength. 85

Figure 4.11: Macroscopic conditions for wettability transparency of (a) graphene-coated Si(111) and (b) graphene-coated Si(100). The shaded regions represent the wettability transparency region with ±5°. All data points have vertical and horizontal error bars 86

Figure 4.12: Density contours of water droplets on Si(100) surfaces (upper panels) and graphene-coated Si(100) surfaces (lower panels). Hydrophobic silicon surface, left panels; hydrophilic silicon surfaces, right panels. The scale is in g/cm^3. 87

Figure 4.13: Density contours of water droplets on Si(111) surfaces (upper panels) and graphene-coated Si(111) surfaces (lower panels). Hydrophobic silicon surfaces, left panels; hydrophilic silicon surfaces, right panels. The scale is in g/cm^3. 88

Figure 4.14: Droplets center-line density profiles along the z-direction of Si(100), Si(111), and graphene-coated silicon surfaces under (a) hydrophobic, (b) hydrophilic, and (c) transparent conditions. 90

Figure 4.15: Corrugation of the solid-liquid interaction potential for (a) Si(100), (b) Si(111), and (c) graphene-coated silicon surfaces (only showing the carbon atoms). The units are kJ/mol and only the attractive potential is depicted. 92

Figure 5.1: Nanoconfined water between graphite plates used to investigate the accuracy of the equilibrium theories of hydrodynamic slip. 96

Figure 5.2: (a) density and (b) pressure profiles in water at different levels of confinement.97

Figure 5.3: Calculation of the friction coefficient λ using Bocquet and Barrat's theory [131, 167] with (a) unbiased algorithms and (b) biased algorithms for the evaluation of the time correlation functions. 99

Figure 5.4: Calculation of the friction coefficient λ using the theory by Huang and Szlufarska [168]. 100

Figure 5.5: Implementation of Hansen et al. [166] method for calculating the liquid slab normalized (a) time correlation function and (b) the Laplace-transformed correlation functions. 101

Figure 5.6: Calculation of the hydrodynamic slip length using the Bocquet and Barrat's theory and the reinterpretation of this theory by Petravic and Harrowell. 103

Figure 5.7: Calculation of the hydrodynamic slip length using the Huang and Szlufarska's [168] theory. 104

Figure 5.8: Statistical analysis of the displacement of the liquid molecules confined in nanochannels: H = 3 nm, upper panels (a) and (b); H = 5 nm, middle panels (c) and (d); and H = 8 nm, (e) and (f). The right panels are histograms of the time-average position of the liquid particles and the left panels are plots of the average versus standard deviation position of the liquid particles in the confinement. 106

Figure 5.9: Comparison between non-equilibrium (solid symbols) and equilibrium (shaded regions) calculations of L_s. 108

Figure 5.10: Water confined within (a) Si(111), (b) Si(100), and (c) graphene-coated silicon nanochannels. 109

Figure 5.11: Wettability of different silicon planes expressed and the scaling laws correlating (a) $\varepsilon \sim 1+\cos(\theta)$ and (b) $\varepsilon \sim 180°-\theta$. 111

Figure 5.12: Wettability of pristine and graphene-coated silicon surfaces. The MD simulations results (symbols) verify the theoretical predictions (solid lines) of the wettability of graphene-coated silicon. Two different values for the equilibrium distance between graphene and silicon (δ_{GS}) were used for validation. The shaded region represents the wettability transparency condition with a ±2.5° deviation from $\theta_S = \theta_{GS}$. 112

Figure 5.13: Density profiles along the nanochannels height with contact angles of (a) θ = 71° and (b) θ =150°. 113

Figure 5.14: Relationship between hydrodynamic slip and wettability for silicon nanochannels having different wettability and graphene-coated silicon nanochannels under wettability transparency conditions. 114

Figure 5.15: Velocity profiles obtained for (a) Si(100) nanochannels and (b) Si(111) nanochannels. 116

Figure 5.16: Velocity profiles obtained for (a) graphene-coated Si(100) nanochannels and (b) graphene-coated Si(111) nanochannels under wettability transparency conditions. 117

Figure 5.17: Reconciliation of the hydrodynamic slip length calculations in silicon nanochannels having different contact angles and graphene-coated silicon nanochannels. 118

Figure 5.18: (a) Interfacial liquid water density profiles and (b) depletion length calculations. 119

Figure 5.19: Interfacial density contours (g/cm^3) under hydrophilic conditions for (a) Si(111) and (b) Si(100) nanochannels. 122

Figure 5.20: Interfacial density contours (g/cm^3) under wettability transparency conditions for (a) Si(111) and (b) Si(100) graphene-coated nanochannels. 123

Figure 6.1: (a) silicon and (b) graphene-coated silicon systems used to investigate the thermal transport across bare surfaces with different wettability and under wettability transparency conditions. 127

Figure 6.2: Temperature profiles obtained for hydrophilic silicon Si(111) and water with a heat flow of 20 nw. 128

Figure 6.3: Thermal boundary conductance calculations for Si(100) and Si(111) under (a) hydrophilic and (b) hydrophobic wettability conditions. 129

Figure 6.4: Analysis of the size effects on the calculation of the thermal boundary conductance. 130

Figure 6.5: Ratio of the hot to cold thermal boundary conductance calculations for different wettability conditions. 131

Figure 6.6: Thermal boundary conductance relationships for different silicon and graphene-coated silicon surfaces. (a) Thermal boundary conductance vs. the work of adhesion (1+cosθ) and (b) thermal boundary conductance vs. the contact angle. 133

Figure 6.7: Thermal boundary conductance dependence on the silicon-water interaction strength. 134

Figure 6.8: Reconciliation of the contact angle calculations using the solid-liquid interaction energy per unit area and (b) thermal boundary conductance vs. the solid-liquid interaction energy per unit area. 134

Figure 6.9: Phonon density of states (DOS) in arbitrary units of atomic layers in the bulk and interface of Si(100) and Si(111) in contact with water. 136

Figure 6.10: Decomposition in out-of-plane and in-plane phonon modes of interfacial (a) Si(111) and (b) Si(100) atoms. 136

Figure 6.11: Reconciliation of the thermal boundary conductance calculated for different surfaces in contact with water using the density depletion length. 138

Figure 6.12: Figure 6.12: (a) Density layering and snapshots of the interfaces of (b) Si(100), (c) Si(111), and Si(100) coated with graphene under the same wettability conditions, $\theta = 71°$. 140

LIST OF SYMBOLS AND ABBREVIATIONS

A	Area
ΔT_{int}	Interface temperature jump
F_i	Force component or attribute i
G	Thermal boundary conductance
H	Nanochannel height
J	Heat flux
k_{B}	Boltzmann constant
k_{e}	Coulomb constant
L_{K}	Kapitza length
L_{s}	Slip length
m	Mass
q	Charge
r	Distance between particles
r_{B}	Droplet base radius
R_{K}	Kapitza resistance
T	Absolute temperature
u_{s}	Slip velocity
x,y,z	Cartesian coordinates
V	Non-bonded interaction potential
w	Single particle interaction potential
W_{ad}	Work of adhesion
$\langle B(t), B(0) \rangle$	Time autocorrelation operation on B

Abbreviations

BCM	Boltzmann calibrated model
LJ	Lennard-Jones (potential)
MRPM	Multiresponse postprocessing method
RMSE	Root-mean squared error
SAM	Self-assembled atomic monolayers
TBC	Thermal boundary conductance
TDTR	Time-domain thermorefectance

Greek symbols

θ	Contact angle
δ	Density depletion length
ε	Energy parameter of the LJ potential
σ	Length parameter of the LJ potential
η	Shear viscosity
λ	Solid-liquid interface friction coefficient
γ	Surface tension, surface free energy
$\dot{\gamma}$	Shear rate
κ	Thermal conductivity
τ_L	Line tension
ρ	Density

SUMMARY

Experimental and numerical investigations indicate that surface effects govern the transport phenomena in nanoconfined liquids. The wettability of solid surfaces, usually characterized by the static contact angle, has been used to correlate the hydrodynamic boundary condition and the thermal transport at solid-liquid interfaces. Recent investigations suggest the existence of quasiuniversal laws correlating the hydrodynamic slip length and the contact angle in nanoconfined liquid flows. Likewise, a correlation between the work of adhesion and the thermal boundary conductance has been consistently reported in previous investigations. Classical molecular dynamics simulations and a physically sound theoretical background were used to critically assess the effects of wettability on the interfacial momentum and thermal energy transport at solid-liquid interfaces. In particular, the silicon-water interface was investigated due to the rising importance of silicon-based sensors and devices operating in aqueous environments. The wettability of the Si(100) and Si(111) planes was theoretically and numerically characterized. Additionally, the recently discovered wettability transparency phenomenon was considered in this investigation in order to provide a broader perspective of the wettability effects on interfacial transport phenomena. The results indicated that although the wettability of a given surface can be of practical use to describe the hydrodynamic boundary condition and thermal transport in nanoconfined liquids, the interfacial liquid structure properties give a universal description of these phenomena which is being reported here for the first time. These groundbreaking results provide the foundations to theoretically tackle the challenging task of describing

interfacial transport in nanoconfined liquids; likewise, these results suggest the possibility of developing highly efficient nanofluidics devices with applications in the biomedical sciences, the energy sector, ultrafast flow delivery systems, low friction nano- and microgap bearings, etc., by means of tailoring the properties of the interfaces in order to achieve low friction flows or highly conductive solid-liquid interfaces.

CHAPTER 1

INTRODUCTION

1.1 Background and motivation

Nanofabrication has brought forth new opportunities for scientist and engineers to revise our current understanding of the effects of scale on the laws of physics, and during the process, we have been able to envision and develop new technologies. Since the first theoretical conceptions of micro- and nanoscale devices, it was evident that a number of new and exciting problems would arise due to the length scale effect on some the laws of nature. For example, the reliability of the continuum medium hypothesis is significantly reduced once the length scale investigated is comparable to the molecular dimensions. As a consequence of the scaling laws, surface effects become more significant as the size of a given system decreases (the surface-to-volume ratio scales as L^{-1}), while the inertia effects become negligible (inertia scales as L^{3}). Figure 1.1 illustrates how the percentage of atoms constituting the interface increases as the system size decreases. Therefore, a thorough understanding of the interfacial phenomena at small length scales is required to efficiently design, develop, and fabricate nanoscale devices. Moreover, this is not only important to small scale devices, but in general to all interfacial phenomena as the exchange of momentum, mass, and energy takes place within the short-range of the atomic interactions.

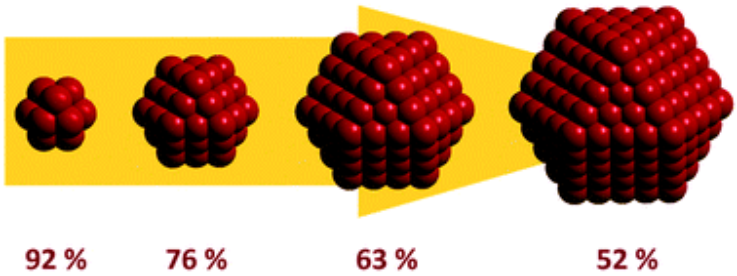

Figure 1.1: The percentage of interfacial atoms decreases as the system size increases and vice versa.

The combination of liquid flow in nanochannels and microelectronics control has led to the creation of highly sensible measuring devices, such as lap-on-a-chip, for the individual examination of minuscule particles contained in a flow stream. The biomedical community has taken advantage of these technologies in applications such as the analysis of biological solutions for DNA sampling [1-4], high precision drug delivery [5-8], and low-cost cell analysis for disease diagnostics [9, 10]. In addition to biomedical applications, one can find applications of nanoconfined flows for use in the improvement of electrochemical-mechanical energy conversion in batteries [11], electrical energy generation from salinity gradients [12], barrier films with selective filtration and separation [13], and nanofluidics diodes and transistors [14-19]. Similarly, the dynamics of thin confined fluids are important in many industrial processes: as the tolerances of machine parts are reduced and operating speeds increase, an appropriate lubrication of these small gaps is required [20]. Ultrafast water transport has been experimentally reported in membranes made of carbon nanotubes [21], indicating that flow rates are four to five times those predicted by classical fluid dynamics. While these observations seem to be opposite to conventional predictions (hydrodynamic resistance scales as L^{-4}), these results have been explained in terms of the frictionless environment caused by the repulsive interaction between carbon surfaces and water, which are enhanced as a result of the scaling effect. Numerical investigations support these findings in a qualitative manner [22]; however, the breach between numerical and experimental results is substantial. Nevertheless, the enhanced surface effects on the hydrodynamic behavior of nanoconfined liquids suggest a clear opportunity to develop fast flow delivery systems by taking advantage of the surface chemistry of some surfaces.

The validity of the Navier-Stokes equations (momentum conservation equations of Newtonian fluids), or the lower scale limit for which the definition of the shear viscosity holds, can be derived from a scale analysis performed on the fluctuation-dissipation definition of viscosity in equilibrium. For water, this limit has been found to

be ~1 nm [23]; in contrast, the appropriateness of the no-slip boundary condition is an assumption that is not based on any physical principles [24]. Experimental [25-35] and numerical [22, 36-41] evidence suggest that the no-slip boundary condition does not hold for nanoscale flows, and that the actual boundary condition is a multivariable function. In general, the boundary condition can be one of slip or locking and it depends on a number factors such as the wettability of the surfaces (surface chemistry) [37, 42-49], the interfacial liquid structure [44, 50, 51], the surface roughness [27], and the operating shear rate [39, 46-48, 52-60]. The impact of wettability on the hydrodynamic slip, which is characterized by the slip length, is so significant that a quasiuniversal relationship based on experimental and numerical findings has been proposed between the contact angle and the slip length [45].

Friction is the most important interfacial property limiting the fluid transport at the nanoscale [61]. The high hydraulic resistance caused by inducing flow in nanoscale confinements is the major drawback in these types of applications if the surface chemistry is not appropriate to induce low friction flow as in carbon nanotubes [21, 22]. Pressure drops as large as 4 MPa have been reported in nanochannels arrays at flow rates as low as 0.1 μl/h [53]. Additionally, the high shear rates observed in lubricated microgaps lead to viscous heating of the fluid, ultimately requiring a removal of thermal energy through the solid-liquid interface for proper operation [20]. Experiments indicate that there is a direct relationship between the wettability of surfaces and the thermal boundary conductance (TBC) at the solid-liquid interface [62, 63]. These trends have been confirmed by numerical investigations [64-66], although controversy exists on the actual dependence of the TBC on the surface chemistry. Recent nanoultrasonics probing experiments have demonstrated that the first few water molecular layers govern interface-mediated properties and energy transfer [67]. By using high frequency acoustic waves, a nanoscale resolution of hydrophilic solid-liquid interfaces was obtained. It was shown that the bulk water properties get significantly affected at the interfacial region by the

strong solid-liquid interactions. No molecular layering was reported as in numerical simulations, since nanoultrasonics depends on having a medium available for energy transfer, and the density depletion at the interface observed in numerical simulations is then difficult to observe with this method [67].

Hydrodynamic slip and interfacial thermal transport at the solid-liquid interface depend on the wettability of the solid surfaces as well as on the operating shear rate in highly confined liquids. These processes are coupled when the shear rates are high enough to produce viscous heating in the nanochannel. Attempts have been made to explain this phenomenon [68-72], but controversy still exists about the relationship between the hydrodynamic slip length and the TBC at the solid-liquid interface. Even at the most fundamental level, there has been a lack of consensus on how to properly perform atomistic simulations of nanoconfined liquids [54, 73, 74].

Recently, an intriguing phenomenon has been discovered, the wetting transparency of graphene-coated surfaces [75-78]. As has been reported, the contact angle of a solid substrate remains unaltered if the solid is coated with a single-layer of graphene, but only if certain conditions (substrate wettability) are given. A lack of consensus still exists in the literature about the actual existence of wettability transparency and about the conditions required to obtain it. On the practical side of this finding, for example, a graphene coating could serve as a protecting barrier to the oxidation of many surfaces, in particular for silicon and copper. This is important as graphene-silicon hybrid structures are promising candidates for future transistors due to the adjustable Schottky barrier between the two materials [79]. The newly discovered wetting transparency of graphene-coated surfaces also presents an opportunity for deepen into the nature of the correlation between wettability and interfacial phenomena, such as hydrodynamic slip and solid-liquid thermal transport. If the contact angle remains unaltered between a bare substrate and a graphene-coated version of it, this means that the work of adhesion or the total solid-liquid interaction energy is the same; thus, it is

possible to separate the total energetic contribution from the surface structure effect, as these two are coupled. In other words, the wettability of a surface is not only determined by the solid-liquid affinity, but by a combination of it with the surface granularity, which eventually modifies the energy landscape formed due to the solid-liquid interactions. Therefore, the changes in the interfacial properties provide a mechanism by which the effects of wettability and interfacial liquid structure can be assessed on hydrodynamic slip and thermal transport in a separate manner. Additionally, the application of the wettability transparency of graphene-coated surfaces poses an opportunity to numerically investigate systems with similar contact angles as reported from theory, simulations, and experiments [75-78], instead of artificially induce different wettability conditions in a numerical model and expect that a real system may behave as predicted.

The hydrodynamic boundary conditions are unquestionably determined by the efficiency of the momentum transport between the solid and liquid atoms at the interface. The total energy interactions as well as the granularity of the solid surface determine the efficiency of this transport. Therefore, investigating hydrodynamic slip in liquids confined by graphene-coated surfaces under wettability transparency conditions allows separating both effects and testing the current theories correlating wettability and hydrodynamic slip. Alternatively, the interfacial thermal transport is dictated by the phonon density of states of the interfacial atoms, a property evidently affected by the addition of a coating layer. However, experimental and theoretical investigations suggest that there is a relationship between the wettability and solid-liquid thermal transport, in addition that the phonon density of states is affected by the wetting condition at the interface [80, 81]. Thus, by investigating thermal transport between liquids and graphene-coated surfaces under wettability transparency conditions allows to critically analyze the relationship between surface chemistry and interfacial heat transfer.

1.2 Review of concepts

Wettability is the property of a liquid to maintain contact with a surface or it is also understood as the affinity between liquids and solids [82]. Conventionally, the wettability of a surface by a given liquid is determined by measuring the contact angle (θ) from the geometry of a sessile drop formed as illustrated in Figure 1.2.

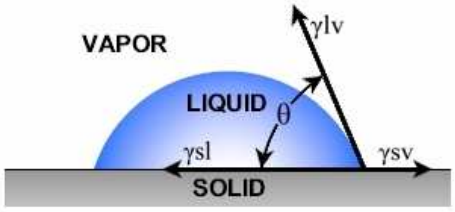

Figure 1.2: Geometry and balance of forces on a sessile drop formed on a flat surface.

In the absence of any external body forces and assuming a perfect contact with the surface, the following expression is obtained from the balance of forces at the triple-phase contact line:

$$\gamma_{LV}\cos(\theta)=\gamma_{SV}-\gamma_{SL}\,, \tag{1.1}$$

where γ is the surface tension and LV, SV, and SL stand for liquid-vapor, solid-vapor, and solid-liquid. Since γ is an equilibrium property, θ is also considered an equilibrium property. Depending on the magnitude of the contact angle, a surface is usually defined as hydrophilic $\theta < 90°$ or hydrophobic $\theta > 90°$. Alternatively, Equation (1.1) can be obtained from a minimum energy principle analysis of the interfaces of the system depicted in Figure 1.2. Given that the system under consideration has a fixed number of particles, fixed volume, and temperature (NVT), the most appropriate thermodynamic potential to describe it is the Helmholtz function [82]. After minimizing the energy function as a function of area, Equation (1.1) is deducted from a more formal analysis.

The work of adhesion, see Equation (1.2), is defined as the reversible work per unit area required to turn apart a solid-liquid interface. It can also be viewed as the net

reversible work required to destroy a solid-liquid interface ($-\gamma_{SL}$) and create two new interfaces ($\gamma_{SV} + \gamma_{LV}$), namely,

$$W_{ad} = \gamma_{LV} + \gamma_{SV} - \gamma_{SL} = \gamma_{LV}\left(1+\cos\theta\right). \tag{1.2}$$

The work of adhesion is used as a measurement of the magnitude of the solid-liquid affinity.

Since the early work by Navier [83], the possibility of a slip boundary condition was suggested as

$$u_s = L_s \left.\frac{\partial u}{\partial z}\right|_{z_0} \tag{1.3}$$

where u_s is the slip velocity at the interface z_0, L_s is the slip length, $\left.\partial u / \partial z\right|_{z_0}$ is the velocity gradient evaluated at the interface, and z is the coordinate in the normal direction to the interface. The slip length (L_s) is obtained as the extrapolated distance, from the interface, required for the velocity profile to reach the no-slip boundary condition, see Figure 1.3.

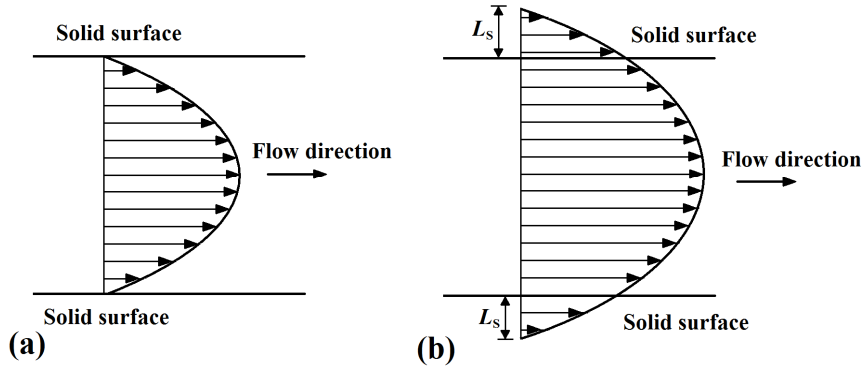

Figure 1.3: Hydrodynamic (a) no-slip and (b) slip boundary conditions.

By applying the viscous law of friction at the interface (shear force is proportional to velocity), it is possible to obtain the shear force per unit area acting on the walls as

$$F_{shear} = -\eta \left.\frac{\partial u}{\partial z}\right|_{z_0} = -\lambda u_s, \tag{1.4}$$

where λ is the solid-liquid friction coefficient, η is the shear viscosity of the liquid, and L_s can be obtained by

$$L_s = \frac{\eta}{\lambda}. \tag{1.5}$$

In the following chapters, methods for calculating λ will be discussed and implemented. L_s is commonly used in the literature to characterize the hydrodynamic boundary condition as indicated in Equation (1.3); however, higher order descriptions have been proposed [84]. In addition to represent the boundary condition, L_s can also be considered as an indication of the magnitude of the solid-liquid friction. Large values of L_s indicate low friction (small λ) and small values correspond to large friction (large λ).

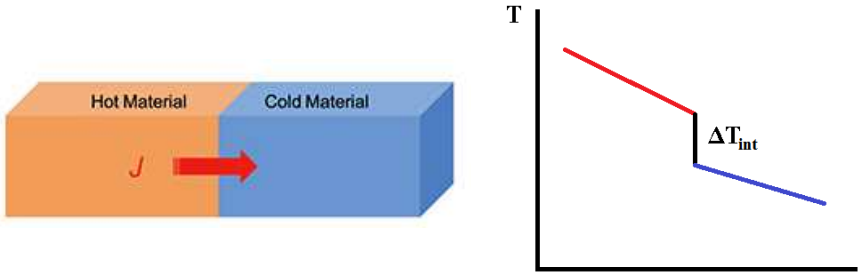

Figure 1.4: Temperature jump observed when heat flows between materials with dissimilar properties.

When heat travels between dissimilar materials, a temperature jump is observed at the interface due to: 1) the microscopic imperfections at the contact region (the effective contact are is not the same as the cross-section area) and 2) the thermal vibration properties mismatch between materials (the thermal vibrations or phonons move at different speeds when traveling from one material to another), see Figure 1.4. For a given heat flux (J), such a temperature jump (ΔT_{int}) can be related to a thermal resistance as

$$\Delta T_{int} = JR_B, \tag{1.6}$$

where R_B is the thermal boundary resistance, and its inverse $G = 1/R_B$ is the thermal boundary conductance (TBC), such that $J = G\Delta T_{int}$. Such a temperature jump was first reported by Pyotr Kapitza in 1941 while experimenting with the superfluidity of helium

at very low temperatures [85]. Although Kapitza was not the first one to observe this phenomenon he was the first one to report it [86]. Oftentimes, the Kapitza length is also used for characterizing the thermal resistance of an interface as

$$L_K = R_K \kappa \tag{1.7}$$

where R_K is the Kapitza resistance and L_K is the Kapitza length or the equivalent length of a material, with effective thermal conductivity κ, required to generate a thermal resistance R_K. Although similar in definition, R_K and R_B, differ in that R_K only applies to perfectly smooth surfaces in perfect contact. Physicists quickly followed the steps of Kapitza and tried to explain the interfacial temperature jump by means of analytical models. The acoustic mismatch model (AMM) was one of the first theories trying to predict the thermal boundary resistance between liquid helium and solids at very low temperatures. This model is based on continuum acoustics and treats phonons as plane waves that can be either transmitted or reflected when they reach an interface [87]. Another theoretical model, the diffusive mismatch model (DMM) assumes that all phonons striking an interface lose memory of where they come from and the probability of being scattered to one side of the interface or the other is just a function of the phonon density of states [86]. A noticeable limitation of these theories is that none of them takes into account the solid-liquid affinity, an interfacial property, and they only deal with bulk properties; thus, these theories are not able to accurately predict thermal transport through solid-liquid interfaces at room temperature even though the contact is perfect between phases.

1.3 Research objectives and summary of findings

The growing importance of understanding the solid-liquid interactions at the nanoscale and the noticeable gaps that exist in the literature about the hydrodynamic slip condition and thermal transport calls of for deeper investigations. A thorough literature review was conducted and the main discrepancies found among the community were identified. Reports on experimental and numerical investigations were consulted and it

was found that nowadays, many are the challenges faced to properly determine the nature of the hydrodynamic boundary condition in highly confined liquids. Solid-liquid thermal transport experiments have shown more consistent trends about the dependence of the thermal boundary conductance on wettability; unfortunately, the type of materials required for experimentation limits the variety of interfaces that can be investigated. On the numerical approaches used to undertake these investigations (classical atomistic modeling), inconsistencies among publications were found. Thus, a number of publications have been exclusively dedicated to highlight the sources of error and unphysical conditions used in atomistic modeling, for example to simulate highly confined liquids.

The main objective of this dissertation was to further develop the understating of the solid-liquid interactions in order to determine how the nanoscale phenomena affect the macroscopic-observable properties, such as the contact angle, hydrodynamic slip, and thermal transport. Unlike previous investigations, a major portion of the efforts were focused on gaining a deep understanding of how the surface chemistry and granularity affect the wettability of pristine solid surfaces. A theoretical model of wettability was formulated to explain the wettability of different solid surfaces obtained from atomistic simulations; in particular, graphitic carbon and different silicon planes in contact with water were amply studied in this work. This theoretical model was able to fully predict, once calibrated, the wettability of graphene-coated silicon surfaces. A formalized method for obtaining the contact angle from molecular dynamics (MD) simulations was developed. This method features the capabilities of tracking the calculations as a function of the data sets analyzed over time and also a remarkable accuracy in the calculation of the contact angle. By combing MD simulations and a strong theoretical background, the experimentally determined wettability of graphite and silicon was incorporated into an atomistic model. Once the solid-liquid interaction potentials were validated from MD

simulations and theory, the macroscopic and microscopic conditions necessary to observe the wettability transparency of graphene-coated silicon were fully described.

The calibration of the graphite/silicon-water interaction potentials with experimental results of wettability allowed investigating the hydrodynamics of nanoconfined water. First, the most reliable methodology for properly representing the physics of nanoconfined liquids was implemented in equilibrium and non-equilibrium models. Secondly, a critical assessment of the current theories to calculate the hydrodynamic slip from systems in equilibrium was conducted. These findings were compared with non-equilibrium calculations of liquid flow in silicon nanochannels. Lastly, the relationship between wettability and hydrodynamic slip was investigated and the newly discovered wettability transparency of graphene-coated silicon surfaces was investigated for the first time in nanoconfined liquid flow. The results indicated that the wettability of a surface, characterized by the contact angle, might not be as reliable as previously thought, but instead the density depletion (interfacial liquid structure) poses a better alternative to characterize the hydrodynamic boundary condition. Additionally, the calibration of the silicon-water interaction with experiments of wettability was used to verify the existence of a no-slip boundary condition, as reported from experiments, in silicon nanochannels as small as 100 nm.

Non-equilibrium MD simulations were used to investigate thermal transport across silicon-water interfaces. Different crystal planes in contact with water were investigated in order to evaluate the effects of the macroscopic contact angle, atomic/energy granularity, and interfacial water structure on the thermal boundary conductance. As in the hydrodynamic slip portion of this investigation, it was found that the contact angle is not a universal parameter to describe the solid-liquid thermal transport. Alternatively, the interfacial liquids properties, such as density depletion and concentration per unit area, were found to be more adequate to characterize the thermal

response of solid-liquid interfaces, since the number of energy carriers is the major discriminant of the effectiveness of the thermal transport.

Overall, the deficiencies of characterizing the interfacial phenomena by means of the contact angle obtained from MD simulations of wettability are discussed in this dissertation. The wettability model developed here helped in understanding the multitude of variables that affect the outcome of an atomistic simulation of wettability. It is suggested to approach with caution the calibration of the solid-liquid interactions with wettability experiments, since there are many variables not being considered during the process. Eventually, when energy and momentum investigations are conducted with calibrated potentials, the outcome of the simulations might not match the realistic response of the systems.

1.4 Dissertation outline

This dissertation is divided into seven Chapters. Chapter 1 has been already covered and it contains the motivation of the problem under investigation, the research objectives, and a brief review of the three main phenomena investigated herein.

Chapter 2 contains the review of the consulted literature. The noticeable gaps existing in the investigation of hydrodynamic slip and thermal transport across soli-liquid interfaces are highlighted. The current methods for performing wettability, hydrodynamic slip, and thermal transport calculations using atomistic modeling are presented and criticized.

Chapter 3 deals with the methodologies employed during this investigation. Molecular dynamics simulations are presented as an efficient manner to investigate the solid-liquid interactions and interfacial phenomena. The parameters and characteristics of the simulations are thoroughly described. A formalized method for performing wettability simulations is introduced. The equilibrium and non-equilibrium methods for calculating hydrodynamic slip and thermal transport are presented.

Chapters 4, 5, and 6 contain the wettability, hydrodynamics, and thermal transport results of this investigation, respectively.

Chapter 7 contains a summary, conclusions, and recommendations for future investigations.

CHAPTER 2

LITERATURE SURVEY

A thorough review of literature is summarized in this Chapter in a brief but concise manner. Molecular dynamics simulations are presented as a reliable alternative for conducting the analysis of interfacial phenomena from a fundamental point of view. The current challenges faced for experimentally determining the hydrodynamic boundary condition and thermal transport at the nanoscale are reviewed. A review of the main theories that look to explain the behavior of the interfacial phenomena with wettability is presented herein. This literature review helped to put the current investigation into context and allowed to highlight the contribution of it.

2.1 Wettability modeling as a method for calibrating the solid-liquid interactions

In classical molecular dynamics (MD) modeling, it is a common practice to calibrate or optimize the atomic interaction potentials in order to obtain a bulk property of a given material. Once the potential has been calibrated for one or a set of properties, further numerical investigations can be performed with some degree of validation. However, when non-identical materials interact, a new parameterization is required [88]. Often times, the non-bonded interaction potentials between non-identical pairs of atoms are obtained through the Lorentz-Berthelot mixing rules, even though the inadequacy of using such combination rules has been demonstrated for systems as simple as gas mixtures [89]. Likewise, the application of such mixing rules leads to miscalculating the equilibrium separation between materials, for example graphene on silicon. The application of the mixing rules predicts an equilibrium separation of 3.5 Å, while experiments [90] and quantum simulations [91, 92] indicate that 2 Å is more realistic. Hence, the calibration of the interaction potentials between solid and liquid atoms has

been conducted, for some years now, such that the wettability observed in experiments can be retrieved from numerical simulations.

MD simulations offer a unique opportunity to perform computer experiments to evaluate the wettability of various surfaces, given that the contact angle can be obtained from the fundamental solid-liquid atomic interactions, modeled by Lennard-Jones (LJ) potentials, and statistical analyses. A number of methods have been developed to extract the macroscopic contact angle, θ_∞, from MD simulations. These include: 1) a method in which the surface tensions are obtained from statistical calculations of the stresses [93] and algorithms such as the phantom wall [94], followed by the application of the Young's equation (Equation (1.1)) to determine θ_∞; 2) the microscopic contact angle (θ) and droplet base radius (r_B) are obtained from hemispherical droplets of different sizes, allowing θ_∞ to be obtained through data fitting using the modified Young's equation,

$$\cos\theta = \cos\theta_\infty - \frac{\tau_L}{\gamma_{LV} r_B} \tag{2.1}$$

where τ_L is the line tension that represents a size-effect, in the thermodynamic limit $r_B \rightarrow \infty$ and the Young's equation is obtained; and 3) cylindrical liquid slabs are equilibrated over atomically flat surfaces and assuming that the contact line is straight ($r_B \rightarrow \infty$), the microscopic contact angle is considered to be similar to its macroscopic counterpart as predicted by Equation (2.1).

Graphitic-carbon wettability was investigated by means of MD simulations of hemispherical droplets by Werder et al. [95], Jaffe et al. [96], and Walther et al. [97]. These authors parametrically investigated the effects of the interaction potential parameters between carbon atoms and water molecules and found a linear relationship between θ_∞ and the water-graphite binding energy (E_b). They proposed optimal interaction potential parameters and potential cut-off radii to obtain θ_∞ of graphite from MD simulations, outlined postprocessing methods, and addressed the size effects by means of the spherical droplet method.

The cylindrical droplet method offers a computationally affordable alternative to the spherical droplet method due to the theoretically non-size-affected contact angle calculations obtained from it. Scocchi et al. [98] performed a comparative analysis of graphite wettability using hemispherical and cylindrical droplets and found a marked size effect; however, a convergence of both methods was found in the thermodynamic limit. Vanzo et al. [99] investigated the contact angle of graphane (functionalized graphene) using MD simulations of cylindrical droplets, where a discussion on why the cylindrical droplet is more efficient than the hemispherical droplet was presented. Hemispherical droplets showed contact radius size dependence for small droplets and deviations from the modified Young's equation, Equation (2.1). Alternatively, the cylindrical droplet technique was less computationally expensive with a negligible line tension effect. Additional references [75, 100-102] also highlight the efficiency of the cylindrical over the spherical droplet wettability simulations.

A substantial number of investigations have dealt with the characterization of the wettability of graphitic surfaces, while some others with the fundamental modeling of wettability using simple systems (LJ particles). The wettability of silicon, an important material used in microfabrication, has not been extensively investigated mainly because of the difficulty found in keeping a silicon surface exposed to air absent of a SiO_2 forming on top of it. Barisik and Beskok [103] widely acknowledged this issue and reported a good review of experimental investigations on the wettability of silicon. These authors were the first in characterizing the contact angle of the (100) plane of silicon, or simply Si(100), by means of MD simulations of hemispherical droplets wettability. The characterization was performed by varying the strength of the silicon-water interactions and recording the size-independent contact angle obtained for each condition.

2.1.1 Line tension effects in MD simulations of wettability

The contact angle of a liquid on a solid is well described in the thermodynamic limit by the Young's equation. For droplet sizes in the order of nanometers, the density fluctuations of the three-phase contact line adds to the free energy of the system. Such a contribution is size dependent and usually accounted for by adding the line tension term to the original Young's equation to obtain the modified Young's equation.

Schimmele and Dietrich [104] published a short communication where the definition of the line tension and the deficits of using the modified Young's equation are discussed. Experimental data and theoretical models about the line tension are criticized in depth. It is indicated that the conventional definition of the Young's equation is incomplete due to its dependence on the different possible definitions of the position of the various dividing interfaces between the three phases. In order to have a proper definition of the line tension, one has to take into account surface and volume contributions to the stiffness of the contact line. For instance, different definitions of the line tension can arise due to the pressure dependence of the solid-vapor interfacial tension (pressure variation due to curvature of the interface). Schimmele and Dietrich [104] concluded that the modified Young's equation has a limited range of applicability and further investigation is required on the subject.

Weijs et al. [101] conducted a comprehensive investigation on the effects of line tension in the wettability of nanoscale droplets made of LJ particles. Classical MD simulations of cylindrical and hemispherical droplets as well as a quantum model were used to predict the contact angle of nanodroplets as well as the line tension. The results demonstrated the convergence of the microscopic contact angle to a macroscopic value by three different methods: 1) extrapolation of the hemispherical contact angle data to de macroscopic limit using the modified Young's equation, 2) obtaining a fairly constant value of the contact angle of a cylindrical droplet for three different drop sizes, and 3) from independent calculations of the three surface tensions and using Young's equation.

In the limit of large systems, both, the hemispherical and the cylindrical methods converged to a constant value, also matched by the direct calculation using Young's equation. The cylindrical droplets did not show any effect of line tension, but other curvature effects such as the Tolman correction and the effect of the Laplace pressure on the solid-liquid surface tension. The quantum calculations matched those obtained by MD simulations about the dependence of the contact angle on the droplet size. Therefore, MD and quantum simulations predicted a negative line tension for the hemispherical droplet and zero line tension for the cylindrical one. Quantum simulations indicated that the line tension term is a leading order term of an expansion of $1/r_B$ and is valid only for relatively large drops. However, quantum and classical approaches differed dramatically when comparing the line tension prediction as a function of the Young's contact angle. The quantum model captured the vanishing of the line tension at the extremes of 0° and 180°, whereas the classical one diverged at small contact angles.

Peng et al. [102] used Monte Carlo simulations to obtain the line tension and contact angle of spherical and cylindrical nanodroplets made of LJ particles. The three surface tensions were independently calculated to obtain the macroscopic contact angle predicted by Young's equation and found out that cylindrical nanodroplets gave a very accurate prediction of the macroscopic contact angle, except when the surface is highly hydrophobic, this was attributed to the constant chaotic motion of the droplet not allowing for the capture of the precise contact angle. Peng et al. [102] also verified the independence of the contact angle with respect to the cylindrical size droplet at different wettability conditions. Spherical droplets showed a significant variation of the contact angle with respect to the macroscopic value, except for the case of hydrophilic surfaces. It was concluded that the line tension is so small and varies so widely that a reliable measure of such is not possible.

2.1.2 Calibration with experiments vs quantum calculations of the solid-liquid interaction potentials

Wu and Aluru [105] used *ab initio* (quantum mechanics) calculations to obtain the non-bonded interaction potential between graphitic carbon and water. A series of models were used to obtain, from first principle calculations, a pairwise interaction potential to be applied in MD simulations. It was found that by using Werder et al. [95] and Schochi et al. [98] pairwise interaction parameters fitted through MD predictions of experimental contact angles, and interaction parameters obtained through mixing rules, miscalculations of the binding energy between a water monomer and carbon are obtained. The interaction energy dependence on the water molecule orientation with respect to the graphite surface was taken into account by adding nonzero hydrogen-carbon interactions into the pairwise potential. MD simulations of spherical droplets were conducted in order to find the contact angle with the new *ab-initio*-developed potentials and the widely used potential developed by Werder et al. [95]. Wu and Aluru [105] found that a significantly lower contact angle is predicted using the quantum-derived potentials in comparison with the calibrated ones. A comparison between the experimental contact angles of graphite with simulations was conducted by introducing two categories: 1) experiments conducted at ambient conditions, and 2) experiments conducted in ultrahigh vacuum. The utilization of two of the quantum-based potentials matched the range of contact angles in ultraclean graphite surfaces. These two models predicted almost the same binding energy, but a difference of 8° was found in the contact angle predictions. It was hypothesized that binding energy alone is not enough to describe the carbon-water interactions, as previously formulated by Werder et al. [95].

Driskill et al. [106] reported a good agreement between the values of the binding energy and the zero potential distances for graphene and water obtained via *ab initio* simulations and using MD empirical models; however, a wide range of *ab initio*-derived

binding energies were found during the literature review reported in [106]. In other words, it was found that *ab initio* potentials produced a wide range of binding energies between water and carbon and require further adjustments to be used as pairwise additive force fields in MD simulations. Therefore, the empirical parameterization of the solid-liquid interaction potentials was suggested as an alternative to *ab-initio*-derived potentials.

The limitations of the interaction potentials derived from quantum calculations are the dependence of the interaction strength with respect to the liquid molecules orientation, the significantly limited number of particles that can be incorporated in a quantum model, and the lack of a direct application of these potentials in a pairwise fashion as required in MD simulations. Alternatively, the calibration of the solid-liquid interaction potentials in classical MD simulations is performed in systems encompassing a large number of particles, the calculations are performed in systems in equilibrium, and the process is performed looking to match an experimentally reported parameter.

2.1.3 Theoretical models of wettability

On the theoretical side, wettability models are typically based on the reduction of a many-body problem to a single-body problem, i.e., the mean-field (MF) approach. The single-particle treatment of the wettability problem depends on an appropriate description of the density distribution of the particles at the interface and on a single-particle potential. In most MF models of wettability, the work of adhesion only considers the solid-liquid interaction energy and neglects the interfacial entropy contribution. Recently, Taherian et al. [107] determined that the interfacial entropy accounts for ~30% of the total work of adhesion in graphite. Taherian et al. [108] later developed an analytical model based on the free energy perturbation theory to obtain the interfacial entropy. The primary problem with MF models is how to account for the change of the density distribution of the liquid particles as a function of the energy affinity between the solid

and the liquid. Different approaches have been suggested, such as the sharp-kink approximation (SKA) [109] and the Boltzmann distribution [78]. However, these models typically rely on either arbitrary calibrations or other adjustments that lack of a sound physical foundation. A detailed description of a wettability model and further comparison with previous investigations is presented in Section 4.1.

2.1.4 Experimental characterization of graphite and silicon surfaces

Experimentally, the wettability is determined by measuring the contact angle at the solid-liquid interface using accurate imaging techniques. These measurements are not simple, since parameters like the degree of humidity and environmental contamination can affect the outcome [110]. The wettability of graphitic-carbon is a clear example of the issues found in wettability experiments. In samples exposed to ambient conditions, early experiments reported contact angles in the range from 85.3° to 85.9° [111] and 84.2° [112] for cleavage graphite. When experiments were conducted in an ultrahigh vacuum environment, contact angles of 35±4° were obtained [113]. Recently Li et al. [110] measured a contact angle of 64.4° on graphite samples absent of environmental hydrocarbon contamination. These observations were validated by Lai et al. [114] and Wei and Jia [115], who reported contact angles of 61.1° for clean graphite surfaces.

Measuring the wettability of silicon surfaces also presents similar challenges due to the well-known reactivity of silicon with environmental oxygen. Barisik and Beskok [103] widely acknowledged this issue and reported a comprehensive review of the experimental investigations on the wettability of silicon. The contact angle of silicon has been reported to vary from 35° to 96°, but recent measurements on clean surfaces have narrowed down this range to somewhere around ~77° [116].

2.1.5 Summary of the literature review on wettability

The most pertinent aspects, for this research, about wettability were discussed in Section 2.1. A significant portion of the previous writing was dedicated to showcase the numerical methods available for determining the wettability of a solid by a given liquid. The most fundamental approach, quantum calculations, was found to be severely limited by the current computational resources available; alternatively, classical MD simulations were highlighted as the most reliable option to obtain the wetting properties of a system from an atomistic point of view. Among the MD methods available, the simulation of cylindrical droplets is the most cost effective approach. A fundamental discussion of the size-effects (line tension) inherent to any atomistic simulation helped to support this method. The difficulty to perform reliable contact angle measurements are also discussed with a major focus on carbon and silicon surfaces, as these are of significant interest for the current investigation.

2.2 Wettability transparency of graphene-coated surfaces

The changes produced in the wettability of a given surface after being coated with graphene have been a controversial subject among the scientific community. Experimental and theoretical analyses support the theories of wettability opaqueness, transparency, and translucency of graphene-coated surfaces. Shin et al. [117] found that the contact angle on a silicon carbide surface coated with graphene was similar to that of graphite and independent of the number of stacked graphene layers, indicating wettability opaqueness. Raffie et al. [118] exfoliated and functionalized graphene in aqueous solutions with varying concentrations of acetone to modify the wettability of graphene and then coated different substrates with graphene, contact angle dependence on the supporting substrate was observed. Later on, Raffie et al. [75] first reported the wettability transparency of graphene. Single and multiple layer graphene, were used to coat materials such as gold, copper, silicon, and glass. The results indicated that the

contact angle for gold, copper, and silicon was not significantly affected by coating these surfaces with a single graphene layer. Alternatively, the contact angle of glass, a highly hydrophilic material, was significantly affected by a single layer of graphene. Simulations and theoretical calculations supported the idea that surfaces for which wettability was dominated by van der Waals forces could exhibit wetting transparency, unlike surfaces like glass where the short-range hydrogen bonding is also important.

Shih et al. [78] used md simulations and a mean-field-theory-based model, to formulate the partial wettability transparency or wettability translucency theory, in which the contact angle on a graphene-coated surface is affected by the water-substrate and water-graphene interactions. This idea is contrary to that of the wetting transparency theory in which the van der Waals interactions between water and graphene are negligible and the substrate properties are transmitted through the graphene sheet. Raj et al. [76] investigated the wettability of copper, silicon oxide, and glass substrates, coated with CVD-grown graphene by measuring the advancing, receding, and static contact angles. It was reported that the addition of a single graphene layer, altered the contact angle of the substrates, while the addition of more layers had no observable impact on the contact angle. These findings were used to formulate the idea that graphene is actually opaque to wettability changes since the equilibrium spacing between the substrate and graphene is too large for any substrate force potential to be transferred to the wetting liquid.

Li et al. [110] investigated the effects of atmospheric hydrocarbon contamination on the wettability of graphene-coated surfaces exposed to air. Airborne hydrocarbons were found to be absorbed onto graphitic substrates, thereby increasing the surface energy, and hence, creating more hydrophobic surfaces. These findings indicated that graphitic surfaces are more hydrophilic than previously thought. Lai et al. [114] reported similar observations for graphene-coated copper when exposed to airborne hydrocarbons. Atomic-force-microscopy-based force reconstruction was used to perform a nanoscopic

characterization of the interface under different ambient humidity conditions, which led to the hypothesis that ambient water absorption also contributes to the observed ambient-exposure wettability dependence. The observed similarity between the wetting behavior of graphene coated surfaces and that of graphitic carbon prompted Lai et al. [114] to support the idea of the wettability opaqueness of graphene. Conversely, a recent experimental investigation conducted by Kim et al. [119] supported the wettability transparency theory when using in situ CVD-grown graphene on copper substrates, since the growth process involves surface adsorption that uniformly covers any imperfections.

Shih et al. [77] explained the wettability of graphene-coated surfaces by means of the classical Young-Dupré model. The contributions to the total work of adhesion were assumed to be additive (water-graphene and water-substrate interactions) and that the substrate-graphene interactions did not alter the total contact angle. By separating both solid-liquid interactions, a clearer understanding of the conditions for transparent and opaque wettability was obtained.

A clear lack of consensus about the wetting behavior of graphene-coated surfaces was found during this literature review. Surprisingly, experiments, theories, and simulations support the opposite behaviors of wettability transparency and opaqueness, as well as the intermediate translucency hypothesis. Therefore, it is mandatory to address this problem from a fundamental point of view to elucidate the conditions under which wettability transparency is feasible.

2.3 Hydrodynamics of nanoconfined liquids

The investigation reported in this dissertation was focused exclusively on the numerical investigation of interfacial phenomena (wettability, hydrodynamic slip, and thermal transport). Therefore, a significant portion of this section was dedicated to review the experimental techniques used to measure hydrodynamic slip in nanoconfined liquids

and the results obtained. Sections 2.3.2 to 2.3.5 are dedicated to the survey of the theoretical and numerical literature on the topic.

2.3.1 Experimental investigations of hydrodynamic slip

The adequate measuring of any interfacial or bulk property is strongly affected by the resolution of the measuring techniques. In the field of nanofluidics, the recorded magnitude of the experimental measurements of the slip length has decreased as the resolution of the measuring techniques increased [23]. The main methods for performing slip length measurements in nanoconfined liquids are the surface force apparatus (SFA), atomic force microscopy (AFM), and micro-particle image velocimetry (μ-PIV). The SFA measures the viscous force, F_h, between two surfaces immersed in a liquid of viscosity η as a function of the separation h between them [120], see Figure 2.1. This method possesses subnanometer resolution when combined with multiple-beam interferometry.

The force F_h is given by Equation (2.2) where v_a is the relative velocity of one body with respect to the other and f^* is a correction factor that accounts for hydrodynamic slip. For $f^* = 1$, Equation (2.2) is the solution of the Navier-Stokes problem in the lubrication regime. For surfaces having similar properties, Vinogradova [121] derived the solution for f^* as indicated in Equation (2.3).

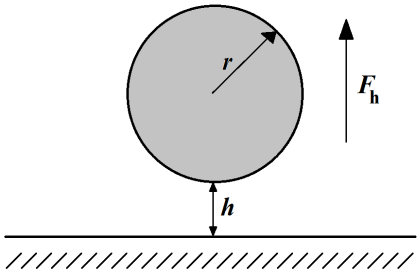

Figure 2.1: Sketch of the principle of operation of the SFA. A sphere of radius r immersed in a liquid experiences a force F_h as the distance h decreases when the sphere approaches at velocity v_a causing drainage of liquid.

$$F_{\mathrm{h}} = \frac{6\pi\eta r^2 v_{\mathrm{a}}}{h} f^* \tag{2.2}$$

$$f^* = \frac{h}{3L_{\mathrm{s}}}\left[\left(1+\frac{h}{6L_{\mathrm{s}}}\right)\ln\left(1+\frac{h}{6L_{\mathrm{s}}}\right)-1\right] \tag{2.3}$$

Zhu and Granick [60] measured large slip lengths of water and tetradecane on hydrophobic surfaces using a modified SFA. An unbounded growth of the slip length was observed as the shear rate increased while measuring slips in the order of micrometers. Very large shear rates were used and it was suggested that bubble nucleation could be induced, thus, generating larger slip lengths. More recently, Cottinn-Bizonne et al. [30] studied the hydrodynamic boundary condition of water and dodecane on hydrophilic and hydrophobic surfaces using a dynamic SFA under shear rates as large as 5×10^3 s^{-1}. The viscosity of water did not show deviations from its bulk value in confinements up to 10 nm. Water and dodecane did not slip on hydrophilic Pyrex surfaces while did slip on hydrophobic surfaces, presenting a slip length of approximately 20 nm. These results significantly disagree from those reported in Ref. [60]. Cottinn-Bizonne et al. [30] indicated that the amplitude of the oscillating pressure in their SFA never exceeded the vapor pressure of the liquids under study, while the operating conditions in Ref. [60] could have allowed some cavitation. In addition, contamination of the surfaces by hydrophobic substances was suggested as a source of discrepancy. Following the same line of research, Cottinn-Bizonne [31] extended their analysis to identify any sources of experimental error during data analysis. For example, minute errors in the determination of the separation distance between surfaces can lead to significant errors in the determination of the slip length. Water and water-mixtures were used to investigate the effects of viscosity on surfaces of different wettability. The more hydrophobic a surface is, the larger the slip length was measured with values not surpassing 20 nm.

The AFM can be used in a similar fashion as the SFA, except that that the AFM is limited to smaller probed areas [23]. Craig et al. [122] used an AFM apparatus to measure the drainage force of aqueous solutions of sucrose between a sphere (tip of the AFM) and a flat surface. Analytical models were used to fit the experimental data in order to extract information such as the slip length. It was found that the slip length was dependent upon the approaching rate of the AFM cantilever (shear rate) and the viscosity of the fluid. At small approaching velocities, no slip was found, resembling a "free system"; while at faster approaching velocities (driven systems), slip always occurred with slip lengths not surpassing 20 nm. The application of the AFM for measurements of the viscous force in nanoconfined liquids can be affected by the deflection of the AFM cantilever caused by viscous drag [123]. As the driving speed of the AFM cantilever increases more viscous drag is expected. Vinogradova [123] developed a series of models to minimize or even suppress such unwanted effects. By applying the methods of analysis developed in Ref. [123], Vinagroda et al. [124] designed an AFM probe capable of reducing the drag and using the data reduction method previously proposed, they were able to observe the no-slip boundary condition of water on hydrophilic surfaces and slip lengths of 10 nm on hydrophobic surfaces. Bonaccurso et al. [26] used AFM to measure the hydrodynamic force between hydrophilic mica and glass with aqueous solutions. Significant slip of 8-9 nm was found on hydrophilic surfaces. Slip was found to be independent of the approaching speed of the AFM probe. The hydrodynamic slippage observed on hydrophilic surfaces was justified by the large shear rates used during experiments (10^4 s^{-1}). Honig and Ducker [125] investigated the effects of rapid approaching speed of the AFM probe when measuring the viscous forces in sucrose solutions of different viscosity. A lack of a statistically significant measurement of slip length above zero was found even at shear rates as large as 2.5×10^5 s^{-1}. These findings are opposite to those by Bonaccurso et al. [26] even though similar systems were analyzed; on the other hand, these results were similar to those by Vinagroda et al. [124]. The main

reason for discrepancies is believed to originate by the means used to determine the separation between surface and probe. Conventional AFM experiments determine this distance from the sum of the displacement of the piezoelectric and the deflection of the cantilever, conversely Honig and Ducker [125] determined this separation from the intensity of scattering of an evanescent wave by the particle. On the other end of the spectrum of experimental measurements of slip length, Bushan et al. [25] measured slip lengths ranging from 43 to 232 nm on hydrophilic and superhydrophobic surfaces, respectively.

The μ-PIV technique consists in tracking the position of particles while being dragged in a liquid flow stream confined within microscale dimensions. In order to capture the interfacial phenomena, the image velocimetry analysis is strongly focused in the region near the surface where the velocity profile is sampled. Hypothetically, μ-PIV could be used to characterize flows in nanoscale conduits but as a first challenge emerges the difficulty of accurately tracking particles with dimensions of a fraction of that of the nanochannels. Moreover, at the same time that the μ-PIV resolution increases, the noisiness of the measurements increases due to larger Brownian effects as the particle tracer size decreases [23]. Therefore, μ-PIV techniques are applied to microchannels but always looking at enhancing the resolution near the surface to capture whether or not hydrodynamic slip occurs. Tretheway and Meinhart [24] used standard μ-PIV to study the slip at hydrophobic and hydrophilic channels of 30×300 μm cross-section. Fluorescent polystyrene spheres 300 nm in diameter were used as tracers and the sampled region had dimensions 25×100 μm. Slip lengths of 1 μm were obtained for hydrophobic surfaces while no-slip was observed in hydrophilic surfaces. These results were significantly higher than expectations from theoretical calculations but are consistent regarding the wettability effect. Lumma et al. [126] improved the accuracy of the velocity profiling in a microchannel 100 μm wide by cross-correlating the fluorescence response (FCCS method) of well-identified tracer particles (40 nm diameter). This method allows

decoupling flow and diffusion. They obtained slip lengths in the order of micrometers, from 0.2 – 1 μm. It was acknowledge that such results were larger and apparently not only the liquid-surface interactions were considered, but other factors such as tracer colloidal repulsive interactions may have affected the outcome of their experiments. An improvement on the precision of the μ-PIV technique was obtained by Joseph and Tabeling [32]. A microchannel of 10×100 μm cross-section was used for experiments with fluorescent beads (100 – 200 nm diameter) in water. The novelty of their research consisted in an accurate determination of the position of the wall by tracking the position of tracer particles absorbed onto the walls. Slip lengths under 100 nm were reported with uncertainties as large as their mean values. However, this investigation is the first one to report slip lengths closer to what is found from simulations.

Improvements on the particle tracking resolution using μ-PIV have been observed by applying total internal reflection fluorescence (TIRF). Slip lengths as small as 45 nm [33] and 21 nm [28] have been measured for water flowing pas hydrophobic surfaces. Li et al. [53] experimentally investigated flow dynamics in a nanochannels array, each nanochannel had a cross-section of 100 nm by 100 μm. By varying the flow rate and recording the pressure drop of the array, the shear rate was determined from an analytical model of hydrodynamic slip. From the data fitting, it was observed that there was no slip until a shear rate of 1×10^{5} s^{-1} was reached. A slip length of approximately 4 nm was measured for water on silicon at higher shear rates. A recently reported method to measure hydrodynamic slip is the quartz crystal microbalance (QCM). The QCM provides ultrasensitive and real-time monitoring of the mass on the crystal surface by monitoring changes in its resonance frequency [127]. The friction generated by the contact with a liquid damps the resonance frequency and the slip length can be calculated from the shift in the frequency. Xue et al. [127] used the QCM to measure slip lengths no greater than 2.8 nm for water on mica surfaces coated with gold and SAMs.

2.3.2 Molecular mechanisms of hydrodynamic slip

The origins of the slip and stick mechanisms of liquids flowing pass solids are early discussed in the important contributions by Thompson and Robbins [50, 51]. In Ref. [51], Thompson and Robbins explain the stick-slip phenomenon from a thermodynamics point of view instead of a hydrodynamic instability one. Non-equilibrium simulations of LJ particles in Couette flow were conducted where the friction force, displacement of the walls, and the structure of the interfacial water were recorded as a function of time and velocity of the moving wall. Solid-liquid transitions were observed on the liquid particles at the interface. Depending on the binding strength between solid and liquid atoms, crystallization was induced on the liquid and then eliminated due to the shear stress imposed during Couette flow, giving origin to a periodic phase transition behavior. Therefore, a thermodynamic origin was given to the hydrodynamic slip. In Ref. [50], Thompson and Robbins reported an extended analysis of Couette flow of LJ particles where different binding strength between the solid and liquid particles was investigated, as well as the effect of having different atomic surface density. Solid-like ordering was observed in the first two liquid layers near the solid wall. The solid-like ordering was quantified by means of the 2-D structure factor and the hydrodynamic behavior was gauged using the slip length. Solid surfaces with strong affinity for the liquid and surfaces with low density (rough surfaces) promoted high epitaxial ordering of the liquid particles. It was proposed that the boundary condition at the solid-liquid interface can be correlated to the degree of order induced in the fluid.

Based on observations of the liquid particles ordering along the normal direction to the wall, Lichter et al. [128] hypothesized that if the liquid molecules reside long enough near the wall, a dynamical description of their molecular motion is justifiable. A stochastic differential-difference equation was derived for the particles comprising the first layer near the wall, a region allowing for mass exchange between the bulk and the interfacial particles. This model was called the variable-density Frenkel-Kontorova model

(vdFK). Qualitatively, the vdFK was able to predict the same trends as MD simulations regarding the relationship between shear rate and slip length. In addition, the vdFK model distinguished between two slip mechanisms: 1) localized defect propagation (slip due to the particles exchange between interface molecular vacancies and the bulk) and 2) concurrent slip of large domains. Defect-driven slip was observed at low shear rates while concurrent slip at higher shear rates where the slip length asymptotes. Later on, Lichter et al. [129], introduced the concept of slip as a rate process, where the slip mechanism was explained as the hopping of liquid particles between equilibrium positions under de action of shear, while leaving behind a vacancy travelling in the opposite direction. Slip velocity was defined as the mean number of vacancies times the molecule hopping rate times the length per hop.

When vacancies are far apart during liquid slip, there is no relationship between the transition of one atom from one equilibrium position to another. This allows to focus on single atoms and the possibility to use transition-state theory [55]. Babu and Sathian [130] the used Eyring theory of reaction rates (transition-state theory) in which viscous flow is modeled as a chemical reaction where the fundamental process is the hopping process of one molecule from one equilibrium position to another. Thus, the liquid molecules must overcome the energy barrier imposed by their neighbors to occupy a new equilibrium position. A closed-form analytical model consisting of six equations was developed in [130]. The shear viscosity and the friction coefficient were the main outcomes of the model. MD simulations of water confined between graphene sheets and CNTs were carried out in order to directly calculate the friction coefficient and for estimating the activation energy of the liquid molecules, the latter being an input required by the analytical model. In order for this model to be valid, the shear rate must be low enough for having defect slip as indicated by Martini et al. [55]. The analytical predictions of the friction coefficient followed the same trend as the numerical

simulations; however, mismatches were found for the different confinement levels investigated.

2.3.3 Hydrodynamic slip dependence on surface wettability

A quasi-universal relationship between slip and contact angle was reported by Huang et al. [45]. Hydrodynamic slip of water flowing pass organic and inorganic surfaces was investigated by means of MD simulations of Couette flow. Spherical droplet wettability simulations were carried out to obtain the contact angle of water on different surfaces as well as the density profiles and surface tensions. Slip lengths no greater than 20 nm were observed for contact angles as large as 150°. Water in contact with surfaces with different characteristics, such as density and roughness, were investigated and interestingly the data seemed to follow a universal curve. The universal curve was obtained as an scaling formula $L_s(\theta) \sim (1+\cos\theta)^{-2}$; this expression was derived from a dual scale analysis performed on the Green-Kubo-like expression for the friction coefficient derived in Ref. [131] and the scaling of the contact angle obtained from MD simulations with respect to the energy parameter of the non-bonded solid-liquid interactions (ε), given by $\varepsilon \sim 1+\cos\theta$.

Sendner et al. [46] explored in more detail the effects of wettability on the hydrodynamic slip reported in Ref. [45]. Diamond-like surfaces with different roughness and wettability in contact with water were investigated using MD simulations. The pressure tensor method was used to determine the surface tensions and then the contact angle was calculated using the Young's equation for the different surfaces and conditions investigated. Two scaling relations were found to fit the contact angle calculations and ε. The first one was previously proposed in Ref. [45] ($\varepsilon \sim 1+\cos\theta$) and derived using a simplified mean-field model of wettability. A new and more physically sound relation $\varepsilon \sim (180° - \theta)$ was proposed from the data fitting of the MD simulations. The first relation accurately fits the data but it also suggests a drying transition at a finite value of ε, a

contradiction to the nature of the entropic repulsion of a confined interface governed by surface tension, where a finite depletion layer thickness should be expected. It was found that $L_s \sim \varepsilon^{-2}$, as formulated in Ref. [45], where from the scaling performed on the friction model of Bocquet and Barrat [131], the following scaling relation was obtained

$$L_s \sim \frac{\sigma^2 \eta D k_B T}{C_\perp \varepsilon^2}, \tag{2.4}$$

where $C_\perp$ is a geometric factor that accounts for roughness effects, σ is a characteristic length scale, D is the self-diffusion coefficient, k_B is the Boltzmann constant, and T is the absolute temperature. This simplified scaling relation with several assumptions is able to capture the relation $L_s \sim \varepsilon^{-2}$ found in MD simulations. From the observations of the behavior of the interfacial liquid structure and the solid-liquid affinity, the scaling law $L_s \sim \delta^4$ was found and provided a better alternative to describe the hydrodynamic boundary condition with the density depletion length δ given as

$$\delta = \int_0^\infty \left[1 - \frac{\rho_s(z)}{\rho_s^b} - \frac{\rho_l(z)}{\rho_l^b} \right] dz, \tag{2.5}$$

where ρ_l^b and ρ_s^b are the bulk densities of the liquid and solid, while $\rho_l(z)$ and $\rho_s(z)$ are the density profiles of the liquid and solid particles respectively. A classical theory predicts a linear relationship $L_s = \delta(\eta_l/\eta_g - 1)$ where η_l and η_g are the shear viscosities of the liquid and the gas phases at the solid-liquid interface. However, due to the size of the interface it is questionable to define the viscosity of the gas phase. Sendner et al. [46] hypothesized that the differences between experimental and simulation data of slip length measurements could be caused by the underprediction of the depletion length in MD simulations. Additionally, the presence of dissolved gases has been reported to increase the depletion length, thus the relationship between slip and depletion lengths is a good discriminant tool for comparing experiments and simulations. Surface roughness was physically incorporated by Sendner et al. [46], obtaining a reduction of the slip

length as roughness increases, increases, and a reduction of the contact angle over rough surfaces since these enhance the interaction area.

Adding to this line of discussion, Ho et al. [44] investigated the effect of substrate density on the wettability and hydrodynamic slip of water on MgO. Unlike the previous investigations, a polar solid was used to confine water; thus, the solid-liquid interactions were not only dispersive, but electrostatic as well. Wettability was artificially controlled by modifying the strength of the electrostatic interaction between water and MgO and also modifying the lattice constant of the MgO crystal. The contact angle showed a monotonic increase as the electrostatic interactions decreased since the solid-liquid attraction was reduced to only vdW forces. Interestingly, the contact angle showed an initial non-monotonic decrease as the solid density became larger, more atoms in the same volume, and such an effect was explained in terms of the effect imposed by the electrostatic surface force on the orientation of the water molecules. Below a lattice constant reduction of 10% the contact angle showed an expected decreasing trend as the spacing between atoms decreased. This is similar to Voronov et al. [47] observations and different from Sendner et al. [46]. In latter investigation the surface roughness was significantly altered such that the contact surface increased between water and the solid, whereas Ho et al. [44] and Voronov et al. [48] slightly modified the energy landscape by either changing the lattice spacing or the LJ length parameter, respectively. Moreover, Ho et al. [44] also observed an increase of slip as the solid density became greater, more hydrophilic, just like Voronov et al. [47]. This phenomenon was explained by analyzing the density contours of water at the solid-liquid interface where slip only occurred in systems where liquid molecules migrated from one absorption site to another forming density bridges, just as predicted by the theory of defect slip by Lichter et al. [129].

2.3.4 Hydrodynamic slip dependence on shear rate

Shear rate is unquestionably one of the main parameters determining the nature of the boundary condition in a nanoconfined liquid. The shear force acting on the liquid particles plays a major role as a competing force in the balance with solid-liquid binding and liquid-liquid cohesive forces. Thompson and Troian [59] acknowledged the need for a generalized form of the hydrodynamic boundary condition. A series of MD simulations of a LJ liquid with varying interaction potentials and solid densities were carried out under a wide range of shear rates in a Couette flow configuration. The effect of corrugation of the wall was observed as indicated in Section 2.3.3 as well as the reduction of slip as ε increases. Slip was found to be nearly constant for a given range of shear rates and then experienced a rapid unbounded growth after a critical shear rate, $\dot{\gamma}_c$. The shear viscosity of the liquid was calculated for all the shear rates studied and no effect was found, suggesting a Newtonian behavior under the investigated conditions. A universal functional form of the boundary condition was suggested as $L_s = L_s^0 \left(1-\dot{\gamma}/\dot{\gamma}_c\right)^{-\alpha}$, where L_s^0 is the low shear rate slip length limit and α is a fitting parameter; this expression reveals that the Navier slip boundary condition is only a limiting condition of a more general expression.

The unbounded growth of the slip length at very high shear rates was also reported by Voronov et al. [47, 48] and by Chen et al. [20] via MD modeling of Couette flow. Conversely, Martini et al. [54] observed a bounded growth of the slip length after a given critical shear rate value, corroborating their theory about the molecular mechanisms of slip. Martini et al. [54] formulated that the reason for observing an unbounded growth of the slip length as the shear rate increases was that in those simulations the wall atoms were kept fixed, hence neglecting the momentum transfer between the solid and the liquid. Martini et al. [72] used MD simulations of Couette flow with and without fixed wall atoms, a dynamical model (vdFK model, see Section 2.3.1), and a continuous model

to demonstrate their hypothesis. First, the MD simulations proved that nanochannels with rigid walls do exhibit an unbounded growth of the slip length at high shear rates. Conversely, the nanochannels with flexible walls present a constant slip length after a critical high shear rate, but the rigidity of the walls had to be calibrated to observe such a phenomenon. The vdFK model predicted that at high shear rates the slip length is shear-independent, as obtained from MD simulations with flexible walls, and tends to grow very large as the solid-liquid momentum transfer decreases (fixed solid walls). The third method was a continuous model of a compressible low Reynolds Couette flow under the effect of a potential field at the bottom wall with a slip boundary condition dependent of the solid-liquid friction force. The model was solved numerically and predicted an asymptotical growth of the slip length at high shear rates for non-zero values of the friction coefficient, and an unbounded growth after a critical shear rate for frictionless conditions.

Pahlavan and Freund [39] proposed to reassess the high shear rate limit in MD simulations by decoupling the effects of the wall model and thermostating of the liquid as these were not independently investigated in Ref. [54]. MD simulations of Couette flow were carried out to investigate the effects of the heat dissipation through the walls and the thermostating on the hydrodynamic slip. A negligible effect of the solid-liquid vibrational frequency mismatch was found on the slip length; however, a significant temperature rise was observed as a consequence of the high shear rates. A reduction of the slip length was observed due to the solid-liquid collisions increase as temperature increased. Additionally, a reduction of slip as pressure increases was observed as indicated by Bocquet and Barrat [42], using fixed solid atoms. It was demonstrated that thermostating the fluid and not the rigidity of the solid atoms leads to a rapid growth of slip at high shear rates. When the direction of flow was not thermostated, a reduction of slip to practically zero was found as the shear rate increased due to the temperature effect on the collisions frequency. These findings are opposite to what Martini et al. [54] observed;

however, it must be highlighted that in Ref. [54] the rigidity of the walls was optimized to have an efficient and stable heat dissipation. If the solid conductivity is rather low, then an overheating of the liquid atoms is expected and smaller slip lengths are in order due to increasing solid-liquid collisions (better momentum transfer).

2.3.5 Hydrodynamic slip dependence on confinement size

The small dimensions of nanochannels, comparable to the molecular mean free paths, promote an enhancement of the surface effects, such as roughness and wettability. Additionally, the liquid properties can be modified from their respective bulk values due to the strong surface effects. Some authors have investigated the threshold from nanoscale to continuum flow mechanics to identify size-affected regimes. For example, Xu and Li [40] used a hybrid numerical model in which an MD code and a continuum model were combined to investigate Couette flow through channels varying in sized from a few nanometers up to dimensions in the microscale. The results indicated that hydrodynamic slip is weakly dependent on the channel size above a ten molecular diameters. Different solid-liquid interaction parameters were used to artificially create slip, no-slip, and locking boundary conditions. Only the no-slip system was not affected by the channel size. It was proposed that by not observing differences in the interfacial fluid structure, the size-independence of slip could be explained. Two points regarding the absoluteness and relativity of the boundary conditions were made based on observations of the behavior of the shear rate and the slip-to-wall-velocity ratio. Both parameters approached their respective no-slip values as the channel size reached values of thousands of molecular diameters; this is the relativity of the boundary conditions. However, because the slip length remained constant, it was indicated that there is no transition from micro- to macroscale as long as the channel size is above ten molecular diameters. The main factor affecting the boundary conditions is the interfacial parameters; this is the absoluteness of the boundary conditions.

Thomas and McGaughey [22] investigated water flow in carbon nanotubes of diameters ranging from 1.66 to 5 nm. The flow rate was determined from the simulations data and compared with that predicted using the no-slip boundary condition. Flow enhancement was reported (ratio of the real flow rate to the no-slip flow rate calculated using the CNT diameter). The slip length was observed to be CNT-diameter-dependent as well as the viscosity of water. The viscosity was calculated from equilibrium simulations and then cross-sectional averaged to include the confinement effect. Just as indicated in Ref. [40], the slip length was found to decrease until reaching a constant value as the CNT diameter increased. When the viscosity and slip length were calculated as diameter dependent, a remarkable agreement was obtained between the MD simulations and the analytical model of flow enhancement. Zhang et al. [41] found that the mean flow velocity and the pressure gradient obtained from MD simulations followed a linear relationship as expected from a continuum model for different channel sizes. However, the slope of these lines did not follow a linear relationship with respect to the channel size. In order to analytically predict the reported non-linear behavior, the viscosity of the liquid was introduced as size-dependent and was calculated using equilibrium methods in channels of different width. By introducing the size-dependent viscosity into the analytical model, the MD data was well matched suggesting that the fluid flow in nanochannels cannot be strictly considered as Newtonian due to the inhomogeneity of the viscosity within the flow.

Interestingly, Thomas and McGaughey [22] found that the viscosity of water increased as the CNT diameter increased, but Zhang et al. [41] reported a decreasing viscosity as the wall spacing in a nanochannel increased. Giannakopoulos et al. [36] performed an unusual investigation were non-equilibrium MD simulations were used to extract the self-diffusion coefficient, shear viscosity, and thermal conductivity using equilibrium expressions. Such an unusual approach was acknowledged by the authors, but it was explained that the conditions under investigation were in the linear-response

regime and that other required adjustments were made. Eventually, the transport properties were found to be size-affected for channels smaller than ~20 molecular diameters. Conversely, Bocquet and Charlaix [23] indicated that water maintained its bulk value of shear viscosity down to confinements of 1 nm, approximately 3 atomic diameters. In addition to this, in Ref. [23], a set of publications are cited supporting the argument that viscosity remains its bulk value down to confinement levels of 1-2 nm. This would imply that if the conditions are such that the shear rate is under its critical value, and the dimensions of the confinement are large enough, above 2 nm, to not affect the viscosity of the fluid, the boundary condition would not be size-affected.

2.3.6 Summary of the literature review on hydrodynamics of nanoconfined liquids

The experimental investigation of hydrodynamics in nanoconfined fluids has been enthusiastically carried out. Several techniques have been developed in an effort to enhance the sensitivity or resolution of the measurements. A clear trend is observed in the literature to a reduction in the magnitude of the slip length as the accuracy of the measuring instruments increases. It is noteworthy how the experimental values of slip lengths approach more and more those obtained from numerical simulations.

It is clear that surface wettability and surface roughness play an important role in the determination of hydrodynamic slip. Wettability can be macroscopically quantified by means of the static contact angle, and in the microscopic realm it is a function of the solid-liquid interaction strength. Hydrodynamic slip has been strongly correlated to the contact angle by a quasi-universal relationship when surface roughness is such that the contact area between the liquid and the solid increases as roughness does. However, when wettability is artificially altered by modifying the interaction potential between the solid and liquid atoms, or by slightly varying the solid atomic density, unexpected results arise since smooth energy landscapes promote small contact angle calculations and large

slip lengths due to deficient momentum transfer. It is clear then, that there is more than the contact angle to draw a clear general picture of the hydrodynamic slip phenomenon.

The shear rate dependence of hydrodynamic slip has been reported as a divergent behavior at high shear rates, as a monotonically decreasing function, and as saturation to a constant value. Numerical evidence suggests that all these relationships are possible; however, more physically sound explanations are given once the wall and liquid properties are modeled as close as possible to experimental conditions. Evidently, more investigations have to be focused on understanding this complex relationship.

As other parameters affecting the flow behavior in nanochannels flow, the size of the channels is still a troubling one. Investigations have tried to explain such a size-effect by considering modification of the transport properties and the slip length, only the properties, or just by looking at the effect of the flow rate enhancement. Difficulties arise when comparisons between systems of different sizes and under the same flow conditions are sought.

Based on this literature review, it was clear that the nanochannels hydrodynamics simulations needed to be carried out in systems large enough, such that no size-effects were observed and under shear rates small enough to avoid the region where discrepancies exist in the literature; thus, allowing the isolation of the effect of wettability on the hydrodynamic boundary condition, which was one of the objectives of this investigation.

2.4 Solid-liquid interfacial thermal transport at the nanoscale

The thermal transport between solids and liquids has been a topic of interest since the early investigations by Kapitza at cryogenic temperatures [85]. However, the research interests moved quickly to thermal transport across solid-solid interfaces. This is not surprising, since the thermal boundary resistance is the major limitation for heat dissipation in nanoscale circuits and energy-conversion systems [132]. It has been

experimentally demonstrated that the close proximity of interfaces in silicon microelectronics modify thermal transport, thus aggravating the heat dissipation process [133]. Therefore, significant efforts have been directed towards understanding the thermal transport between semi-conductors and metals, heat transfer in nanostructured materials, development of methodologies for measuring temperature and boundary resistance at the nanoscale, and a significant amount of research on thermal transport between graphene and metals [133, 134]. Recently, thermal transport between liquids and solids at room temperature has gained more interest due to the vast applications of nanofluidics, thus creating a necessity for understanding the heat transfer between solid-liquid interfaces at the nanoscale. This literature review deals with the few attempts at experimentally measuring the thermal boundary conductance (TBC) at solid-liquid interfaces and the most representative numerical investigations on the topic.

2.4.1 Effects of surface wettability (experimental investigations)

Ge et al. [62] reported the first experimental measurements of the TBC of surfaces chemically functionalized with self-assembled monolayers, SAMs, (hydrophobic and hydrophilic surfaces) in contact with water. Time-domain thermoreflectance (TDTR) was used in conjunction with an experimental setup that allowed establishing a dominantly one-dimensional heat transfer process. Thermal boundary conductances of 100 – 180 MW/m^2K and 50 – 60 MW/m^2K were obtained for hydrophilic and hydrophobic surfaces, respectively. The large TBC difference between hydrophilic and hydrophobic surfaces was explained in terms of the water structure formed at the interface. Hydrophobic surfaces tend to form low-density atomic layers near the solid walls, thus a reduction of the thermal transport is in order due to the lack of heat carriers (water molecules).

Seven years later, Harikrishna et al. [63] conducted similar experiments as in Ref. [62] using TDTR. Chemically functionalized gold surfaces were used in order to create

different wettability conditions. The idea behind these experiments is that by having a stronger bond between solids and liquids, a better transmission of thermal energy at the interface can be achieved. The experimental results agreed in tendency and magnitude with those reported in [62]. Harikrishna et al. [63] found a linear relationship between the TBC and the work of adhesion, which is eventually proportional to $(1 + \cos\theta)$, as numerically reported in Ref. [65]. The main difference between Ge et al. [62] and Harikrishna et al. [63] investigations, is that in the latter, the same alkyl chain (thiol molecules) were used with only different terminal groups in the chain to modify the wettability, whereas Ge et al. [62] used different alkyl groups. The obtained linear relationship was highlighted to be non-universal as many factors affecting the actual behavior may change from system to system. It was indicated that the effect of the alkyl chains is negligible, since the conductance is ballistic through them. There was no claim of generality of the correlation observed, but of a possible accountability of the work of adhesion for the vibrational states affecting interfacial transport.

More recently, Mante et al. [67] used nanoacoustic waves with a femtosecond pulse width and angstrom resolution (3 Å) to probe the interfacial structure of water in contact with hydrophilic surfaces. The interfacial density was found to be up to five times greater than in the bulk, implying a good ordering close to the surface. The viscosity was practically zero near the interface, where the water appears to behave as a solid, but recovered the bulk liquid behavior away from the interface. No density layering was observed, as in MD simulations, due to the relatively high roughness of the solid surface. These experimental observations revealed that: 1) the decay of the reflectivity of the acoustic waves indicates that phonons at high frequencies are likely to be transferred into the water, and 2) that the interfacial liquid structure (impedance-matching layer) is a dominant mechanism of the TBC besides the surface roughness. These authors are the first to observe the Kapitza anomaly [85] at a solid-water interface at room temperature.

As it can be observed, the experimental investigations about thermal transport across solid-liquid interfaces are few. However, consistency is found among them regarding the effect of the solid-liquid affinity (wettability). Additionally, the recent nanoscopic characterization of the solid-liquid interface helps to validate the theoretical mechanisms of thermal transport.

2.4.2 Effects of surface wettability (numerical investigations)

Early numerical investigations of thermal transport across solid-liquid interfaces were conducted using simple lj systems (monoatomic fluids) [66, 135-137] and in many of these investigations the thermal transport is characterized using the Kapitza length (l_k)

$$L_K = \frac{\Delta T_{int}}{dT/dz\big|_l}, \tag{2.6}$$

where ΔT_{int} is the temperature jump at the solid-liquid interface and $dT/dz\big|_l$ is the temperature gradient in the liquid phase. In the vast majority of the MD simulations of heat transfer, non-equilibrium methods, in which the system is deviated from equilibrium by imposing a temperature gradient, are employed.

Maruyama and Kimura [135] calculated the contact angle in a simple LJ system by varying the solid-liquid interaction strength (ε) and observed the linear relationship ε ~ cos(θ) for a range of contact angles between 0° and 150°. L_K was found to decrease sharply as ε increased. Barrat and Chiaruttini [136] obtained a similar dependence of L_K as a function of ε, but in addition to non-equilibrium simulations, equilibrium simulations were used to calculate L_K. Although a good match was found between the two modeling approaches, it is uncommon to find investigations where the authors only rely on equilibrium simulations. The effect of the solid-liquid bonding strength was investigated and two regimes were identified by Xue et al. [66], something not reported by Maruyama and Kimura [135] and Barrat and Chiaruttini [136]. A functional fit of L_K vs a parameter that affected the solid-liquid bonding strength (α) was performed by dividing the data into

wetting and non-wetting regimes. For non-wetting liquids, it was found that L_K ~ exp(-1.9α), where an extrapolation to a finite L_K can be found at a fully repulsive condition. As for the wetting liquids, the thermal resistance was significantly smaller and $L_K \sim \alpha^{-1}$. Additionally, it was indicated that the liquid layering does not have any effect on the interfacial thermal properties of water. Later, Xue et al. [137] investigated the effect of the interfacial liquid structure on thermal transport by using the structure factor to quantify the level of ordering in the in-plane and through-plane directions. The structure factor decayed from unity to zero in a sharp manner for non-wetting conditions in the normal direction of the confinement, while it presented a less abrupt drop for wetting situations. The temperature profiles were similar between hydrophobic and hydrophilic conditions, indicating that the level of ordering plays a minor role on its thermal properties. However, it was indicated that the interfacial density depletion could have an effect on thermal transport. More recently, Torii et al. [138] formulated the same idea, but with a non-conventional definition of the density depletion.

Kim et al. [139] conducted a parametric investigation using a simple LJ system in order to unravel the functional form of the temperature jump at the solid-liquid interface. It was formulated that the temperature jump was a function of the ratio of the solid/liquid thermal oscillation frequencies $\left(\omega_{\text{wall}}/\omega_{\text{fluid}}\right)$, the solid-liquid affinity $\left(\varepsilon_{\text{sl}}/\varepsilon\right)$, wall temperature $\left(T_{\text{w}}\right)$, and temperature gradient $\left(dT/dz\big|_{\text{l}}\right)$. The following expression was obtained:

$$\Delta T_{\text{int}} = \alpha\left(T_{\text{w}}\right)\left(\frac{\omega_{\text{wall}}}{\omega_{\text{fluid}}}\right)^{4} \exp\left(-1.85\varepsilon_{\text{sl}}/\varepsilon\right)\frac{dT}{dz}\bigg|_{\text{l}}. \tag{2.7}$$

As predicted by the AMM theory, the interfacial thermal resistance increased as the ratio between the solid and liquid thermal oscillation frequencies increased. It was assumed that wettability only depended on the ratio of the LJ energy interaction parameter, a rather simple assumption. The regime under investigation was linear as the temperature

jump was linearly dependent on the temperature gradient (heat flux), thus a Navier boundary condition was proposed by incorporating the thermal oscillations, wettability, and temperature gradient dependences. Equation (2.7), when used in a continuum model showed an excellent agreement with MD data, but this was expected due to the derivation of the model using the same MD data.

Numerical investigations using real systems (real solid structures interacting with water or other complex liquids) are more common in recent publications [64, 65, 140-144]. Merabia et al. [141] investigated the heat transfer process between gold nanoparticles submerged in octane and water. The solid-water interaction potentials were calibrated by means of matching the experimentally determined contact angles. The TBC for gold in water was larger than for gold in octane, consistent with the contact angle-TBC relationship. Shenogina et al. [65] conducted MD simulations and experiments to calibrate the solid-liquid interaction potentials by matching the contact angle between water and functionalized surfaces. The TBC between water and surfaces having different contact angles was calculated using MD simulations. A significant match between the modeling results and the experimental data reported by Ge et al. [62] was obtained. Furthermore, a linear relationship $G = B(1 + \cos\theta)$ was found, where G is the TBC, B is a constant, and θ is the contact angle. Acharya et al. [64] extended the previous work [65], by conducting more MD simulations to demonstrate that the nanoscale surface roughness enhances the thermal transport between solids and water. Thermal rectification was observed; namely, different TBCs were calculated by switching the heat flow direction. Higher thermal conductance was obtained when heat travels from a highly organized medium (solid) to a disperse medium (liquid) than when it flows in the opposite direction. Acharya et al. [64] indicated that the contact angle is limited when it comes to characterize an interface, since there is no resolved contact angle on superhydrophilic surfaces, while the TBC can be used without this concern.

Goicochea et al. [142] studied the thermal transport between water and silica functionalized with SAMs. TBCs greater than 1000 MW/m^2 were calculated between silica-SAMs and SAMs-water interfaces. These results, outside the range of what has been experimentally reported [62, 63], were explained in terms of the strong covalent bond and strong –OH groups interactions in the system under investigation. Goicochea et al. [142] also studied thermal transport between water and quartz. The phonon density of states (DOS) of the interfacial atoms of water and quartz were obtained for different system sizes. Compressibility effects were observed on the DOS by down-shifting the available phonons as the length of the quartz blocks increased. Only the low-frequency spectrum was investigated since this is the range were interfacial thermal transport takes place.

Pham et al. [143] investigated the effect of pressure on the TBC at the interface between water and two solids, silicon and gold. The interaction potential between water and the two solids was calibrated by means of wettability simulations. The gold surface was superhydrophilic while silicon was hydrophobic. The interfacial water structure/layering near the hydrophilic gold surface showed negligible changes as pressure increased. It is worth mentioning that the set of interaction parameters used for gold created a large density depletion length and a significant density layering. Alternatively, the interfacial water structure near the hydrophobic Si(100) surface featured an increase in the concentration of liquid particles as pressure increased. A zero depletion length was observed for all of the silicon cases due to the large interstitial spacing in this plane. The depletion length was defined as the position of the first density peak of water. The depletion length and L_K did not change for gold under different pressures. The depletion length decreased linearly in the silicon channel as well as the Kapitza length. Unlike Xue et al. [66] a correlation between the interfacial liquid structure and thermal transport was found. This was also reported by Torii et al. [138]. Barisik and Beskok [144] analyzed a complex system involving silicon and, where the

(100) plane faces the liquid. A non-linear relationship was found between L_K and the strength of the silicon-water potential (wettability). The density of their systems was claimed to be constant at the bulk; however, density changes were observed when changing the wettability of the walls. This could have probably induced confinement effects.

2.4.3 Effects of wall temperature (numerical investigations)

Balasubramanian et al. [145] calculated the Kapitza resistance R_K at an argon-iron interface using non-equilibrium MD simulations. It was found that R_K increased in a power-law fashion with respect to the wall temperature. These results were explained based on the highly packed structure of interfacial liquid atoms on relatively hotter surfaces. Kim et al. [139] supported this observation and Murad and Puri [140] reported a power-law dependence of the temperature jump on the heat flux applied. Conversely, Carlborg et al. [146] observed that the structures of solids and liquids surrounding a carbon nanotube were unaltered during heat addition to the system. Merabia et al. [141] found a linear relationship between the temperature jump and the heating power at low heat fluxes (linear response regime), when heat was transferred between gold nanoparticles and octane, meaning a constant TBC for octane and gold. The TBC decreased at higher heat fluxes. Shenogina et al. [65] and Acharya et al. [64] also observed a linear relationship between the interface temperature jump and the heat flux.

Barisik and Beskok [144] performed non-equilibrium simulations of heat transfer of water confined by silicon walls by imposing a temperature gradient in the solid surfaces. It was consistently observed that the cold surface presented a larger thermal resistance than the hot end, except for the highly hydrophilic conditions; the differences however were not very drastic. These results indicated that the thermal boundary resistance is not solely dependent on the wall temperature. Under hydrophobic conditions, the interfacial water density profiles were similar between the hot and cold

walls; however, a greater concentration of water particles on the cold wall was observed for hydrophilic walls, thus explaining the lower value of L_K for these conditions. As expected, L_K decreases as the wall temperature increases, since the phonon density of states is higher at high temperatures. Thus, the interfacial liquid density plays a major role in the thermal transport process, but it is not entirely dictated by the wall temperature, the wall temperature also has an effect on the phonon density of states.

Shi et al. [147] reported a linear relationship between L_K and the wall temperature for a graphite-argon system and larger interface temperature jumps were observed at walls with higher temperature, while the liquid temperature gradient remained constant. These observations are contrary to the power-law functions previously reported [139, 140, 145], in addition to the wall temperature independent (in a range of 300-380 K) values of the TBC reported for water confined between silica and quartz slabs [142]. These results although confusing, they could be easily explained if the authors would have reported the relationship observed between the heat flux used and the thermal response of the systems under investigation. Namely, to report on the values of the thermal conductivity of the solids, liquids, and temperature jumps as a function of the heat fluxes applied. Since MD simulations are significantly affected by size, very large temperature gradients are imposed, and as a first requirement of any simulations, it is necessary to check the response of the system to the non-equilibrium conditions applied.

2.4.4 Theoretical model of thermal transport and wettability

In 2014, Caplan et al. [80] developed the first analytical model for predicting the TBC between solids and liquids taking into account the binding energy between the atoms of the two phases. A closed-form model based on the DMM theory and the phonon theory of liquid thermodynamics was developed. The model is formulated under the following assumptions: (i) in the hydrophobic limit, the interfacial layer of liquid at the

interface will have similar velocities to that of the bulk liquid; (ii) in the hydrophilic limit, the no-slip condition applies and the interfacial layer of liquid at the interface will assume the transverse velocities of the solid; (iii) in both hydrophobic and hydrophilic cases, the longitudinal phonon modes remain unaffected; (iv) at a hydrophobic interface, transverse modes in the solid will not contribute to thermal boundary. Their predictions accurately match the experimental data reported by Ge et al. [62]. Afterwards, Giri and Hopkins [81] further supported this theory by conducting a spectral analysis of temperature to verify that higher TBC is achieved in strongly bonded solid-liquid interfaces due to the increased coupling of low-frequency phonon modes; whereas, the interface of a poorly wetted solid acts more like a free surface to phonons. The spectrum of the phonon modes was found to increase as the bonding strength between the solid and liquid increased. The majority of the spectral contribution for the weakly bonded interfaces came from the in-plane phonon modes. More phonon modes appear as the solid-liquid bonding increases and the low frequency contributions to the spectrum are diminished on the strongly coupled surface compared to the weak one.

2.4.5 Summary of the literature review on solid-liquid thermal transport

A short overview of the recent investigations on thermal transport between liquids and solids was summarized herein. A short story of the evolution of the main findings in this area was presented, starting from the modeling of atomic to more complex solids and liquids. Some investigations reported on the idea that the changes in the interfacial liquid structure are one of the mechanisms affecting the solid-liquid transport, while others do not support this point of view. However, in general terms, there is an agreement on the relationship between the TBC and the wettability of the interfaces. In particular, the functional form of this relationship is still a controversy. Much has been done and more is

left open to investigate. For example, presenting more evidence to support/discard the theory developed by Hopkins' group [80, 81], extend these kinds of analyses to gas-solid interfaces, or even study the implications of the newly discovered wettability transparency of graphene-coated surfaces. If some surfaces coated with graphene are transparent to wettability (the contact angle of bare substrates does not change when coated with graphene), what would be the implications for heat transfer if the TBC and the wettability of an interface are strongly correlated as $G \sim 1 + \cos\theta$?

CHAPTER 3

METHODS

In this Chapter, a description of the modeling methods used during this investigation is presented. Classical molecular dynamics (MD) simulations are introduced as a reliable alternative to investigate the behavior of systems at the nanoscale. The complexity associated with the modeling of water is described. A formalized method for characterizing the wettability of solid surfaces is presented. The different methods for performing equilibrium molecular dynamics (EMD) simulations of hydrodynamic slip are presented as well as the non-equilibrium molecular dynamics (NEMD). Lastly, the methods for performing the calculation of the thermal transport across solid-liquid interfaces are described.

3.1 Classical molecular dynamics (MD)

Classical molecular dynamics (MD) is a numerical technique commonly used to calculate the equilibrium properties of a many-body system under the assumption that Newtonian dynamics govern the particles motion. Although atomic-scale systems are investigated using MD, only a fraction of the investigations require of applying quantum mechanics principles [148]. MD is a deterministic method, but given that the microstates (or configuration of the atomic structure) fluctuate over time, time tracking of the variables or properties of interest is required in order to properly define equilibrium, an equilibrium based on the time-averaged properties.

Statistical mechanics allows to predict the macroscopic properties of a system from the microscopic states. Ensemble is one of the most important concepts in statistical mechanics. This concept is defined as a collection of all possible microstates that result in the same macroscopic thermodynamic state. The Ergodic principle indicates that an

ensemble average is equal to a time-average if time goes to infinity, or at equilibrium. Hence, MD simulations are linked to statistical mechanics as time-averaged positions and velocities are used to calculate the macroscopic state of a system (ensemble average) under the assumption of classical behavior.

3.1.1 Overview of the method

An MD simulation begins from the definition of the initial conditions, particularly, the position and velocity of each particle inside the computational box. The positions must be defined as close as possible to the structure under investigation, if a solid is considered, or in such a way that overlapping or strong repulsion (due to short-range forces) of particles is avoided. The initial velocity of each particle is assigned such that a given distribution (Gaussian, Maxwellian, or random) is followed. The velocity initialization must be performed such that the total momentum of the system is zero. Thermal properties can be correlated to the velocity initial condition given by

$$k_{\mathrm{B}}T = \sum_{i=1}^{N} \frac{m v_{i,\alpha}^2}{N_{\mathrm{f}}} \tag{3.1}$$

where k_{B} is the Boltzmann constant, m is the mass of a particle, $v_{i,\alpha}$ is the velocity component α of particle i, N_{f} is the number of degrees of freedom of the particle, and T is the temperature of the group of particles. Therefore, the velocity initialization is always performed looking to represent a given initial temperature condition.

A time step, usually in the order to 10^{-15}-10^{-12} s is used to investigate the time evolution of a system, the forces on each particle are calculated in an additive pair-wise fashion (this is the most time consuming part of any MD simulation), and by using the relationship between position, velocity, acceleration, and force, the state of the system (velocity and position) is updated for every time step by time-integrating the equations of motion given by Newton's second law. Resembling an experiment, the response of the system is tracked over time; likewise, the outcome of the simulations is calculated as the

average over a period of time long enough to reduce the statistical uncertainty. In general, temperature, pressure, kinetic, and potential energy are the tracking parameters.

3.1.2 Force calculation via empirical potentials

In order to introduce the calculation of forces as required by Newton's second law, empirical potentials are used in classical molecular dynamics. The Lennard-Jones (LJ) potential is usually the most cost-effective alternative to represent the interactions between neutral particles; it is computationally efficient due to its simplicity and reliable, since it captures the main features of the interactions. The LJ potential is given by

$$V_{\mathrm{LJ}}\left(r_{ij}\right) = 4\varepsilon\left[\left(\frac{\sigma}{r_{ij}}\right)^{12} - \left(\frac{\sigma}{r_{ij}}\right)^{6}\right], \tag{3.2}$$

where ε is the energy parameter, σ is the length parameter, and r_{ij} is the distance between particles *i*-*j*. The LJ potential captures the short-range repulsion between particles in the first term (exponent 12) and the long-range attraction in second term (exponent 6) on the right hand side. Now, the force on the particles can be obtained as

$$F_{ij} = -\nabla V_{\mathrm{LJ}}\left(r_{ij}\right). \tag{3.3}$$

From the computational point of view, Equation (3.2) cannot be used due to the lack of a limit for the evaluation of r_{ij}; thus, Equation (3.2) is commonly truncated and shifted at a given value r_c, such that $V_{LJ}(r_{ij}) = 0$ for $r_{ij} > r_c$. The truncation operation does not affect the accuracy of the calculations, since for most situations $V_{LJ}(r_{ij})$ is negligible for $r_c \geq 2.5\sigma$. Other more complex potentials are available for multi-body interactions such as the Tersoff potentials [149, 150] for graphitic-carbon and silicon, which are materials of particular interest for this investigation.

Electrostatic interactions are also of significant importance when polarized particles interact. The Coulomb potential is the most common way to account for these interactions as

$$U_C\left(r_{ij}\right) = k_e \frac{q_i q_j}{r_{ij}} \tag{3.4}$$

where k_e is the Coulomb constant, and q_i and q_j are the partial charges of particles i and j. The handling of these long-range interactions is accomplished by means of algorithms, such as the Ewald summation algorithm and the particle-particle particle-mesh solver (PPPM) [151].

When molecules are considered in an MD simulation, not only the interparticle interactions are important, but also the interactions within the particles of molecules. For example, for the simple molecule of water, it is necessary to define a potential to account for the angular and linear stretching of the H-O bonds and the H-O-H angle. These potentials usually account for the modifications of the bonds and angles using an elastic model of the Hookean type as

$$U_{\text{bond}}\left(L_{ij}\right) = \frac{1}{2} K_{\text{bond}}\left(L_{ij} - L_0\right), \tag{3.5}$$

$$U_{\text{angle}}\left(\theta_{ijk}\right) = \frac{1}{2} K_{\text{angle}}\left(\theta_{ijk} - \theta_0\right), \tag{3.6}$$

where K_{bond} and K_{angle} are the elastic constants of the bonds and angles, respectively, L_{ij} and L_0 are the instantaneous and equilibrium bond lengths between particles ij, and θ_{ijk} and θ_0 are the instantaneous and equilibrium angles between particles ijk. In these models, oscillations in the magnitude of the bonds and angles are allowed, while a restitution force is exerted when a deviation from the equilibrium conditions occurs. It can be observed that by constraining the elastic properties of the system, rigid molecules can be modeled.

3.1.3 Integration of the governing equations

There are many algorithms to discretize the equations of motion, however, it has been consistently proven that one of the best is the Verlet algorithm [148]. This algorithm is highly accurate since it takes advantage of the relationship between the higher order

derivatives of the position and the physical meaning of these. The position of a particle is updated every time step using

$$r\left(t+\Delta t\right)=2r\left(t\right)-r\left(t-\Delta t\right)+\frac{F_{ij}}{m}\Delta t^{2}+O\left(\Delta t^{4}\right), \tag{3.7}$$

where it can be observed that the truncation error of this numerical scheme is of order Δt^2. The velocity can be obtained from the first derivative of the position with respect to time and it is noticeable that the second order derivative has been replaced by its equivalence with the force F_{ij} divided by the mass of the particle.

3.1.4 Thermostating

The nature of the Newton's equations of motion is to conserve momentum and thus for a system with a constant number of particles and constant volume, the energy would be kept constant as well, this is NVE or known in statistical mechanics as the microcanonical ensemble. For practical applications of MD simulations the microcanonical ensemble is far from being realistic because no experiment is conducted by fixing the energy of a system, instead, constant temperature or pressure conditions are required. Velocity rescaling techniques are applied to the equations of motion in order to ensure constant temperature conditions. These techniques go from simple rescaling to modifications of the equations of motion in order to represent a coupling between the system and a thermal reservoir. For example, the Nose-Hoover thermostat [152, 153] is a deterministic velocity rescaling technique able to reach a canonical distribution or NVT. The temperature is kept constant at an average value at the same time that allows for fluctuations of the temperature with a distribution typical for an ensemble canonical distribution. This is why this type of thermostat is widely used in the literature.

3.1.5 Boundary conditions

Most of the times, the purpose of MD simulations is to calculate a macroscopic property based on the microscopic information obtained from a system of particles. Due

to the limitations of the computational technology, the size of the systems that can be modeled is limited to hundreds of thousands of particles for super high performance computing and to tens of thousands of particles for high performance computing resources. A solution to this problem is to use periodic boundary conditions on a system of particles of a size that could allow an efficient simulation process, see Figure 3.1. This is a feasible alternative but still the size of the particles system must be large enough to capture the bulk behavior of materials. Additionally, the interaction potential cutoff must be selected such that a particle does not interact with itself in a contiguous periodic image as depicted in Figure 3.1. The particles contained within the potential cutoff radius are stored in a neighbor list, an effective technique used to optimize the evaluation of the forces. This list is revisited every given number of time steps in order to optimize the calculations.

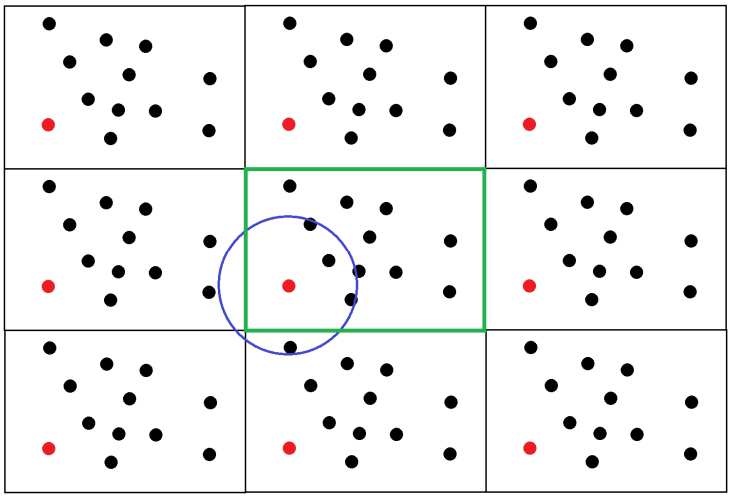

Figure 3.1: Typical computational box with a representation of its periodic images. The computational box is the box highlighted in green and the circle represents the potential cutoff.

3.1.6 Computational codes used

All of the simulations were performed using the open source MD code LAMMPS [154] developed in Sandia Laboratories and the software VMD [155] for visualization purposes. The postprocessing of the data obtained from the MD simulations was carried

out using scripts developed in MATLAB, meaning that only raw data (velocity, position, and kinetic energy) was obtained from LAMMPS to be postprocessed.

3.2 Water modeling

Water modeling is by itself a research area in the field of computational chemistry. Added to this, there is no need to list the importance of water in the many fields of science and engineering to pose it as the most important substance for humanity. Thus, having computational models that allow predicting the properties of water is of substantial interest. A thorough revision of the water models will not be conducted herein, but the reader is referred to Refs. [156, 157] for more detailed information. Even though much efforts have been dedicated to develop accurate computer water models, the complex behavior of this substance is far from being fully predicted either by MD or *ab initio* simulations [156]. No current model can predict all the water properties or its structure [157], but the vast number of models available allows to choose the most reliable one for a desired purpose. For instance, an investigation on the heat transfer properties of several water models is reported in Ref. [158] and a similar investigation on the viscous properties of water in Ref. [159].

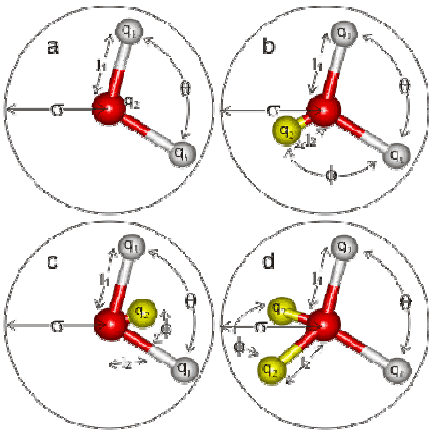

Figure 3.2: Schematics of the atomic structure employed in different water models. a), b), and c) are planar models, while d) is a tetrahedral model.

Water models are essentially constituted of two main features: the molecular structure and the interaction potential. The molecular structure can be planar or tetrahedral, as depicted in Figure 3.2. The water models can be polarizable in order to capture some of the complex interactions caused by the hydrogen bonds in each molecule. Some models are built based on the planar structure of the water molecule, and some can include artificial charges, making the model non-planar, see Figure 3.2. The water models can be flexible, allowing for distortion of the H-O bond length and H-O-H angles, or the models can be fixed, meaning that the shape of the water molecules remains unaltered. The interaction potential (V_{ij}) between water molecules accounts for attractive and repulsive non-bonded interactions as well as long range electrostatic (Coulombic) forces

$$V_{ij}\left(r_{ij}\right)=\sum_{i}\sum_{j}\left\{k_e\frac{q_i q_j}{r_{ij}}+4\varepsilon\left[\left(\frac{\sigma}{r_{ij}}\right)^{12}-\left(\frac{\sigma}{r_{ij}}\right)^{6}\right]\right\}, \tag{3.8}$$

where the pair *ij* represents the oxygen or hydrogen atoms in molecules *i* and *j*, *q* is the partial charge of the hydrogen or oxygen atoms in each molecule, and *r* is the distance between particles of individual molecules.

Table 1 summarizes the parameters of Equation (3.8) for the most common water models. The type of structure, hydrogen bond length, angles, and the partial charges of the hydrogen and oxygen atoms are also indicated [157]. MD simulations of water can be computationally expensive; however, recently the ELBA coarse-grained model has been reported as a computationally cost-effective method with an accurate prediction of the water properties [160].

The extended simple-point charge model (SPC/E) [161] was used throughout this investigation due to being computationally affordable, reliable for an accurate prediction of several water properties in comparison with other more complex models, and for being amply used in the literature, thus allowing comparisons with other investigations. In order

to keep the rigidity of the O-H bonds (1 Å) and the H-O-H angle (109.47°), the SHAKE algorithm [162] was employed. The Coulombic interactions were treated with the PPPM algorithm [151] with an accuracy of 1×10^{-6}.

Table 3.1: Parameters for some water models.

Model	Type	σ (Å)	ε (kJ mol^{-1})	l_1 (Å)	l_2 (Å)	q_1 (e)	q_2 (e)	θ°	φ°
SPC	a	3.166	0.650	1.0000	-	+0.410	-0.8200	109.47	-
SPC/E	a	3.166	0.650	1.0000	-	+0.4238	-0.8476	109.47	-
SPC/Fw	a	3.166	0.650	1.0120	-	+0.410	-0.8200	113.24	-
TIP3P	a	3.1506	0.6364	0.9572	-	+0.4170	-0.8340	104.52	-
TIP3P/Fw[2]	a	3.1506	0.6368	0.9600	-	+0.4170	-0.8340	104.5	-
PPC	b	3.2340	0.6000	0.9430	0.06	+0.5170	-1.0340	106.00	127.00
TIP4P	c	3.1536	0.6480	0.9572	0.15	+0.5200	-1.0400	104.52	52.26
TIP4P-Ew	c	3.1643	0.680946	0.9572	0.125	+0.52422	- 1.04844	104.52	52.26
TIP4P/2005	c	3.1589	0.7749	0.9572	0.154	+0.5564	-1.1128	104.52	52.26
TIP4P/2005f	c	3.1644	0.7749	0.9419	0.154	+0.5564	-1.1128	107.4	53.7
TIP5P-Ew	d	3.097	0.7448	0.9572	0.70	+0.2410	-0.2410	104.52	109.47

3.3 Atomistic modeling of wettability and postprocessing

3.3.1 Simulations set up

The wettability of different surfaces was investigated using the cylindrical droplet method. A water box was originally placed at a distance on top of a solid surface, such that there was not strong initial solid-liquid repulsion. Then, the system was allowed to equilibrate until a droplet formed. The solid atoms equations of motion were not solved for the majority of the simulations. For the cases of self-interacting solids, the bonded interactions between carbon and silicon atoms were treated using the Tersoff [149, 150] potentials and in the case of carbon, the interlayer interactions were modeled with parameters σ_{CC} = 3.41 Å and ε_{CC} = 0.289 kJ/mol [163]. Periodic boundary conditions were imposed on the three directions of the computational domain. The starting molecular setup of the simulations is depicted in Figure 3.3. The *y*-dimension of the solid

substrates was fixed as 26.16 Å and 27.15 Å for graphite and silicon, respectively. As for the *x*-dimension, the length varied between 200 Å and 300 Å depending on the size of the droplet; likewise, the *z*-dimension was kept sufficiently large to avoid any interaction between the water molecules of one box with the periodic image of the solids of another.

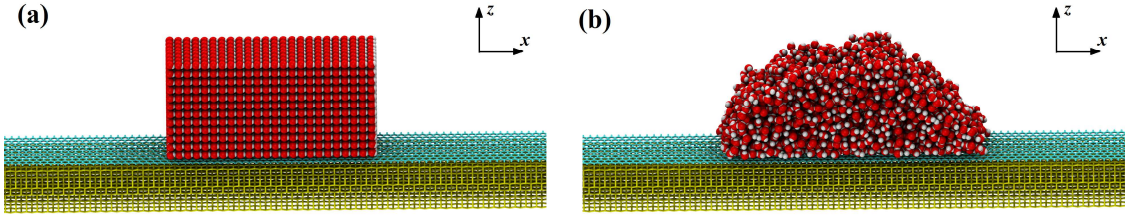

Figure 3.3: Cylindrical droplet wettability modeling stages: (a) initial configuration and (b) snapshot of a droplet in equilibrium.

The time step for integration of the governing equations was 1 fs, the neighbor lists were updated every time step, and the center of mass of the water molecules was reset to its initial position every time step in order to avoid drifting due to random perturbations. The simulation procedure was as follows: 1) energy minimization of the structures in order to eliminate any excess potential energy from the initial configuration; 2) equilibration at 298 K using a Nosé-Hoover thermostat [152, 153], one for water and one for the solid atoms when required, with a time constant of 0.1 ps for 0.5 ns; 3) equilibration in the microcanonical ensemble for 0.5 ns; 4) production run (3-4 ns) for collecting snapshots of the water molecules every 0.5 ps.

3.3.2 Postprocessing

The coordinate files obtained as snapshots were analyzed as follows. The computational box was discretized into bins of square cross-section in the *x*-*z* plane, see Figure 3.4 a), and utilizing the entire length of the computational box in the *y*-direction as the depth of the bins. The resolution of the bins was as large as 2×2 Å and as small as 0.125×0.125 Å. The position of each particle was stored into the appropriate bin for every snapshot and the mass density was calculated as the average over time of the bins count

per unit volume. Once the density of the droplet was obtained as a $\rho(x,z)$, see Figure 3.4 b), the sigmoidal function [164] depicted in Equation (3.9) was used to fit the density profile along the center of the droplet in the z-direction, see Figure 3.4 c):

$$\rho(z) = \frac{1}{2}(\rho_l + \rho_v) - \frac{1}{2}(\rho_l - \rho_v)\tanh\left(\frac{z - z_e}{d_e / 2}\right) \tag{3.9}$$

where ρ_l is the liquid bulk density, ρ_v is the vapor bulk density, z_e is the position of the equimolar distance, and d_e is an approximation of the liquid-vapor interface thickness. The vapor density was assumed zero and the data fit was carried out neglecting the highly distorted region near the solid surface [107]. The droplet interface was defined by placing markers at the outer bins where $\rho(x,z) = \rho_l/2$, then the interface was refined using a linear interpolation algorithm. The interface points were adjusted by a circular fit based on the least squares method and the contact angle was obtained from the slope at the intersection with the solid surface, see Figure 3.4 d). The contact angle calculation was the last step of the postprocessing stage and this operation was called every ten snapshots allowing accumulation of the data points over time. Hence, the evolution of the contact angle calculation can be tracked as a function of the cumulative snapshots used for the calculations. Additionally, the bulk density and the root mean square error (RMSE) of the functional fits (sigmoidal and circular) were tracked over time.

Previous investigations have reported instantaneous calculations of the contact angle as a function of time [164] and some others argued that the instantaneous calculation method is more cost effective than averaging density profiles over time [99]. However, their own results illustrate ample oscillations of the instantaneous computations and the standard deviations of their steady state calculations are quite large. By following the multi-response postprocessing method (MRPM) described above, where several outcomes of the calculations are tracked over time, a more comprehensive assessment of the postprocessing stage is accomplished obtaining precise computations.

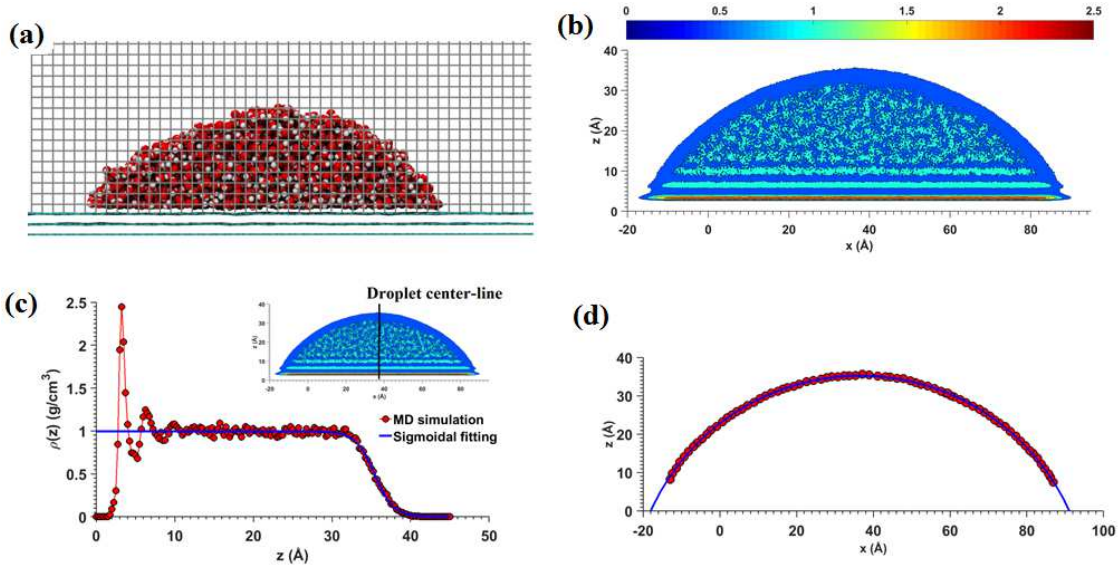

Figure 3.4: Postprocessing steps for obtaining the contact angle from MD simulations: (a) binning of the *x*-*z* plane to perform the particles count, (b) density contours obtained time averaging the particles count, (c) determination of the liquid bulk density using the sigmoidal function, and (d) delimitation of the droplet's interface from the density contours.

3.4 Equilibrium and non-equilibrium modeling of the hydrodynamics of nanoconfined liquids

3.4.1 Equilibrium models for the calculation of hydrodynamic slip

The solid-liquid friction factor can be calculated by means of equilibrium and non-equilibrium MD simulations. Equilibrium molecular dynamics (EMD) simulations are used to obtain the fluctuation of the forces generated due to the solid-liquid interactions in a nanoconfined liquid, namely, functions of time. The dissipation of these fluctuations can be analyzed by means of several theories that have been proposed over the years. Table 3.1 presents a summary of the main equilibrium models to calculate the hydrodynamic slip in nanoconfined liquids.

Table 3.2: Summary of the equilibrium models for the calculation of hydrodynamic slip.

Reference	Calculation of the friction factor	Highlights
Bocquet and Barrat [131]	$\lambda = \frac{1}{Ak_{\mathrm{B}}T}\int_0^{\infty} dt \left\langle F_x(t) F_x(0) \right\rangle$ (3.10) F_x is the total force on the solid atoms A is the area of the solid wall k_{B} is the Boltzmann constant T is the absolute temperature	▪ Linear response theory and alternatively the Mori-Zwanzig formalism were used separately to obtain equilibrium coefficients. ▪ A Hamiltonian induced an artificial shear rate into the fluid to create a Poiseuille flow. ▪ The total friction force ACF is analyzed on the solid atoms. ▪ The ACF must vanish as t → ∞, thus λ is calculated at the time when the ACF reaches zero.
Petravic and Harrowell [165]	$\mu_i = \frac{1}{Ak_{\mathrm{B}}T}\int_0^{t} dt \left\langle F_{xi}(t) F_{xi}(0) \right\rangle$ (3.11) $\mu_i = \lim_{\Delta v_{\mathrm{wall}} \to 0} \frac{\left\langle F_{xi}(t) \right\rangle / A}{\Delta v_{\mathrm{wall}}}$ (3.12) F_x is the total force on the solid atoms Δv_{wall} is the artificial relative velocity across the confined system in a hypothetic Couette flow configuration	▪ The integral of the ACF does not go to zero as t → ∞, but reaches a constant value, suggesting a smooth decay of the force ACF. ▪ Followed a similar formulation for the friction factor calculation as Bocquet and Barrat [131], but disagreed on the interpretation of such a result. ▪ Found that λ is size dependent; thus, it is not an interfacial property.
Hansen et al. [166]	$\tilde{C}_{uF_x}(s) = -\sum_{i=1}^{n} \frac{B_i \tilde{C}_{uu}(s)}{s + \kappa_i}$ (3.13) B_i and κ_i are fitting parameters, where $\lambda = B_1/\kappa_1$ $\tilde{C}_{uu}(s)$ is the Laplace-transformed velocity ACF of interfacial liquid particles $\tilde{C}_{uF_x}(s)$ is the Laplace-transformed CCF between the interfacial particles velocity and the force on the solid atoms. s is the Laplace variable	▪ Suggested to isolate the wall-affected region from the bulk in order to get the actual wall friction. ▪ Formulated a dynamic analysis of a slab near the wall with the friction force correlated with the slab velocity through a memory function. ▪ The analysis of the ACF is performed on the interfacial liquid particles.
Bocquet and Barrat [167]	$\lambda = \frac{1}{Ak_{\mathrm{B}}T}\int_0^{\infty} dt \left\langle F_{\mathrm{w}}(t) F_{\mathrm{w}}(0) \right\rangle$ (3.14) F_w is the total force on the solid atoms A is the area of the solid wall k_{B} is the Boltzmann constant T is the absolute temperature	▪ Reformulated their previous model in order to respond to criticisms about the lack of generality of their Green-Kubo formula. ▪ A non-Markovian general Langevin formulation was used to examine the fluctuations of the wall velocity and the slip velocity. ▪ Avoiding the previous assumptions and non-general characteristic of the original model, the same expression was obtained
Huang and Szlufarska	$\lambda(\omega) = \frac{1}{Ak_{\mathrm{B}}T\left[1-\alpha(\omega)\right]}\sum_i \int_0^{\infty} dt \left\langle F_i(0) F_i(t) \right\rangle e^{i\omega t}$	▪ Linear response theory was applied to a system of liquid particles after

[168]	$\alpha(\omega) = \frac{1}{Ak_B T}\sum_i \int_0^\infty dt \langle F_i(0) u_i(t) \rangle e^{i\omega t}$ (3.15) F_i is the force on individual i liquid particles u_i is the velocity of individual i liquid particles A is the area of the solid wall k_B is the Boltzmann constant T is the absolute temperature	perturbation by a given Hamiltonian. ▪ Particles were analyzed individually and interfacial interactions were assumed to be additive. ▪ The ACF analysis is performed on the liquid particles. ▪ It is suggested that in Ref. [167] a set of Langevin equations are necessary to analyze the slip and wall velocities. Thus, the model suggests a linear relationship between both variables. Something not clearly justified.

The autocorrelation and cross correlation functions (ACF and CCF) contained in Equations (3.10-3.15) were numerically evaluated using discrete time correlation algorithms, the unbiased and biased algorithms, Equation (3.16) and Equation (3.17), respectively

$$\langle B(t)B(0)\rangle_k = \frac{1}{M-k}\sum_{n=0}^{M-k-1} B(t_{n+k})B(t_n) \quad \text{where} \quad k = \{0,1,2,...,M-1\} \tag{3.16}$$

$$\langle B(t)B(0)\rangle_k = \frac{1}{M}\sum_{n=0}^{M-k-1} B(t_{n+k})B(t_n) \quad \text{where} \quad k = \{0,1,2,...,M-1\} \tag{3.17}$$

where B is a time-dependent function, such as F_x, F_i, or u_i, k is the discrete lag time index, and M is the total number of elements in the lag time sample of B.

The slip length was calculated as $L_s = \eta/\lambda$, where $\eta = 0.792\times10^{-3}$ Pa-s is the shear viscosity of SPC/E water [159]. The only exception for the calculation of L_s was for the model reported in Ref. [165], where $L_s = 0.5(H - \eta/\lambda)$ and H is the height of the confinement.

3.4.2 Non-equilibrium modeling of nanoconfined liquid hydrodynamics

Non-equilibrium MD (NEMD) simulations resemble Couette or Poiseuille flows. In these simulations, fluid flow can be simulated by confining a group of fluid particles between solid walls. Unidirectional flow can be induced by imposing an external force on the liquid particles, or by moving one of the walls at constant speed while keeping the

other fixed or both of the walls moving in opposite directions. Unlike the Couette flow, Poiseuille flow can be generated in NEMD in more than one manner. For example, an external force can be applied only to the liquid atoms in a finite region defined as inlet [72, 169] and then let the system equilibrate until a velocity profile is obtained. A second alternative to generate a pressure driven flow as reported by Zhang et al. [41]. In this method, the fluid particles are confined between three walls, one stationary and two walls moving at a constant speed in the direction of the stationary one. This resembles a system where a piston pushes a liquid inside a cylinder.

The postprocessing of the data obtained from the NEMD simulations is performed by profiling the liquid velocity. The confinement region is divided into bins where the stream velocity of the atoms is stored and then averaged over the number of particles for each time step and later over the total number of time steps in order to get a clear picture of the velocity profile. The data is fitted using a linear or a parabolic profile, depending on the case, and the slip length is evaluated as

$$L_s = \frac{\Delta u_s}{\partial u/\partial z\big|_{z_0}}, \tag{3.18}$$

where Δu_s is the difference between the slip and the wall velocity and $\partial u/\partial z\big|_{z_0}$ is the velocity gradient evaluated at the interface z_0, where z is the normal direction to the wall.

3.4.3 Simulations set up

The hydrodynamics of water confined between graphite and silicon walls was investigated. Tersoff potentials [149, 150] were used to model the atomic interactions for carbon and silicon, and an LJ potential with parameters σ_{CC} = 3.41 Å and ε_{CC} = 0.298 kJ/mol [163] was used for the interlayer carbon interactions. All of the simulations (EMD and NEMD) underwent the same initial equilibration process: 1) energy minimization for eliminating any excess potential energy from the initial configuration; 2) equilibration of the system in contact with a thermal bath at 300 K using the Nosé-Hoover thermostat

[152, 153] with a time constant of 0.1 ps during a total time of 1 ns; 3) microcanonical ensemble run for 1 ns. All of the simulations were carried out using a time step of 1 fs.

The theories summarized in Table 3.1 were implemented for the equilibrium calculation of the hydrodynamic slip length. After equilibration, the coordinates and velocities for the individual atoms were recorded every 10 fs for a total production run of 1 ns. Subsequently, the atom coordinates file was used to rerun a simulation where only oxygen-carbon interactions were considered in order to isolate the solid-liquid interactions for every single particle. The *x*-component of the force acting on each solid and liquid particle was recorded and postprocessed according to the requirements of each particular theory.

The NEMD simulations were run for 5 ns after equilibration, and then for an extra production run of 2 ns where the atomic velocities and coordinates were recorded every 0.5 ps. Only the solid atoms were thermostated during the NEMD simulations in order to ensure natural cooling through the walls [73].

3.5 Non-equilibrium modeling of thermal transport in nanoconfined liquids

3.5.1 Non-equilibrium MD modeling of thermal transport

Classical molecular dynamics simulations constitute one of the most cost-effective methods for calculating the interfacial thermal resistance between dissimilar materials. As in the case of liquid flow simulations, non-equilibrium and equilibrium methods can be applied; in this investigation, the NEMD method will be used as the EMD simulations have not been extensively used and validated [136]. In order to determine the interfacial thermal resistance or conductance, a temperature gradient is imposed to a system having interfaces. This can be accomplished in two ways, either using a fixed setup or a periodic setup, see Figure 3.5.

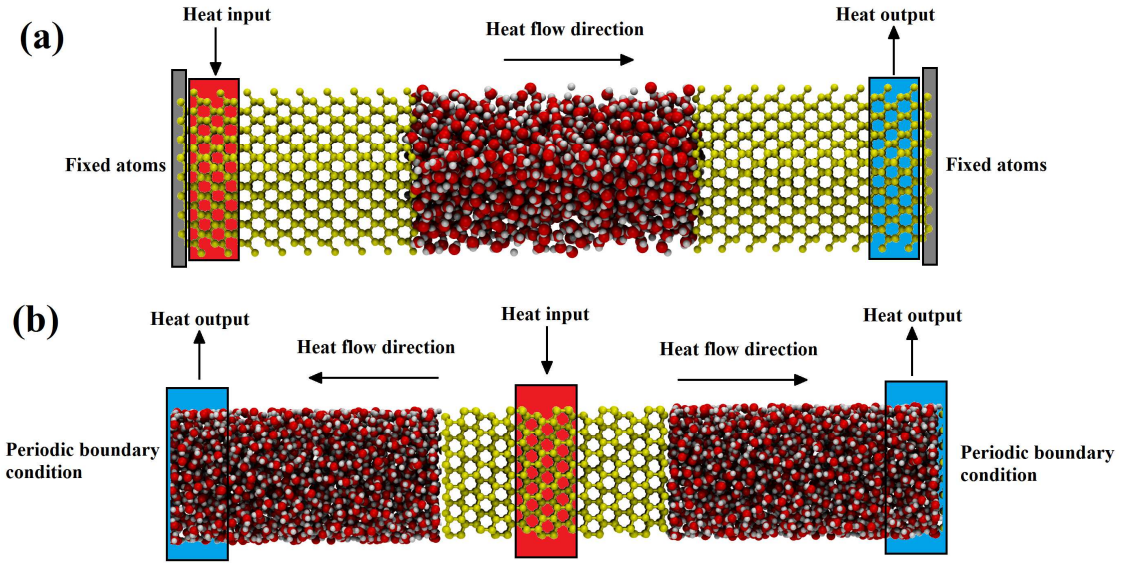

Figure 3.5: (a) fixed and (b) periodic systems commonly use to investigate thermal transport across interfaces.

In the fixed setup, the outermost atomic layers are kept fixed and the computational box is non-periodic in this direction, thus restricting the size of the system. Immediately after the fixed region, the thermal reservoirs are defined as illustrated in Figure 3.5 a). This modeling method is usually size-affected. On the other hand, the periodic setup consists in enclosing one material with two layers of the other, forming two interfaces. One of the thermal reservoirs has to be in the middle of the material in the middle, and the other reservoirs on one ends of the system in order to account for periodicity. As illustrated in Figure 3.5 b), two cold reservoirs are shown when in reality only one has to be defined, but due to the periodic boundary conditions, the system would physically look as depicted in Figure 3.5 b).

The NEMD approach can be implemented by using one of the following equivalent methods:

1) Direct thermostating [170], fixing the temperature of the thermal reservoirs and obtaining the resulting heat flux from the MD simulation.

2) Reverse perturbation method [171], the hottest and coldest atoms in the thermal reservoirs are found and then their velocities are swapped, the resulting change in kinetic energy is monitored for calculating the heat flux and the temperature gradient is tracked over time.
3) Add and subtract thermal energy at the same rate to the thermal reservoirs and track the temperature profiles over time [172].

Regardless of the NEMD method used, the thermal boundary conductance (G) is determined as

$$G = \frac{J}{\Delta T_{\text{int}}}, \tag{3.19}$$

where ΔT_{int} is the temperature difference at the interfaces and J is the magnitude of the heat flux. It has been reported that the direct thermostating method introduces an artificial thermal resistance between the thermostated and free regions [172]; additionally, it requires of an implicit calculation of the heat flux, just like the reverse perturbation method. Barisik and Beskok [172] have recommended to use the third method from the previous lists due to the explicit definition of the heat flux and because it avoids the introduction of artificial internal resistances from thermostating.

The temperature profiles of the systems depicted in Figure 3.5 were obtained from the kinetic energy obtained from the NEMD simulations and the proper utilization of Equation 3.1. It must be considered that individual atoms only have 3 degrees of freedom, while molecules such as water have 9; however, the degrees of freedom of the water molecules can be reduced to 6 if the water model employed is rigid. The water slab was divided into bins where the kinetic energy was calculated as the average over the number of particles per bin and then averaged over time. The solid slabs received a slightly different treatment because the solid atoms do not translate but only oscillate with respect to their lattice sites. Therefore, there was no need for binning but only of identifying the average position of each atomic plane. The averaging of the kinetic energy

was the same as for the water, but performed per atomic plane. Different heat fluxes were imposed on the systems and the value of G and ΔT_{int} were calculated in order to confirm that the conditions investigated were in the linear response regime. In other words, it was expected to obtained G values independent of the heat flux applied.

3.5.2 Simulations set up

The numerical procedures and parameters required for the heat transfer analysis described in this Section are essentially the same as presented in Section 3.4.3 for the nanochannels hydrodynamics simulations. The same interaction potentials, parameters, and equilibration steps were followed. The only differences are the dimensions of the systems, information that will be discussed in the following Chapters, and the procedures followed after equilibration. After the temperature and energy of the system remained constant, heat was added and removed at the same rate as indicated in Figure 3.5 a) during 2 ns in order to achieve a quasi-equilibrium condition for temperature, meaning to obtain a steady state temperature profile. The kinetic energy and position of the particles was recorded every 10 ps for a total production run of 6 ns. Postprocessing was carried out in order to obtain the temperature profiles and the thermal boundary conductance for each system investigated.

3.6 Summary

The characteristics of the numerical methods, models, and postprocessing tools used throughout this investigation have been reported in this Chapter. An overview of molecular dynamics and water modeling was presented with the objective of introducing the reader to the concepts, capabilities, and limitations of the computational tools used. The methods for calculating the contact angle, the hydrodynamic slip length, and the thermal boundary conductance from the MD simulations were described, in addition to the parameters and procedures employed to perform the numerical simulations. It is clear

that portions of important information have not been provided, such as the size of most of the systems and the number of particles contained within the confinements. This was not an omission, but a matter of discussion in the subsequent Chapters dealing with the presentation and discussion of the results.

CHAPTER 4

WETTABILITY OF GRAPHITIC CARBON AND SILICON SURFACES

The solid-liquid interactions in silicon-water and graphite-water interfaces are characterized in this Chapter. A theoretical model of wettability is presented in order to explain the effects of the interfacial liquid structure and the properties of the solid surfaces on the wettability of solid surfaces with water. This model contains a single fitting parameter and once the silicon and graphite models are calibrated, accurate predictions of the contact angle of graphene-coated surfaces can be obtained. MD simulations are conducted in order to calibrate the non-bonded interaction potential between graphite and water so that the experimental contact angle measured on clean graphitic surfaces can be numerically reproduced. The silicon wettability is parametrically studied in order to determine the macroscopic and microscopic conditions necessary to observe wettability transparency in graphene-coated silicon surfaces. The macroscopic contact angle, interfacial liquid structure, and the granularity of the solid-liquid interaction potential are used to explain the wettability transparency phenomenon.

4.1 A theoretical model of wettability based on the mean-field theory

The mean-field theory approach consists in reducing the complexity of a multi-body problem to a single-body one. Evidently, the wettability of solid surfaces is a phenomenon that allows performing such a simplification given that, the interaction between solid and liquid atoms determines the affinity for one phase with respect to the other. Mean-field theory models of wettability have been previously reported [78, 106, 108, 109] and are usually compared to the outcome of MD simulations, as both approaches use as an input the solid-liquid interaction potential and must account for the

solid properties. Noticeable mismatches have been observed between MD and numerical simulations mainly due to the improper characterization of the layering of the liquid particles at the interface [108, 109]. In order to solve this problem, a wettability model based on the mean field theory was developed herein.

The reduction in complexity of the wettability problem begins by assuming that the solid and liquid atoms interact through a LJ potential given by

$$V_{ij}(r) = 4\varepsilon_{ij}\left[\left(\frac{\sigma_{ij}}{r}\right)^{12} - \left(\frac{\sigma_{ij}}{r}\right)^{6}\right], \tag{4.1}$$

where r is the distance between two particles, ε_{ij} and σ_{ij} are the energy and distance parameters, respectively, and ij represent a pair of interacting atoms. Within the framework of the MD modeling of water wettability, ε_{ij} and σ_{ij} are the LJ parameters of the interaction between oxygen and the solid atoms since hydrogen-solid interactions are commonly neglected. Figure 4.1 depicts how the multi-body problem of wettability can be reduced to a single-body problem by considering only the interaction between one water molecule and graphite, represented as multiple monolayers of carbon atoms.

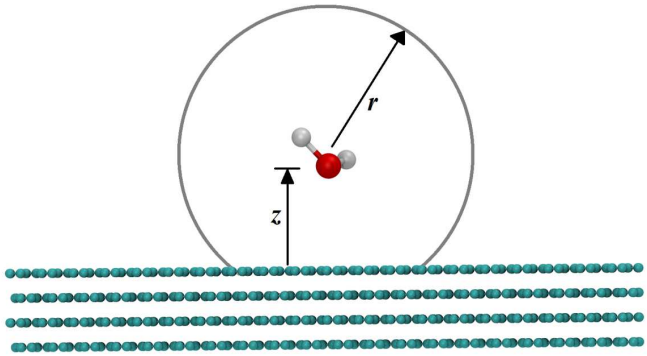

Figure 4.1: Conceptualization of the mean-field theory approach to reduce the complexity of the wettability phenomenon to a single-body problem.

If the graphite substrate depicted in Figure 4.1 is assumed to infinitely extend in the x-y plane with a constant atomic density per unit area ρ_s, the interaction potential between a water molecule and the substrate ($w_G(z)$) can be obtained by

$$w_{\mathrm{G}}(z)=\rho_{\mathrm{s}}\iint_{S}V_{\mathrm{CO}}dxdy=\rho_{\mathrm{s}}\int_{0}^{r_{\mathrm{lim}}}V_{\mathrm{CO}}\left(\sqrt{z^{2}+r'^{2}}\right)2\pi r'dr', \tag{4.2}$$

where CO stands for the oxygen-carbon pair, *S* represents the surface generated when the interaction zone of a single particle (see Figure 4.1) is truncated by a solid substrate, *r'* = x^2+y^2, *z* is assumed constant, and $r_{\mathrm{lim}}=\sqrt{r_{\mathrm{c}}^{2}-z^{2}}$ is the integration limit of *r'*. Integrating yields

$$w_{\mathrm{G}}(z)=4\pi\rho_{\mathrm{s}}\varepsilon_{\mathrm{CO}}\sigma_{\mathrm{CO}}^{2}\left\{\left(\frac{\sigma_{\mathrm{CO}}^{10}}{5z^{10}}-\frac{\sigma_{\mathrm{CO}}^{4}}{2z^{4}}\right)-\left(\frac{\sigma_{\mathrm{CO}}^{10}}{5r_{\mathrm{c}}^{10}}-\frac{\sigma_{\mathrm{CO}}^{4}}{2r_{\mathrm{c}}^{4}}\right)\right\} \tag{4.3}$$

where $w_{\mathrm{G}}(z)$ is defined in $z\in[0,r_{\mathrm{c}}]$. For the particular case of graphitic-carbon, Equation (4.3) represents the interaction potential between one graphene layer and a single water molecule. If it is assumed that van der Waals (vdW) interactions are additive, the single-particle potential for graphite ($w_{\mathrm{N}}(z)$) can be obtained by adding a number N of $w_{\mathrm{G}}(z)$ graphene potentials. This can be mathematically achieved by shifting $w_{\mathrm{G}}(z)$ a discrete distance kh_0, where h_0 is the interlayer distance between graphene layers and $k=\{0,1,2,\ldots N-1\}$ as indicated in Equation (4.4). This is illustrated in Figure 4.2.

$$w_{\mathrm{N}}(z)=4\pi\rho_{\mathrm{s}}\varepsilon_{\mathrm{CO}}\sigma_{\mathrm{CO}}^{2}\sum_{k=0}^{N-1}\left\{\left[\frac{\sigma_{\mathrm{CO}}^{10}}{5\left(z+kh_{0}\right)^{10}}-\frac{\sigma_{\mathrm{CO}}^{4}}{2\left(z+kh_{0}\right)^{4}}\right]-\left(\frac{\sigma_{\mathrm{CO}}^{10}}{5\left(r_{\mathrm{c}}+kh_{0}\right)^{10}}-\frac{\sigma_{\mathrm{CO}}^{4}}{2\left(r_{\mathrm{c}}+kh_{0}\right)^{4}}\right)\right\}. \tag{4.4}$$

A similar process can be performed in order to obtain the single-particle interaction potential for a graphene-coated silicon surface as

$$w_{\mathrm{SiG}}(z)=4\pi\rho_{\mathrm{s}}^{\mathrm{Si}}\varepsilon_{\mathrm{SiO}}\sigma_{\mathrm{SiO}}^{2}\sum_{k=0}^{N-1}\left\{\left[\frac{\sigma_{\mathrm{SiO}}^{10}}{5\left(z+\delta_{\mathrm{GS}}+kh_{i}\right)^{10}}-\frac{\sigma_{\mathrm{SiO}}^{4}}{2\left(z+\delta_{\mathrm{GS}}+kh_{i}\right)^{4}}\right]-\left(\frac{\sigma_{\mathrm{SiO}}^{10}}{5\left(r_{\mathrm{c}}+\delta_{\mathrm{GS}}+kh_{i}\right)^{10}}-\frac{\sigma_{\mathrm{SiO}}^{4}}{2\left(r_{\mathrm{c}}+\delta_{\mathrm{GS}}+kh_{i}\right)^{4}}\right)\right\} \tag{4.5}$$

where $\rho_{\mathrm{s}}^{\mathrm{Si}}$ is the atomic surface density of the silicon plane under consideration (7.83 nm^{-2} for Si(111) and 6.78 nm^{-2} for Si(100)), δ_{GS} is equilibrium separation between graphene and silicon, and h_i is the interlayer distance between silicon planes.

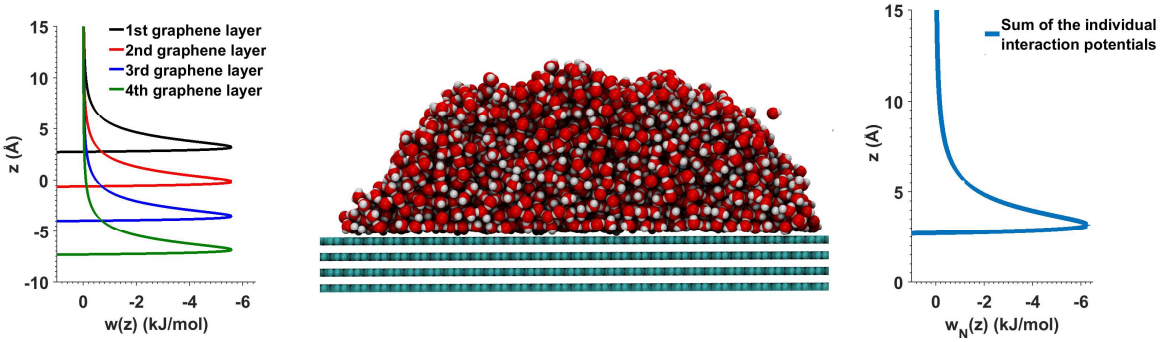

Figure 4.2: Sketch of the shifting process performed to obtain the single-particle interaction potential (left panel) and the resulting shape of the potential after adding the individual atomic layer potentials (right panel).

Shih et al.[78] proposed that the wettability of graphene-coated substrates can be explained by considering the individual contributions to the total work of adhesion $\left(W_{\mathrm{A}}^{\mathrm{T}}\right)$ by the water-substrate and the water-graphene interactions, which can be expressed as

$$W_{\mathrm{A}}^{\mathrm{T}} = W_{\mathrm{A}}^{\mathrm{WG}} + W_{\mathrm{A}}^{\mathrm{WS}} = \gamma_{\mathrm{lv}}\left(1+\cos\theta_{\mathrm{c}}\right), \tag{4.6}$$

where $W_{\mathrm{A}}^{\mathrm{WG}}$ is the water-graphene work of adhesion, $W_{\mathrm{A}}^{\mathrm{WS}}$ is the water-substrate work of adhesion, γ_{lv} is the experimental surface tension of water, θ_{c} and is the contact angle on a graphene-coated substrate. The work of adhesion has interfacial energy and entropy contributions [108] given by

$$W_{\mathrm{A}} = \frac{1}{A}\left(\Delta U_{\mathrm{WS}} - T\Delta S_{\mathrm{WS}}\right), \tag{4.7}$$

where $\Delta U_{\mathrm{WS}}/A$ is the total solid-liquid interaction energy per unit area, $-\Delta S_{\mathrm{WS}}/A$ is the interfacial entropy loss due to the liquid layering imposed on the interfacial water molecules close to the solid surface, and T is the absolute temperature. Taherian et al. [108] found that the interfacial entropy contribution accounts for as much as 30% of the total work of adhesion on graphitic surfaces. A model based on the free-energy perturbation theory was developed in [108] to obtain the interfacial entropy, but its accuracy was restricted to a very limited range of hydrophobic conditions.

An approximation to the work of adhesion for the graphene-coated silicon substrate can be easily obtained if the entropic contribution is neglected in Equation (4.7) as

$$W_A \approx \Delta U_{WS}/A = -\int_{z_{ref}}^{r_c} \rho_L(z)\left[w_G(z) + w_{SiG}(z)\right]dz \tag{4.8}$$

where $\rho_L(z)$ is the density distribution of liquid particles normal to the wetted plane, and the integration is performed from a reference value $z_{ref} \approx 0$ to a large value of r_c in order to capture the bulk behavior. The definition of a proper $\rho_L(z)$ function is the major limitation of these kinds of wettability models. Taherian et al. [108] found that a Boltzmann distribution significantly overestimates the concentration of interfacial liquid particles and that the sharp-kink approximation SKA [109] generates poor predictions of wettability when compared to numerical simulations. A simple but effective calibration to the Boltzmann distribution in which $\rho_L(z) = \rho_{L,0}\exp\left[-w(z)/\eta k_B T\right]$, where $\rho_{L,0}$ is the bulk density of the liquid particles, $w(z)$ is the total single-particle interaction potential, and η is the only tuning parameter of the model. Due to the calibration performed, the theoretical model using $\rho_L(z)$ as previously indicated was called the Boltzmann calibrated model or BCM.

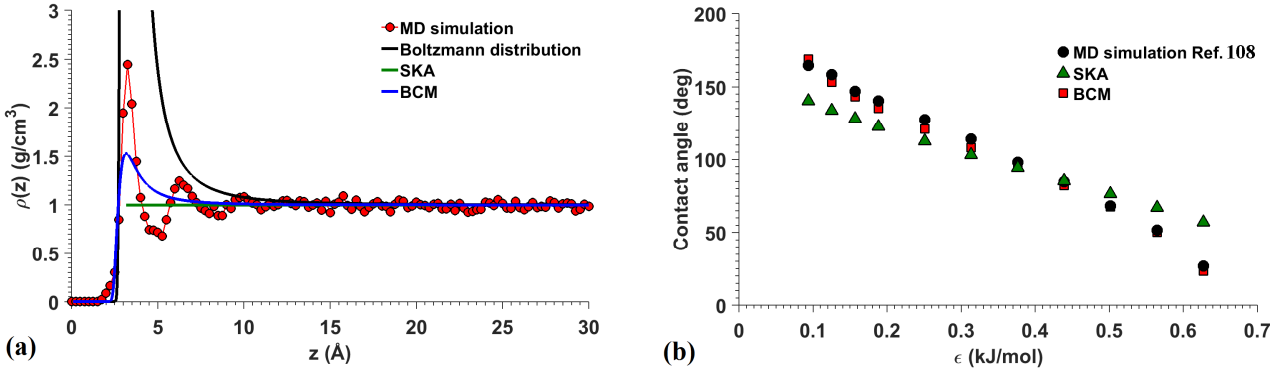

Figure 4.3: (a) Comparison between the interfacial liquid density profiles obtained from MD simulations and the different theories. (b) Comparison between MD simulation results of wettability and implementations of different theories.

Figure 4.3(a) illustrates a comparison between the theoretical descriptions of $\rho_L(z)$ with the density layering obtained from MD simulations. The SKA clearly does not account for the interfacial layering or the effect of the binding strength (amplitude of the density peaks) and the Boltzmann distribution overestimates the interfacial concentration of liquid particles. Alternatively, the BCM proposed here captures some of the features of the liquid layering near the interface within the range observed in MD simulations. An implementation of the BCM is depicted in Figure 4.3(b) where it can be observed that a remarkable match is found with the MD simulation results reported in Ref. [108], where η = 7.1 was the fitting parameter. By neglecting $\Delta S_{WS}/A$, the BCM model was self-compensated under hydrophilic conditions where $\Delta S_{WS}/A$ is important but underpredicted $\Delta U_{WS}/A$. Alternatively, slight underpredictions of the contact angle were observed for hydrophobic surfaces where the magnitude of $\Delta S_{WS}/A$ is small but the theoretical values of $\Delta U_{WS}/A$ was slightly smaller than MD calculations; see the Supplemental Information of Ref. [173]. These observations allowed to justify ignoring $\Delta S_{WS}/A$ in the calculation of the work of adhesion. This model was used for investigating the wettability of graphite, silicon, and graphene-coated silicon.

4.2 Calibration of the atomic carbon-water interactions

Before performing the calibration of the carbon-water interaction potential, a case study was considered to showcase the reliability of the MRPM (see Section 3.3.1). Three droplet sizes having of 2,376, 4,050, and 7,920 molecules were simulated in a cylindrical droplet fashion with fixed solid atoms (two layers of graphene) and using the same LJ parameters (σ_{CO} = 3.19 Å and ε_{CO} = 0.3135 kJ/mol). Figure 4.4 illustrates the analysis of the contact angle calculations as a function of the accumulated data sets over time for a water droplet made of 4,050 molecules using different binning resolutions. Each and every simulation was analyzed in the same fashion. Figure 4.4(a) depicts the evolution of the contact angle over a postprocessing time of 3 ns. The contact angle calculation

exhibits a rapid drop from 150° to 105° in a time frame of approximately 0.15 ns for every binning resolution analyzed. It is noteworthy that all the evolution curves followed similar paths for different bin sizes. The inset of Figure 4.4(a) depicts a subtle difference of approximately 1.25° from peak to peak along the curves of maximum and minimum resolution, which may indicate a negligible effect of the bin size for this particular case. However, there is a clear trend towards convergence to a single curve as the binning resolution increases, leading to a more accurate calculation of the contact angle.

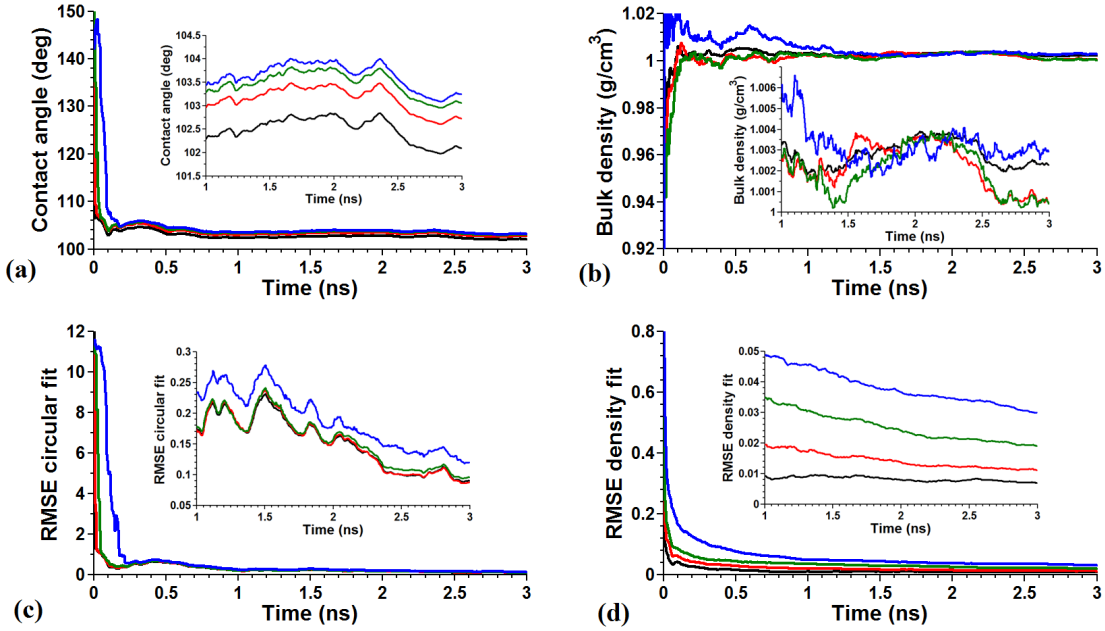

Figure 4.4: Implementation of the formalized multi-response postprocessing method for calculating the contact angle from MD simulations data. analysis of a water droplet made of 4,050 molecules with binning resolution of 2×2 Å (black lines), 1×1 Å (red lines), 0.5×0.5 Å (green lines), and 0.25×0.25 Å (blue lines). (a) Contact angle calculation as a function of time, (b) bulk liquid density as a function of time, (c) root mean squared error (RMSE) of the circular fit used to define the interface, and (d) RMSE of the sigmoidal fit (Equation (3.9)) used to obtain the bulk density of the liquid particles.

After gathering data sets for 0.5 ns, it appears that the contact angle calculation converged. However, the MRPM provides a set of quality indicators to be examined before performing a final calculation. For example, the bulk value of density obtained

from the sigmoidal fit proposed in Equation (3.9) was tracked and depicted in Figure 4.4(b). Larger bins can enclose more atoms and smoother density profiles are obtained towards a converging value of 1 g/cm^3. On the other hand, the finest bin resolution curve is the one that shows more noisiness compared to the other density curves. For the particular case analyzed here, it can be said that all density curves converged after 1 ns. The range of variation of density is not significant in this particular example; however, this variable is fundamental and must be tracked. The most dramatic assessment of the calculations quality comes from the evaluation of the root mean squared error (RMSE) of the circular fit used for representing the liquid-vapor interface see Figure 4.4(c). The RMSE was chosen over the least squares R^2 parameter, since the RMSE imposes much higher penalties to the quality of a functional fit. It is demonstrated that although the contact angle curves begin showing steady state behaviors very rapidly, the quality of the circular fit operation is quite poor and significantly affected by the bins size. By means of visual inspection of several snapshots of the circular representation of the interface, a threshold value of RMSE ≤ 0.3 was adopted as an indicator of reliable calculations. Such a condition is eventually achieved after gathering data sets for 1 ns. The last quality discriminant investigated was the RMSE of the sigmoidal function fit to the density profile along the centerline of the droplet depicted in Figure 4.4(d). Unlike the circular representation of the droplet interface, the representation of the density profiles was an easier task, due to the resemblance between Equation (3.9) and the MD-calculated density profiles. Similar to the circular fit, the RMSE of the density profile is affected by the binning resolution in the same fashion. Clearly, smaller bins are unable to capture good statistics as fast as larger bins.

After evaluating all the information and taking into consideration the threshold values for the quality indicators (RMSE), the contact angle for the molecular setup whose analysis was reported in Figure 4.4 was obtained by averaging between 1 ns and 3 ns. The resulting contact angle was 106.01±0.38° for an individual run and 106.25±0.84° for

the average of three simulation runs under different initial conditions, all cases using the finest binning resolution. The contact angle calculations obtained by following the MRPM are remarkably accurate and repeatable results were obtained after analyzing different independent runs.

The calibration of the carbon-water interaction potential was performed such that the recently reported value of θ_∞ = 64.4° on a free-of-contaminants graphite surface [110] was obtained from MD simulations. The linear relationship $\varepsilon_{CO} \sim \theta$ [95] was used to perform this calibration. First, a random hydrophilic simulation (ε_{CO} = 0.4974 kJ/mol while keeping σ_{CO} constant) resulted in a pair (ε_{CO},θ_∞) = (0.4974 kJ/mol, 57.7±0.24°) in addition to the one already found (0.3135 kJ/mol, 103.56±0.38°). Then, a linearly interpolated value of ε_{CO} = 0.4736 kJ/mol was determined for an objective θ_∞ = 64.4°. The results of the MD simulations for ε_{CO} = 0.4736 kJ/mol are depicted in Figure 4.5, where it can be observed that θ_∞ = 64.7±0.32°. The calibration of the graphite contact angle to 64.4° was further verified by running a simulation with only 2,376 water molecules (for simplicity and assuming size independence) interacting with three graphene layers. The resulting contact angle was 64.13±0.14°. Then, the same simulation was repeated allowing the graphene layers to interact and the resulting contact angle was 63.56±0.26°. In conclusion, it was fully verified that the combination of parameters σ_{CO} = 3.19 Å, ε_{CO} = 0.4736 kJ/mol, and r_c = 15 Å can be used to obtain θ_∞ = 64.4° from MD simulations in graphitic surfaces.

Figure 4.6 depicts a comparison between the BCM with MD contact angle calculations of graphitic-carbon gathered throughout this investigation. Simulation results obtained using LJ potential parameters proposed by other authors to predict different θ_∞ values of graphitic surfaces as well as the current calibration to 64.4° were used as inputs to the BCM. It must be indicated that the analytical values of θ_∞ were obtained for $N \rightarrow \infty$ and $r_c \rightarrow \infty$. Overall, a good match between MD simulations and the analytical calculations was found. Even though the BCM requires of the calibration of a fitting

parameter, its capabilities to match MD simulations should be highlighted since this is something not observed in previous investigations proposing similar models [46, 78, 108, 109]. The main difference arises in a better accountability of the density profiles of liquid particles by scaling the Boltzmann distribution function and the lack of a reference distance required evaluate the energy interaction integral, see Equation (4.8).

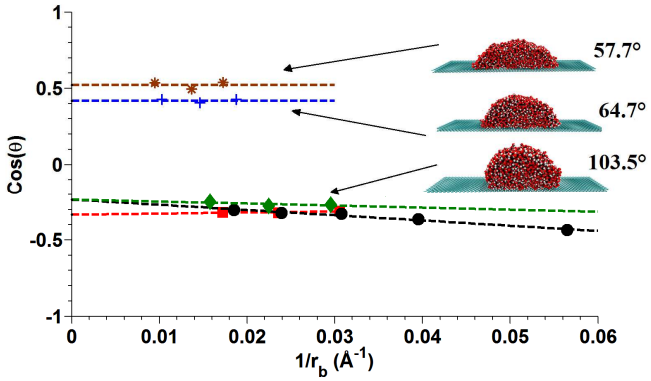

Figure 4.5: Size effects in the calculation of the contact angle on graphite surface and calibration of the contact angle using the scaling law $\varepsilon_{CO} \sim \theta$ [95]. Symbols: Werder et al. [95] results (circles); same case as in Ref. [95] using the MRPM and cylindrical droplets (squares).

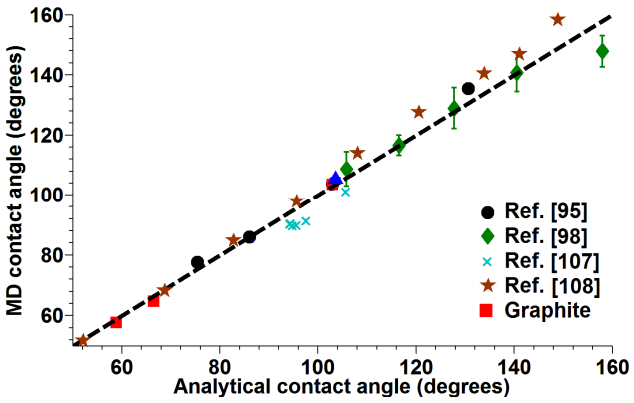

Figure 4.6: Comparison between different investigations on the wettability of graphitic-carbon wettability and the theoretical predictions of the BCM.

4.3 Wettability of different silicon crystallographic planes

The wettability analysis of Si(111) and Si(100) was systematically conducted similar to that of graphite. Using the calibrated LJ parameters proposed by Barisik and

Beskok [103] to obtain the experimental contact angle of water on silicon, contact angles of 87.7±0.36° and 103.6±0.45° were obtained for Si(111) and Si(100), respectively. In their investigation Barisik and Beskok [103] used the hemispherical droplet method to calibrate the LJ potential parameters to obtain θ_∞ = 88°. It has been demonstrated here and in previous investigations that the hemispherical and the cylindrical droplet methods converge in the macroscopic limit. Interestingly, convergence was found but not for the same silicon plane. From a theoretical point of view, it could be expected for the Si(111) surface to be more wettable than the Si(100) surface due to the marked difference in their atomic planar density if the water molecules and silicon atoms interacted through the same pairwise potential. Similar observations about the contact angle dependence on the substrate atomic density have been reported [44]. Despite of being an issue, these results opened a door of opportunity for testing the BCM with different atomic structures.

In order to cover a wider range of wettability conditions for silicon, different contact angles were obtained by fixing the silicon-oxygen interaction potential parameter σ_{SiO}, while varying the energy parameter ε_{SiO}, similar to the previous investigation by Barisik and Beskok [103], where the analysis was focused on the wettability of the Si(100) plane. It was found that using the same range of the silicon-oxygen interaction potential for the Si(100) and Si(111) surfaces, leads to the observation of different contact angles due to the silicon structure anisotropy. This observation was verified by MD simulations and theoretical calculations in Figure 4.7. For comparison purposes, in terms of the observed contact angles, the contact angle of the two silicon surfaces was adjusted from ~50° to ~150°, a range amply covering the experimentally reported wettability of clean silicon [103, 174]. Three independent simulation runs were conducted for each ε_{SiO} value and the contact angles on the two silicon surfaces are illustrated in Figure 4.7. The MD simulation results were consistent with the theoretical predictions of the BCM, where η = 2.7 for Si(111) and η = 2.1 for Si(100), although η = 2.5 produces good prediction for both surfaces. The theoretical predictions appeared to be more accurate for

hydrophilic surfaces than for hydrophobic surfaces. This behavior is understandable, since the BCM compensates the lack of accountability for interfacial entropy in hydrophilic conditions (due to an underprediction of the energy contribution to the work of adhesion) and slightly overpredicts the work of adhesion in hydrophobic surfaces, as demonstrated in the Supplemental Information of Ref. [173].

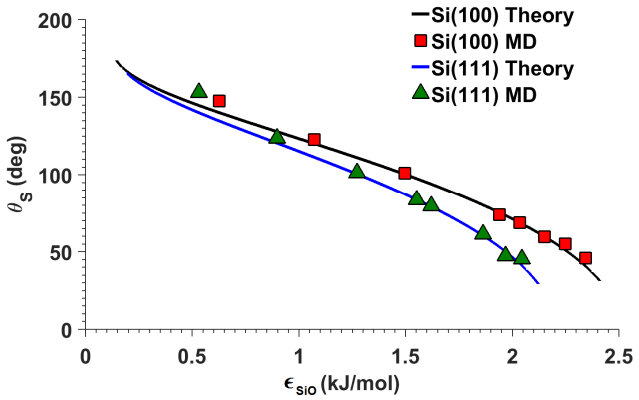

Figure 4.7: Wettability of different silicon planes as a function of the silicon-water interaction strength.

Barisik and Beskok [103] observed some degree of entrainment of water molecules into the interstitia of the Si(100) surface through snapshots of the molecular setup in equilibrium, they also reported density profiles but the resolution of their contours was very poor. The density contours in Figure 4.8(a) properly captured the entrainment of water molecules in every interstitium of the Si(100) plane and Figure 4.8(b) depicts a snapshot of the water molecules penetrating the large spaces between Si atoms in the plane (100). Such a phenomenon was not observed for the Si(111) surface or the graphitic surfaces whose atomic surface densities are 7.83 nm^{-2} and 37.24 nm^{-2}, respectively, whereas the atomic density of the Si(100) plane is 6.78 nm^{-2}. The surface density between silicon planes is not significant, but the closely packed bilayer structure in the normal direction of the (111) plane (see Figure 4.9) contributes to not observing water penetration.

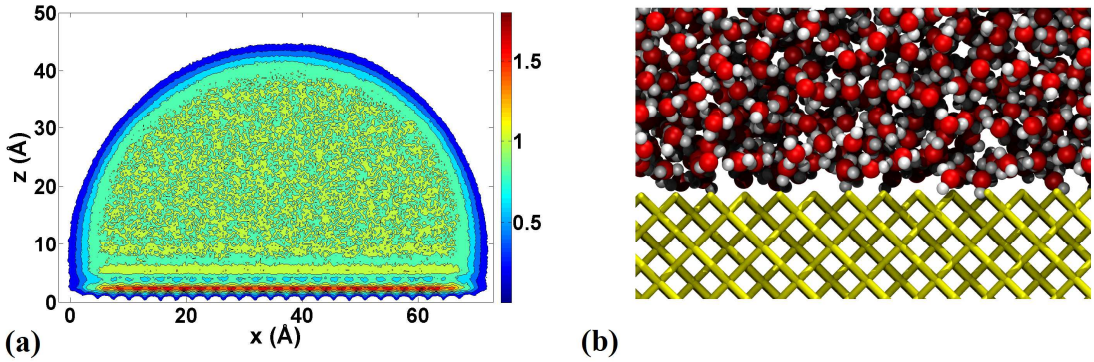

Figure 4.8: Si(100) wettability analysis: (a) droplet density contours (g/cm^3) where entrainment is observed on the lower plane, z = 0, and (b) snapshot of water molecules at the interface with Si(100).

4.4 The wettability transparency of graphene-coated silicon surfaces

The structure of the graphene coated system used for this investigation is depicted in Figure 4.9, where h_i can take a fixed value (h_3 = 1.357 Å) between Si(100) planes or alternating values (h_1 = 0.784 Å, h_2 = 2.352 Å) in order to capture the triple-bilayer periodic structure of Si(111), see Equation 4.5 for details of the structure accountability in the BCM model. The equilibrium distance between the graphene layer and the substrate was varied as illustrated in Figure 4.9. The structure of Tersoff graphene [175] was stretched 4% in order to create periodic graphene-coated silicon structures. Figure 4.9(a) depicts the unit cell used to create the graphene-coated Si(111) structure. The Si(100) imposed a greater challenge for matching with graphene, but a good periodic structure approximation was found by considering a unit cell of a combined structure which was made 5 unit cells of graphene and 4 of Si in the x-direction and 11 cells of graphene and 5 of Si in the y-direction. The stability of the graphene-silicon structures was investigated by obtaining the equilibrium configurations from independent MD simulations of stretched graphene supported on silicon. It was found that the structures maintained their original periodic configuration after equilibration.

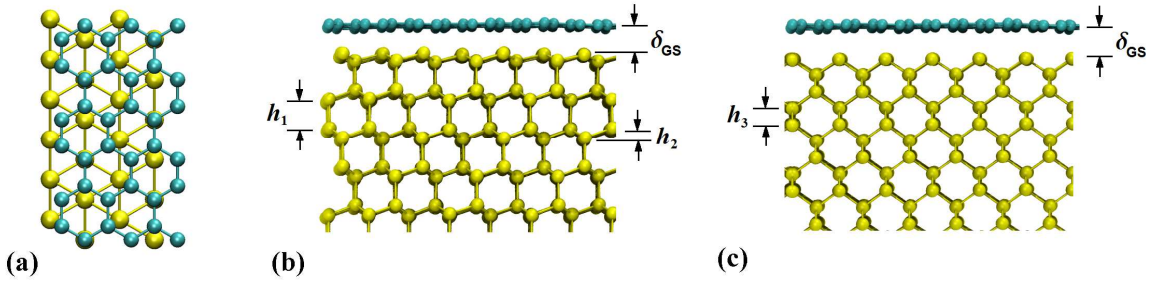

Figure 4.9: (a) Unit cell for generating graphene-coated Si(111), (b) underlying structure of a graphene-coated Si(111) surface where h_1 and h_2 characterize the periodic triple bilayer, and (c) underlying structure of a graphene-coated Si(100) surface where h_3 is the inter-plane distance.

4.4.1 Macroscopic conditions required to observe wettability transparency

Once the silicon and carbon models were calibrated, the contact angles of graphene-coated silicon were predicted by the BCM and compared with MD simulations as depicted in Figure 4.10. Because the solid atoms lack of internal degrees of freedom during the numerical modeling, the equilibrium distance between silicon and graphene, normally determined by the interaction potential between the silicon and carbon atoms, was defined as δ_{GS} = 3.0 Å, a reasonable distance between a graphene layer physisorbed onto a substrate. On this aspect, some authors have indicated that $\delta_{GS} \approx$ 2.0 Å [90-92] and others have suggested that $\delta_{GS} \approx$ 3.55 Å [163] through mixing rule approximations. The value δ_{GS} = 3.0 Å was taken as a reference to investigate the accuracy of the BCM when predicting the MD wettability of a more complex system than bare silicon. Figure 10 illustrates that the theoretical BCM is able to match the contact angles on graphene-coated surfaces calculated by means of MD simulations. The fitting parameter η = 7.25 was used to predict the wettability of graphene-coated silicon due to the proximity between graphene and water. The observed trends coincide, although not as accurately as in the case of bare silicon surfaces. This can be attributed to the fact the wettability of the coated surface is not as sensitive to ε_{SiO} as the bare silicon due to the increased spacing

between the water molecules and the silicon substrate. It was observed that the graphene-coated versions of the silicon surfaces have contact angles that vary between ~74° and ~84°, and the widest gap between the theoretical predictions for both surfaces is smaller than 2°, a small difference hardly captured by MD simulations; nevertheless, the numerical data fall within this range for the majority of the values of ε_{SiO}.

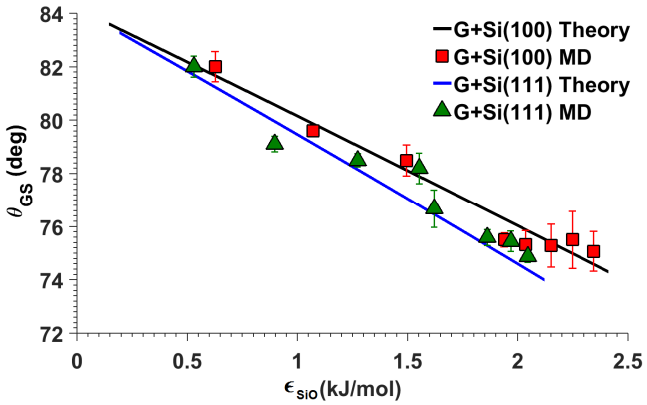

Figure 4.10: Wettability of graphene-coated silicon surfaces as a function of the silicon-water interaction strength.

The theoretical conditions required to achieve wettability transparency as a function of the macroscopic contact angle on a silicon substrate are illustrated in Figure 4.11. The equilibrium distance between graphene and silicon was varied from 3 Å to 5 Å just for purposes of performing a parametric analysis on the BCM, it is important to note that $\delta_{GS} > 3.5$ Å is not physically plausible due to the short range nature of the interatomic forces. Closely resembling experimental data, the MD simulation results fall along the curve for $\delta_{GS} = 3.0$ Å which also corresponds to the molecular setup used to obtain the data illustrated in Figures 4.11(a) and (b). The region where wettability transparency was expected appears as a shaded slab and encompasses a condition such that the variation of the contact angle of the substrate with respect to its graphene-coated version is ±5°. The results indicate that the exact wettability transparency for $\delta_{GS} = 3.0$ Å is achievable if the contact angle of any of the two silicon surfaces is ~76°. Recent

investigations have reported that the contact angle on a clean silicon surface is ~77° [174] and the wetting transparency of graphene-coated silicon surfaces was first reported by Raffie et al. [75]. Therefore, the theoretical and numerical "experiments" reported in Figure 4.11 support previous investigations suggesting the possibility of the wetting transparency of silicon surfaces in addition to explore the overall macroscopic wetting behavior of graphene-coated silicon surfaces.

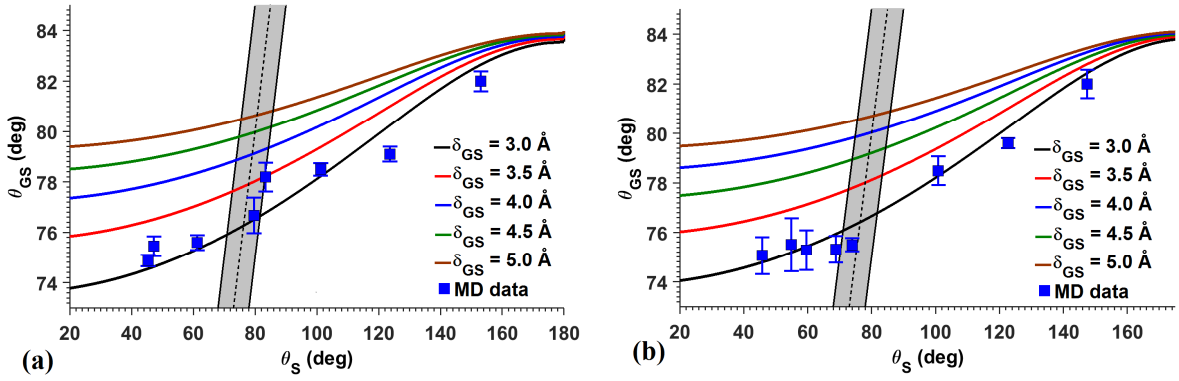

Figure 4.11: Macroscopic conditions for wettability transparency of (a) graphene-coated Si(111) and (b) graphene-coated Si(100). The shaded regions represent the wettability transparency region with ±5°. All data points have vertical and horizontal error bars.

4.4.2 Microscopic conditions required to observe wettability transparency

An analysis of the microscopic conditions giving origin to the wetting transparency phenomenon was conducted by analyzing the liquid interfacial structure and potential energy field contributions to the wetting transparency phenomenon. The changes induced in the equilibrium structure of liquid particles when a silicon surface is coated with graphene are depicted in Figures 4.12 and 4.13. The upper panels illustrate the density contours of droplets for hydrophobic and hydrophilic bare silicon surfaces and the bottom panels depict the same surfaces coated with graphene. As indicated before, the large interstitial spacing between silicon atoms in the (100) plane cause water entrainment (see the right upper panel of Figure 4.12). Because of the low water-silicon

affinity under hydrophobic conditions, no entrainment was observed in this case, (see the left upper panel of Figure 4.12). The interfacial structure of the liquid molecules was greatly modified when the silicon was coated with graphene. Water molecules did not penetrate the solid structure due to the lack of potential energy wells caused by a high atomic surface density (see Figure 4.12 lower panels). Instead, a uniform liquid layering was observed in the vicinity of the solid.

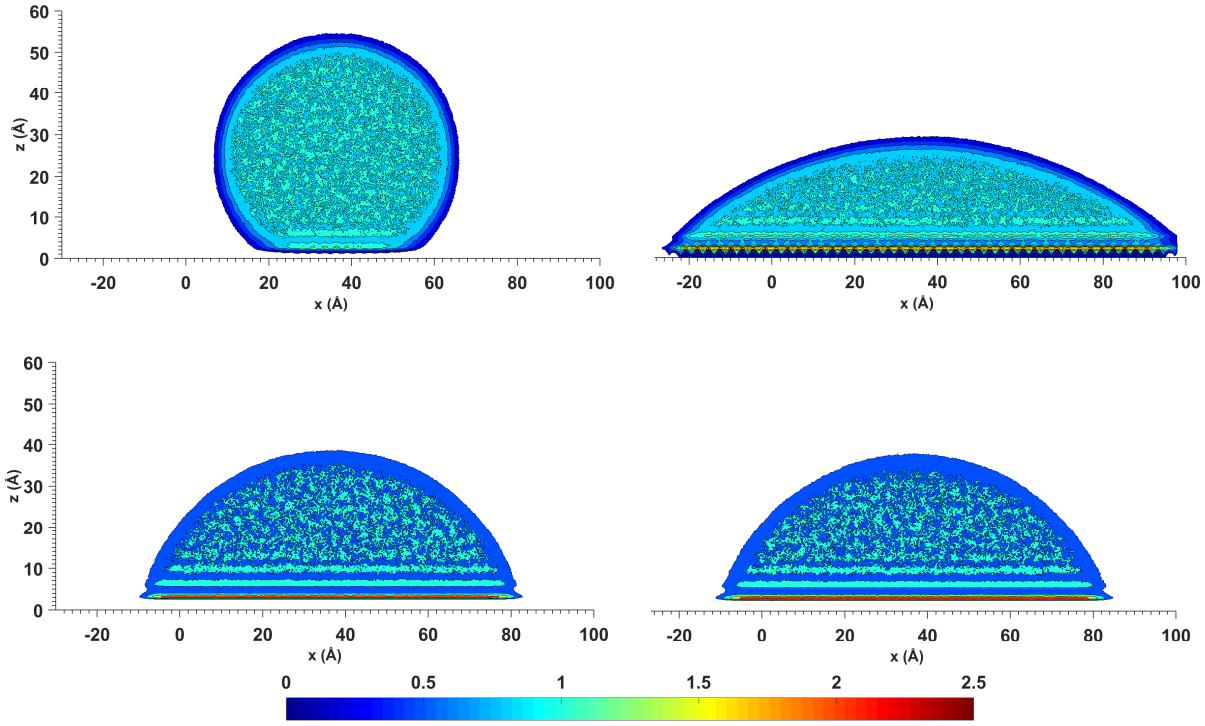

Figure 4.12: Density contours of water droplets on Si(100) surfaces (upper panels) and graphene-coated Si(100) surfaces (lower panels). Hydrophobic silicon surface, left panels; hydrophilic silicon surfaces, right panels. The scale is in g/cm^3.

Figure 4.13 depicts the density contours of water droplets on a Si(111) surface; similar to the previous case, the left- and right-hand panels are hydrophobic and hydrophilic silicon surfaces, respectively, while the lower panels are the same surfaces coated with graphene. The larger atomic surface density of the Si(111) plane clearly eliminated the entrainment effect previously observed on Si(100). Here, the interfacial

water structure consisted of a high-density layer near the solid liquid interface, similar to what was observed on the graphene-coated versions. The equilibrium separation between the water and the solid atoms is different in both surfaces due to the interaction potential parameters; this is strongly related to the length parameter σ_{ij}.

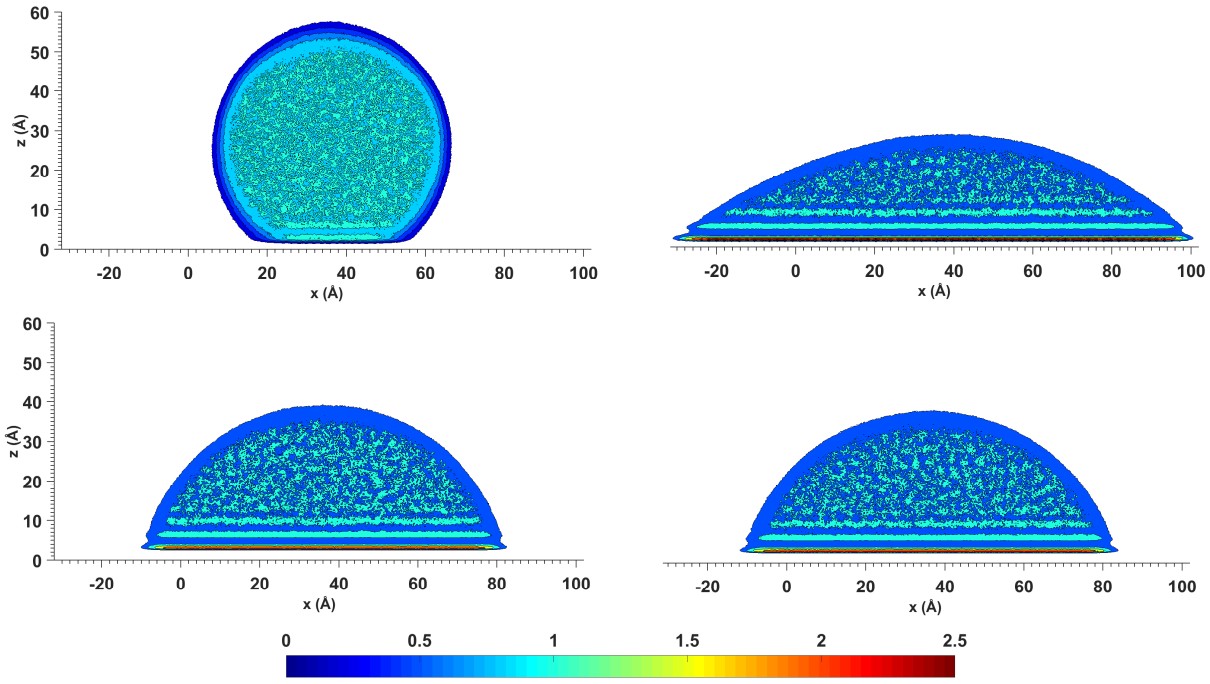

Figure 4.13: Density contours of water droplets on Si(111) surfaces (upper panels) and graphene-coated Si(111) surfaces (lower panels). Hydrophobic silicon surfaces, left panels; hydrophilic silicon surfaces, right panels. The scale is in g/cm^3.

Figure 4.14 reports on the changes observed in the interfacial water structure under hydrophobic (top panel), hydrophilic (middle panel), and transparent (bottom panel) conditions for both, silicon and graphene-coated silicon surfaces. It should be noted that the observed changes in the density profiles for the graphene-coated silicon surfaces were minimal; therefore, only one curve is depicted in each panel shown in Figure 4.14. Under hydrophobic conditions, major changes in the liquid interfacial structure were observed after silicon is coated with graphene; see Figure 4.14(a). A large depletion layer was observed onto the Si(100) surface as a consequence of the low water-

silicon affinity and low atomic surface density, whereas the larger concentration of solid atoms per unit area on the Si(111) surface alleviated this depletion effect. The graphene-coated version of the hydrophobic substrates significantly modified the interfacial liquid structure due to the relative stronger affinity between the carbon atoms and water.

Figure 4.14(b) illustrates the microscopic changes produced after coating a hydrophilic silicon surface. The hydrophilic Si(100) surface exhibits liquid-layering due to a stronger solid-liquid interaction. The first density peak on the Si(111) surface increased and even surpassed the magnitude of that of the graphene-coated silicon. The differences observed on both silicon surfaces can be related to the difference in the atomic surface.The Si(100) plane allows for liquid molecules to become entrained in the interstitia and water density depletion occurred; alternatively, the more closely-packed Si(111) structure did not allow entrainment of particles, and as a consequence the liquid particle concentration near the solid surface increased as the water-silicon interaction force increased, (see Table 4.1).

The wettability transparency condition for both silicon surfaces (mildly hydrophilic surfaces) is depicted in Figure 4.14(c). It was expected to find similarities between the interfacial water structure on silicon and graphene-coated silicon surfaces under wettability transparency conditions. Such an assumption was partially and visually verified for the Si(111) surface and its graphene-coated counterpart. Both systems exhibited a similar interfacial structure of liquid particles once the shift between both density curves (~1 Å) was eliminated. When the interfacial concentration of liquid particles was calculated, from zero to the valley after the first density peak, it was found that similarities indeed arise under wetting transparency conditions for both silicon surfaces, see Table 4.1. It is noteworthy that the density profile at the interface ($z = 0$) is not zero for the Si(100) plane. This is due to the entrainment observed of some liquid particles into Si(100). The interfacial concentration of liquid particles increases on the bare silicon surfaces as the energy parameter ε_{SiO} increases while it remains fairly

constant on the graphene-coated cases. Interestingly, the concentration of particles is quite similar only under wettability transparency conditions.

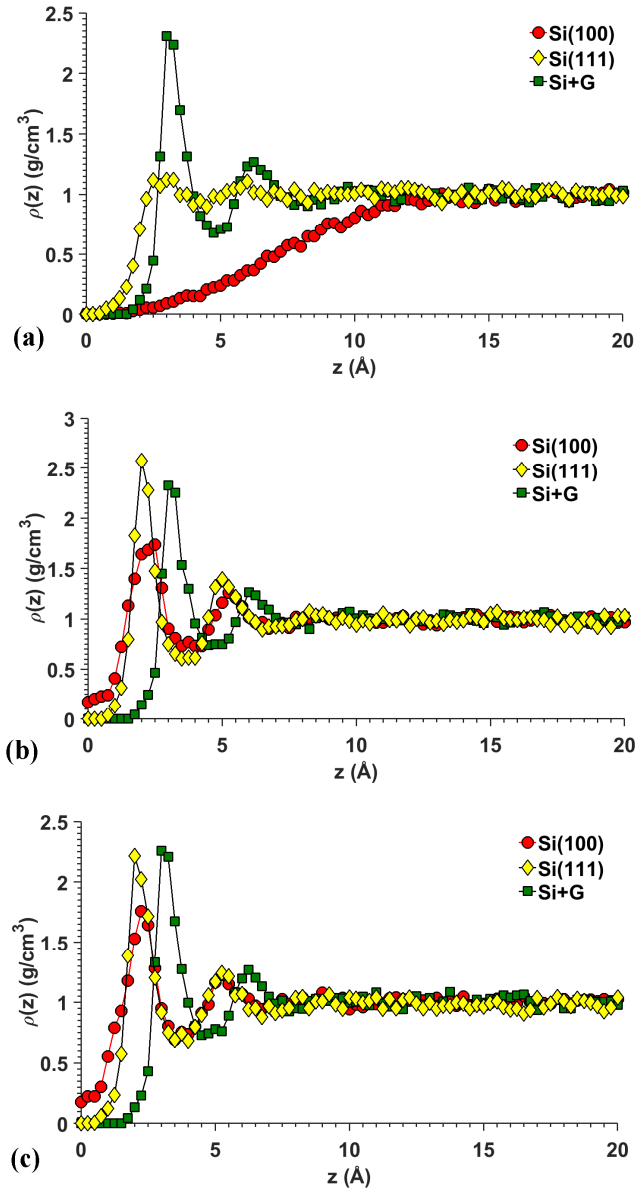

Figure 4.14: Droplets center-line density profiles along the z-direction of Si(100), Si(111), and graphene-coated silicon surfaces under (a) hydrophobic, (b) hydrophilic, and (c) transparent conditions.

Lastly, Figure 4.15 depicts the attractive potential energy contours between different silicon planes and graphene-coated silicon in an effort to explain the wettability

transparency phenomenon and the wettability of the different silicon surfaces. When a silicon surface that exhibits a strong hydrophilic behavior is coated with a single layer of graphene, the strong silicon-water interaction is inhibited by increasing the effective distance between these particles. The equilibrium distance between graphene and silicon, plus the equilibrium distance generated between graphene and water, given by the carbon-water interaction potential, account for the diminished influence of the substrate on the water molecules, (see Figure 4.15). The water-graphene interactions tend to dominate the overall wettability behavior as the surfaces become less hydrophilic, until saturation is reached at superhydrophobic conditions. In these situations, it is apparent that the hydrophobic substrate serves as a supporting material and the observed contact angle is approximately that of a single layer of graphene, an argument theoretically supported by Figure 4.11. Taking an alternative view, it appears that the underlying substrate properties affect the wettability of the supported graphene layer. The silicon potential energy granularity is lost when it reaches the water molecules ($z \approx 6$ Å) as indicated in Figure 4.15. This helps to explain why the two graphene-coated silicon surfaces exhibit similar contact angles and why the pristine surfaces exhibit different wettability. Figure 4.15(c) illustrates how the highly dense concentration of carbon atoms in a graphene layer produces a rather smooth energy landscape for the water molecules, a feature that will significantly affect the momentum and heat transfer at these interfaces.

It appears that the strong granularity of the energy field created by the Si(100) surface affected the interfacial water structure in such a way that water density depletion is observed; nevertheless, these particles contribute to the total work of adhesion and are accounted for in the interfacial concentration of liquid particles. The rough Si(100) interface represents a major contribution to the wetting behavior of the bare substrate. However, when a graphene coat is applied, the underlying silicon only adds to the solid-liquid interaction by means of a smooth energy landscape.

Table 4.1: Interfacial liquid particles concentration per unit area on silicon and graphene-coated silicon surfaces (nm^{-2})

ε_{SiO} (kJ/mol)	Si(100) Bare substrate	Graphene-coated	ε_{SiO} (kJ/mol)	Si(111) Bare substrate	Graphene-coated
0.6271	0.4539	10.5079	0.5306	6.2648	10.4419
1.0709	8.8950	10.5946	0.8973	8.4494	10.4944
1.4955	9.7170	10.6640	1.2736	9.1698	10.5243
1.9393	10.5242	10.6218	1.5534	9.6221	10.4050
2.0358	10.5684	10.2719	1.6209	9.6569	10.4174
2.1516	11.5913	10.3166	1.8621	11.0525	10.4577
2.2481	11.6854	10.8280	1.9682	11.3746	10.5022
2.3445	11.7557	10.5601	2.0454	11.7265	10.5466

*The shaded region indicates the wettability transparency condition.

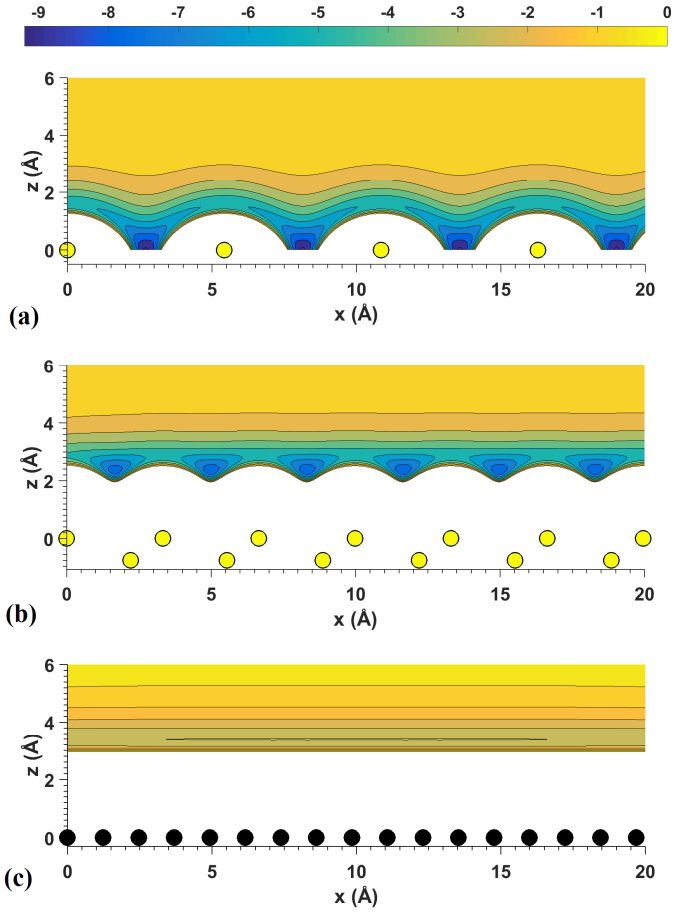

Figure 4.15: Corrugation of the solid-liquid interaction potential for (a) Si(100), (b) Si(111), and (c) graphene-coated silicon surfaces (only showing the carbon atoms). The units are kJ/mol and only the attractive potential is depicted.

As for the Si(111) the same contribution to the energy potential landscape experienced by the water particles was observed, in addition to presenting similar interfacial liquid structures under wetting transparent conditions. Overall, although similarities were found between microscopic properties under wetting transparent conditions, the intricate combination of these gives origin to a physical macroscopic property such as the contact angle which eventually serves as a good discriminant for the conditions required to observe wetting transparency.

4.5 Summary

The characterization of the graphite-water, silicon-water, and graphene-coated-silicon-water interactions was conducted using MD simulations of droplet wettability. This process was conducted in an effort to build a solid foundation for the momentum and heat transport investigations reported in the upcoming Chapters, two phenomena strongly affected by the surface chemistry. In the process of conducting this wettability investigation, the benefits and reliability of a formalized method to postprocess the data generated from MD simulations of droplet wettability were reported for the first time. The MRPM features several quality assessments of the contact angle calculations, it can be used to determine the stability and convergence of the simulations, and the obtained results have a low error margin when compared with several independent simulations. The wettability of graphitic carbon was calibrated for the first time in order to capture the recently discovered wettability of carbon surfaces free of environmental hydrocarbon contaminants. Likewise, the wettability of different silicon planes was characterized in a range from hydrophilic to hydrophobic conditions.

A theoretical model of wettability (based on the mean-field theory) of bare and graphene-coated silicon surfaces was developed in order to validate and further understand the numerical simulation results. With the application of this theoretical

model (BCM), it was possible to explain the differences and the apparent anisotropy effect on the wettability of different silicon planes. Improving upon previous wettability models, the BCM accurately captures the solid-liquid interaction strength effect and includes the characteristics of the solid surfaces, such as the planar atomic density and the underlying structure of the plane facing water. The downside of this model is the necessity for calibration, but once calibrated for silicon and graphite, it was possible to fully predict the wettability of graphene-coated silicon surfaces under different solid-liquid interaction conditions.

The conditions required to observe wettability transparency in graphene-coated silicon surfaces were theoretically and numerically determined. A remarkable agreement was found between simulations and theory. This allowed using the numerical and theoretical results to determine the macroscopic and microscopic conditions required for wettability transparency to occur. It was found that the underlying substrate must have a given contact and that the interfacial concentration of liquid particles must be similar between bare and graphene-coated silicon surfaces (something reported for the first time). These results were supported from analyses of the interfacial liquid structure and the granularity of the solid-liquid interaction potential at the interface.

CHAPTER 5

HYDRODYNAMIC SLIP IN NANOCHANNELS AND ITS RELATIONSHIP WITH WETTABILITY

In this Chapter, a critical assessment of the relationship between the hydrodynamics of nanoconfined water and wettability is reported. In Chapter 4, the carbon-water and silicon-water interaction potentials were calibrated by means of size-independent MD simulations of droplet wettability. In the current Chapter, the surface chemistry characterization was taken as the foundation to investigate the nature of the hydrodynamic boundary condition in nanochannels. Firstly, a considerable portion of this Chapter is dedicated to evaluate the accuracy of the different equilibrium theories available to predict hydrodynamic slip. Secondly, hydrodynamic slip was investigated in silicon nanochannels with different crystallographic planes facing water, and lastly, the wettability transparency phenomenon was introduced to obtain a deeper understanding of the slip-wettability relationship.

5.1 Critical assessment of the hydrodynamic slip length as a surface property

Some numerical investigations suggest that the nature of the hydrodynamic boundary condition in nanoconfined liquids is a surface property, i.e., there is a unique dependence on the solid-liquid affinity and roughness. For a comprehensive review on this topic, please go back to Section 2.3. The mathematical expressions derived from the equilibrium theories of hydrodynamic slip also support this idea. Therefore, previously to conduct any investigation of the wettability effect on the hydrodynamic boundary condition, a critical assessment of the current theories to predict hydrodynamic slip was conducted.

Figure 5.1 illustrates the system used to conduct the first part of this investigation, which consists of a water block confined between graphite plates (three graphene layers). The dimensions of the system were L = 6.39 nm and W = 6.64 nm, while the channel height was varied as H = 3 – 8 nm. The area was kept constant, the size of the confinement was changed, and the number of liquid particles was varied accordingly so that the same bulk pressure and density were obtained in the middle of the channel. By doing this, compressibility effects are eliminated and only the confinement size is involved to determine the nature of the slip length (L_s). The carbon-water interaction potential was modeled using the parameter calibrated to obtain a contact angle of 64.4°, as indicated in Chapter 4.

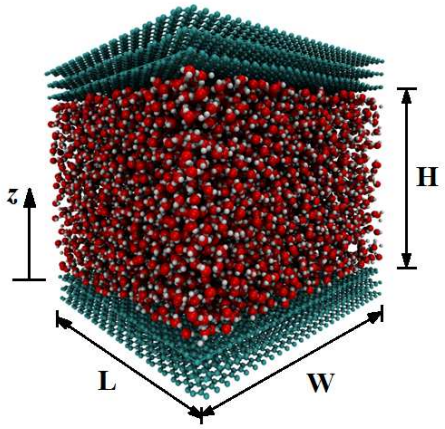

Figure 5.1: Nanoconfined water between graphite plates used to investigate the accuracy of the equilibrium theories of hydrodynamic slip.

Equilibrium simulations were conducted in the canonical ensemble as indicated in Section 3.4.3 for 1 ns; afterwards, the water particle coordinates were recorded every 0.5 ps during a total time of 0.5 ns; additionally, the shear stress per water molecule was recorded every 0.5 ps for a total production run of 3 ns. The water density profiles were calculated by dividing the height, H, of the nanochannels into bins where the number of water molecules was counted and averaged over time. The size of the bins was small enough to capture the fine interfacial details and large enough to avoid losing statistical

significance. Figure 5.2(a) depicts the water density distribution along the height of nanochannels of different sizes. Clearly, the bulk density of water is similar for every system, ~1 g/cm^3. More importantly, the interfacial water structure is similar for the different nanochannels. The equilibrium calculations of L_s are based on short-range interactions between the solid walls and the water molecules; hence, the importance of the interfacial concentration of liquid particles.

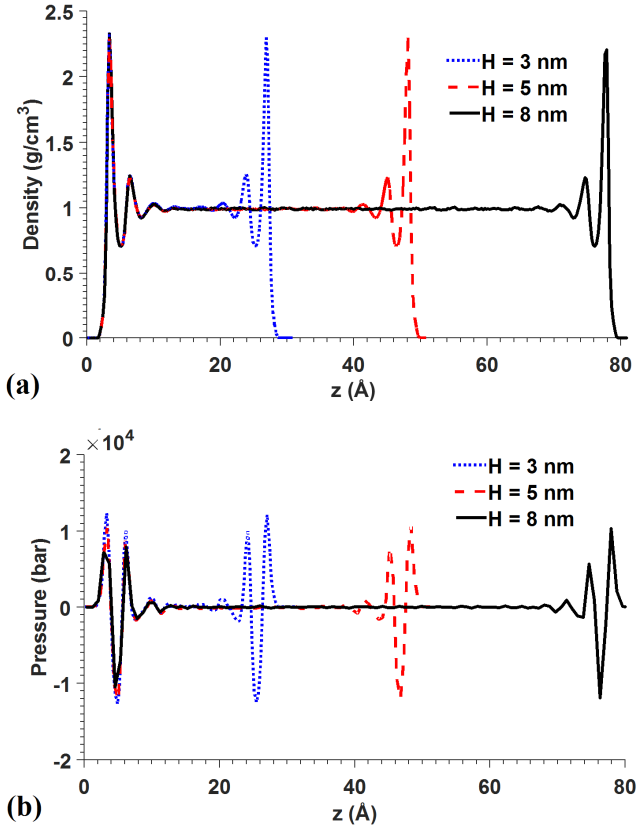

Figure 5.2: (a) density and (b) pressure profiles in water at different levels of confinement.

Figure 5.2(b) illustrates the pressure profiles along the height of nanochannels of different sizes. The observable bulk pressure is on average ~0 bar, but a closer look at the pressure curves reveals a variation between -200 and +200 bar. Unlike the density profiles, the interfacial pressure features small differences for the different channels; however, this can be explained due to the well-known noisiness associated with MD

calculations of pressure, especially at solid-liquid interfaces where water particles concentrate.

5.1.1 Calculation of the friction coefficient λ using different equilibrium theories

After verifying that similar bulk and interfacial liquid water properties existed in the different nanochannels, the characteristics of the calculations of the friction coefficient, λ, were investigated using different theories. Initially, the effect of the lag time, τ, used in the evaluation of the time-correlation function (TCF) formulated by Bocquet and Barrat [131, 167] was analyzed. Data was recorded for a total time of 1 ns using a nanochannel height of H = 5 nm. Different lag times were used to evaluate Equation (3.10) with a time interval of 0.1 ps between TCFs. Figure 5.3(a) depicts the calculation of λ using an unbiased algorithm (Equation (3.16)) for the evaluation of the TCF and the values of λ are depicted as running integrals, with the lag time normalized, so as to observe if saturation occurs. The evaluation of λ using Equation (3.10) appears to be reliable only for the shortest lag time, τ = 2 ps, just as indicated in [131]. As the lag time for the evaluation of the TCF increases, the noise associated with the calculations increases accordingly such that there is no observable plateau. Huang and Szlufarska [168] observed a similar behavior when employing Equation (3.10).

If the TCF of Equation (3.10) is evaluated with a biased algorithm, see Equation (3.17), the previous calculation of the friction coefficient is significantly modified as illustrated in Figure 5.3(b). The noisiness of the integral of Equation (3.10) decreases and λ seems to saturate at a value similar to that for τ = 2, 5, and 10 ps. The difference in the calculated values using the biased and unbiased algorithms is due to the normalization performed on the discrete calculation of the lag-time-shift in the time-correlated functions. The unbiased algorithm weighs the sum of the products as $M - k$, which is consistent with the number of operations performed (k approaches M). Alternatively, the biased algorithm always normalizes the number of products by M. If the analyzed

function *B*, see Equations (3.16-3.17), loses correlation as the lag time increases, it is expected that the last terms in the series of Eq. (10) account only for weakly correlated products and the weight of the normalization given by $M - k$ would not dampen the expected noise. Thus, the biased algorithm features a smaller standard deviation for the calculation of the TCF's and it is usually preferred by the signals and systems community [176].

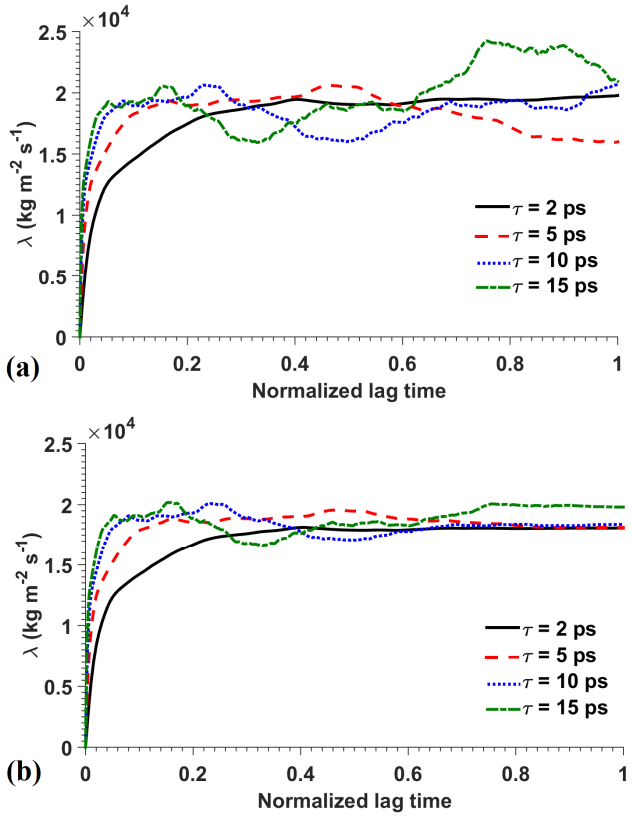

Figure 5.3: Calculation of the friction coefficient λ using Bocquet and Barrat's theory [131, 167] with (a) unbiased algorithms and (b) biased algorithms for the evaluation of the time correlation functions.

It has been demonstrated that using biased algorithms for the evaluation of the TCF in Equation (3.10) leads to smoother time-dependent λ curves, which could be one of the reasons why some authors report noisy and others smooth λ curves. In most publications, little or no information is given about the specific details of the

postprocessing stage, but as has been shown here, drastically different results can be obtained by simply modifying the algorithm used for data postprocessing.

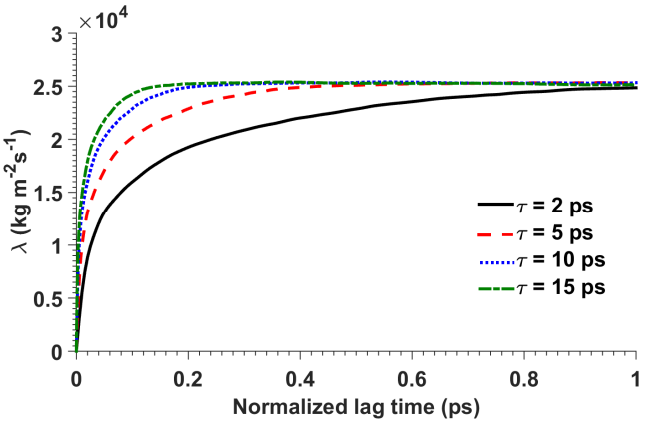

Figure 5.4: Calculation of the friction coefficient λ using the theory by Huang and Szlufarska [168].

The implementation of the Huang and Szlufarska's theory [168] for the calculation of $\lambda = \lambda(0)$ (Equations (3.15)) is depicted in Figure 5.4. The effect of using different lag times for the evaluation the TCF in Equation (3.15) is depicted in Fig 4. Smooth running integrals of λ are observed for different lag times; additionally, all of the curves saturate at the same plateau, making possible a reliable calculation of λ in equilibrium. From this, it can be inferred that one of the reasons for which the model developed in [168] leads to smother calculations than Equation (3.10), is that the sum of several individual TCFs of the solid-liquid interaction forces are considered in the calculation of λ, in addition to the fact that Equation (3.10) is based on the lumped sum of forces for a given number of solid particles. For statistical purposes, Equation (3.15) presents a better alternative than Equation (3.10) and also offers the possibility of applications involving heterogeneous systems, since the analysis is performed on the liquid particles. It is also important to note that a negligible effect is observed from using the biased or unbiased algorithms for the evaluation of the TCFs.

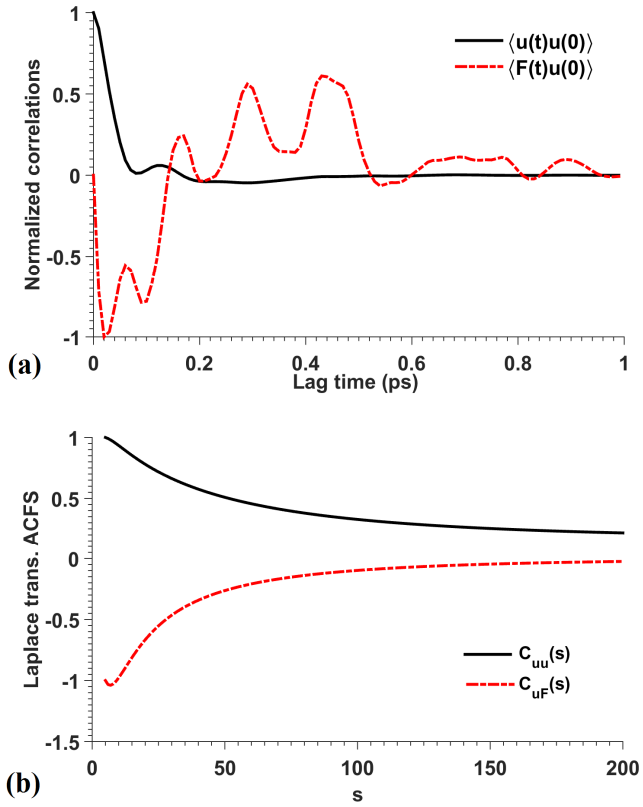

Figure 5.5: Implementation of Hansen et al. [166] method for calculating the liquid slab normalized (a) time correlation function and (b) the Laplace-transformed correlation functions.

Finally, the method used in the calculation of λ reported by Hansen et al. [166] was evaluated. The biased algorithm was used to evaluate the TCFs depicted in Equation (3.13) for different lag times. It was observed that while the velocity autocorrelation function always featured a relatively smooth behavior, the force-velocity cross correlation was considerably noisier. The best illustration of this is depicted in Figure 5.5(a) for a rather short lag time of 1 ps. The Laplace transform of the TCFs shown in Figure 5.5(a) is depicted in Figure 5.5(b). As illustrated, the noisiness is reduced in the Laplace space; however, the fitting process suggested in Equation (3.13) conducts to obtain slab-size and lag-time-dependent values of λ. Therefore, due to its high complexity, high computational demand, and sensitivity of L_s to the definition of the

interfacial region, the equilibrium model reported by Hansen et al. [166] was not utilized to calculate the value of L_s in this investigation.

5.1.2 Calculation of the hydrodynamic slip length using equilibrium theories

Data was collected from six independent simulations for each nanochannel size, H = 3, 5, and 8 nm. The time-dependent total force was recorded for the top and bottom walls for the calculations involving Equations (3.10-3.12), while the force acting on each liquid particle, its coordinates, and velocities were recorded for utilization in Equation (3.15). According to Bocquet and Barrat [131, 167], the hydrodynamic slip length is given by $L_s = \eta/\lambda$, where $\eta = 0.792\times10^{-3}$ Pa-s is the shear viscosity of SPC/E water [159] and λ is obtained from Equation (3.10). Twelve different lag-time-dependent curves of λ were averaged (six independent runs times two confining walls) for each nanochannel and then L_s was recorded in Figure 5.6. Two aspects can be highlighted from this first set of results: 1) the steady-state value at the plateau of the λ-curves notably varied between independent simulations as it can be observed in Figure 5.6 for the Bocquet and Barrat [131, 167] group of curves. The error bars at the end of each curve represent the standard deviation of the value of L_s and each curve is the average of twelve different curves. 2) It was consistently observed that the L_s curve for H = 3 nm was always the lowest, indicating a trend towards a smaller value of L_s for a highly confined channel. As for the identification of L_s as a surface property, the large margin of error of the calculations using the Bocquet and Barrat [131, 167] theory makes this assessment difficult. It is possible to identify a large region where L_s could be defined as a surface property; however, the consistent observation of L_s being the lowest for the nanochannel with H = 3 nm calls for further analysis.

The reinterpretation suggested by Petravic and Harrowell [165] to the theory proposed in [131, 167] was implemented by applying Equation (3.11) and $L_s = 0.5(H-\eta/\lambda)$. Evidently, Equation (3.11) is the same as Equation (3.10) as $t \rightarrow \infty$, but this

implementation is not possible, due to the increase noisiness of the TCFs as $t \rightarrow \infty$; therefore, the λ-curves previously obtained were used for the calculation of L_s as indicated in $L_s = 0.5(H - \eta/\lambda)$. Six independent simulations were averaged and the resulting L_s-curves are depicted in Figure 5.6 where the error bars indicate the standard deviation of L_s at the plateau. Since these new calculations of Ls depend upon the λ values previously obtained, the large error bars previously observed for H = 5 nm are still present. Two aspects can be highlighted about the implementation of the Petravic and Harrowell [165] model: 1) the values of L_s for the different nanochannels decreased by approximately a factor of two compared with the predictions using Equation (3.10) and $L_s = \eta/\lambda$, this was also observed in [165]; 2) the implementation of $L_s = 0.5(H - \eta/\lambda)$ seems to verify L_s as a surface property for the two smallest nanochannels; however, the large error bars observed for H = 5 nm again hinder any definite claim about the nature of L_s.

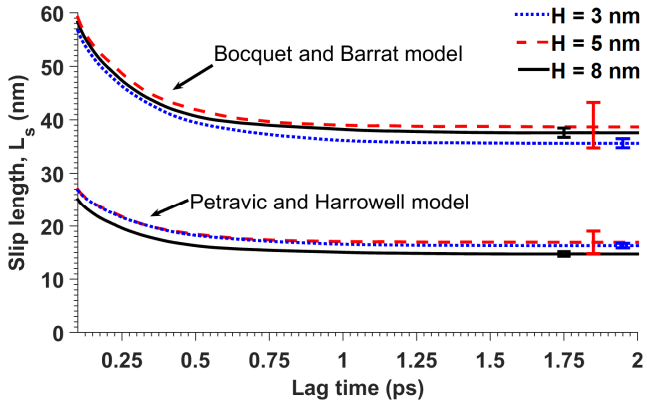

Figure 5.6: Calculation of the hydrodynamic slip length using the Bocquet and Barrat's theory and the reinterpretation of this theory by Petravic and Harrowell.

Huang and Szlufarska [168] indicated that due to the short-range nature of the interaction between the solid walls and the liquid particles, Equation (3.15) can be applied to an interfacial region near the solid walls or to the whole liquid domain; however, the authors of [168] did not indicate that in order to apply Equation (3.15) to the total number of liquid particles confined within the walls of a nanochannel, a

normalization by 2*A* is necessary. This was confirmed by means of evaluating Equation (3.15) in particles confined within interfacial regions near a solid wall. The extent of the interfacial space was increased until reaching half of the domain, where λ matched the value obtained from evaluating the total number of liquid particles using Equation (3.15) normalized by 2*A*. In order to avoid errors associated with the correct definition of the interface, all of the liquid particles within the confinement were included in the calculation of λ and the corresponding lag-time-dependent calculations of L_s are illustrated in Figure 5.7. A remarkable difference between the consistency of the calculations of L_s using Huang and Szlufarska's [168] theory can be observed when compared with the previous two analyzed theories. The L_s-curves depicted in Figure 5.7 are the result of averaging six independent simulations for each nanochannel size and as it can be observed the magnitude of the larger error bars is ~1 nm. More importantly, the consistency of these calculations allows observing that the theory by Huang and Szlufarska [168] indicates that L_s is a size-independet when the channel size is $H \geq 5$ nm. In addition, the accuracy of these calculations allows to verify that the smallest nanochannel features the smallest value of L_s. Another aspect to highlight is that the magnitude of L_s calculated by Huang and Szlufarska [168] lies between the previously analyzed theories.

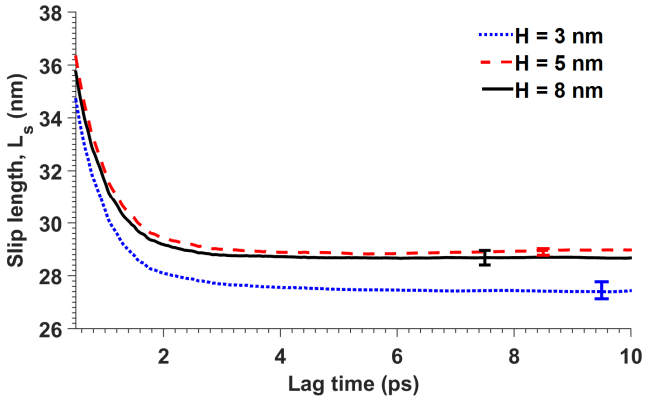

Figure 5.7: Calculation of the hydrodynamic slip length using the Huang and Szlufarska's [168] theory.

Irrespective of the different formulations leading to obtain the theories reported in [131, 165, 167] and [168], and disregarding the fact that the calculations of L_s differ in magnitude using these models, both indicate that L_s for the nanochannel with H = 3 nm is smaller than that for the larger channels considered. Further analysis was conducted in an effort to clarify the reason for this observation. For a model to predict L_s as a surface property, it must quantify the short-range nature of the solid-liquid force interactions at the interface. These interactions originate from a number of interfacial liquid particles; thus, the reason for the verification of the interfacial liquid structure at the beginning of Section 5.1. However, not only a time-averaged fixed concentration of interfacial liquid particles must be observed, but also the presence of the "same" particles, namely, mobility is important as well. If the range of mobility of liquid particles within a nanochannel is such that some particle can move from the bulk to the interfaces, the contribution to the forces reported on these liquid particles and the corresponding effect on the solid atoms due to proximity, observed in Equations (3.10) and (3.15), are reflected in the force TCFs and hence in the L_s calculation from λ.

The trajectory of individual water molecules was tracked over the entire simulation time in the different nanochannels. The time-average and standard deviation of the trajectory of each molecule was analyzed in order to observe the mobility of the particles. The upper panels of Figure 5.8 represent the information obtained for the smallest nanochannel. The scatter plot indicates that many of the bulk particles have a large mobility within the 3 nm nanochannel and the histogram of the mean position indicates that a large number of water molecules tend to remain in the bulk. The density profiles depicted in Figure 5.2(a) demonstrate that when averaged over time in fixed regions, the interfacial concentration of liquid particles is the same for each nanochannel, the histogram of the average position of the particles indicate that most of them tend to remain at the center of the channel, and the scatter plot illustrates that the bulk particles have a large mobility. Hence, a number of particles can travel from the bulk to the

interface and back contributing to the force TCFs observed in Equations (3.10) and (3.15) increasing the value of λ and hence reducing the expected L_s.

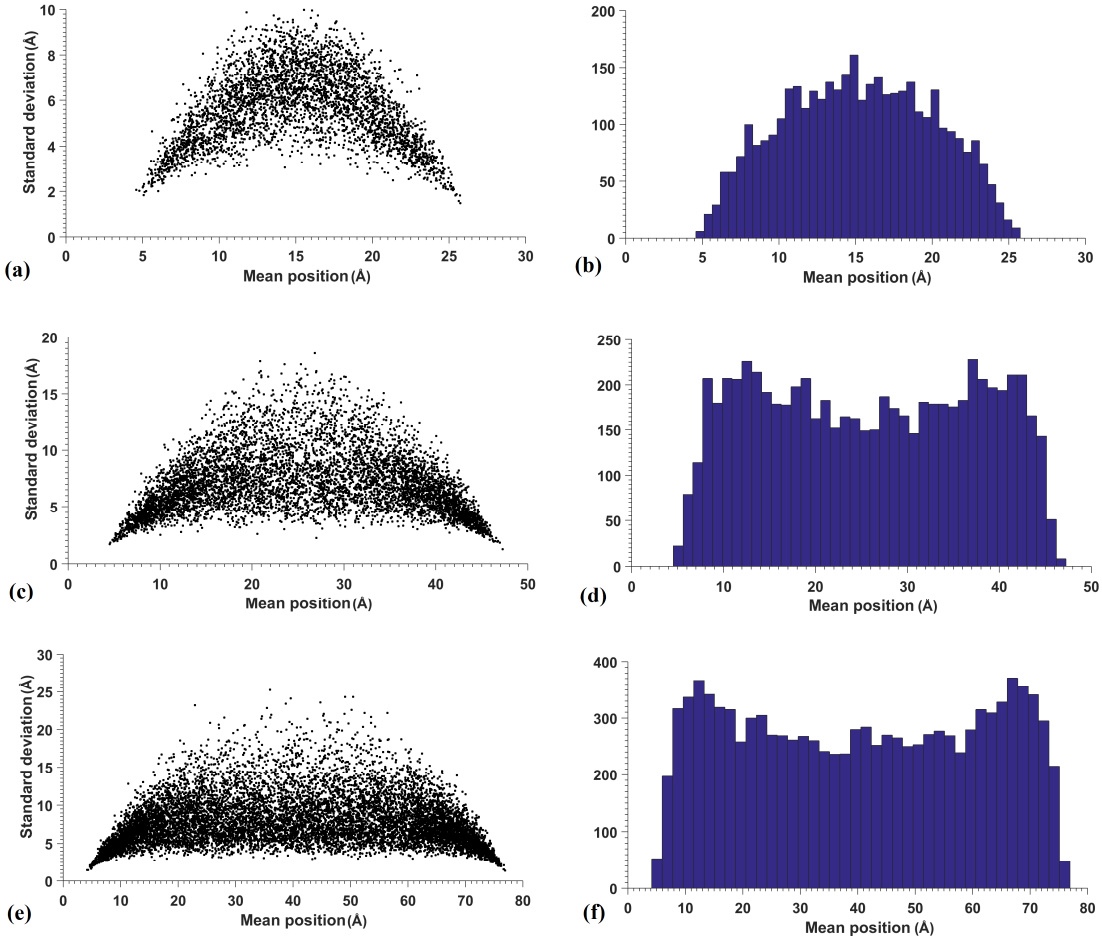

Figure 5.8: Statistical analysis of the displacement of the liquid molecules confined in nanochannels: H = 3 nm, upper panels (a) and (b); H = 5 nm, middle panels (c) and (d); and H = 8 nm, (e) and (f). The right panels are histograms of the time-average position of the liquid particles and the left panels are plots of the average versus standard deviation position of the liquid particles in the confinement.

Alternatively, the middle and bottom panels of Figure 5.8 clearly depict two population peaks of liquid particles near the solid walls in the histograms of the average position of individual particles. Likewise, the scatter plots illustrate a large concentration of particles near the wall where the mobility of liquid particles is limited by the strong solid-liquid interaction. Contrary to what was observed in the 3 nm channel, the number

of bulk liquid particles with the sufficient mobility to travel from the bulk to the interfaces is dramatically reduced in the 5 and 8 nm channels; thus, explaining the consistency between the L_s calculations observed in Figure 5.7.

5.1.3 Comparison between equilibrium and non-equilibrium calculations of hydrodynamic slip

Poiseuille and Couette flows were simulated in nanochannels of different sizes with H = 3, 5, and 8 nm. Shear flow was induced by moving the upper wall at a constant velocity while the bottom wall remained unaltered. Poiseuille flow was generated by means of exerting a variety of force magnitudes on the liquid particles ranging from 1×10^{-7} to 1×10^{-6} eV/Å. Since different channel sizes and flow types were used to obtain L_s from NEMD simulations, and in order to verify the low shear rate limit consistency with EMD simulations, L_s was recorded as a function of the shear rate. Figure 5.9 depicts the results obtained from the NEMD simulations, where the symbols represent the average of a number of independent simulations, in terms of L_s and shear rate, and the error bars are the range of variation observed for each set of simulations. The symbols represent the average between independent simulations for channels of all sizes, although it must be indicated that for shear rates $\leq 4\times1011$ s^{-1}, the results for H = 3 nm were very noisy. The following can be summarized from these modelling efforts: (a) consistent with the trends reported in [39] for nanoconfined flows with a deficient thermal energy removal through the channels walls, L_s decreased as the shear rate increased; this is due to the increased number of liquid particle collisions with the solid walls due to overheating; (b) size effects were difficult to observe due to the nosiness generated in the NEMD calculations of L_s for the smallest nanochannel, although the simulation results for the larger channels were very consistent; and (c) it can be observed that Huang and Szlufarska's theory was the best fit to the NEMD calculations of Ls in the low shear rate

limit. Hence, this equilibrium approach is highly encouraged as an alternative to time-consuming NEMD simulations.

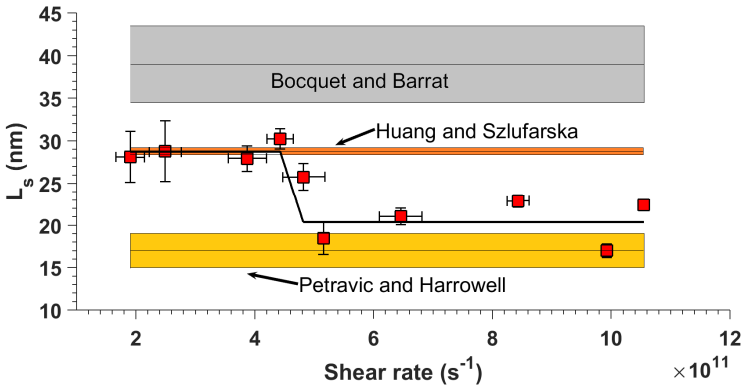

Figure 5.9: Comparison between non-equilibrium (solid symbols) and equilibrium (shaded regions) calculations of L_s.

5.2 Hydrodynamic slip and its relationship with wettability and the interfacial liquid structure

In the previous Section, a critical assessment of the conventional theories used to calculate the hydrodynamic slip was conducted. Additionally, the size-dependence of the hydrodynamic slip length was investigated in order to determine if this parameter is a surface property. The results indicated that, if compressibility effects are eliminated, the calculations of L_s derived from equilibrium calculations are affected by confinement sizes as small as 3 nm. The confinement effects were explained in terms of the mobility of the liquid particles and it was found that in order to obtain size-independent calculations of the slip length, L_s, the size of the confinement must be large enough to avoid a major concentration of liquid particles in the bulk, as well as a significnat migration from interfacial particles to the bulk. Based on these findings, the equilibrium theory by Huang and Szlufarzka [168] was used to calculate L_s in silicon and graphene-coated silicon nanochannels; likewise, NEMD simulations of Poiseuille flow were used to corroborate the equilibrium calculations. The wettability of the Si(111) and Si(100) planes and the

conditions required to observe wettability transparency were reported in Chapter 4. The same solid-liquid interactions were applied herein to address the wettability effect on L_s. The nanochannels used for this investigation are depicted in Figure 5.10. The confinement size was 5 nm, i.e., the distance between the innermost silicon atomic planes in the z-direction and the area was 5.76×5.98 nm for the Si(111) and 5.97×5.97 nm for the Si(100) nanochannels. The graphene coating was performed as indicated in Chapter 4.

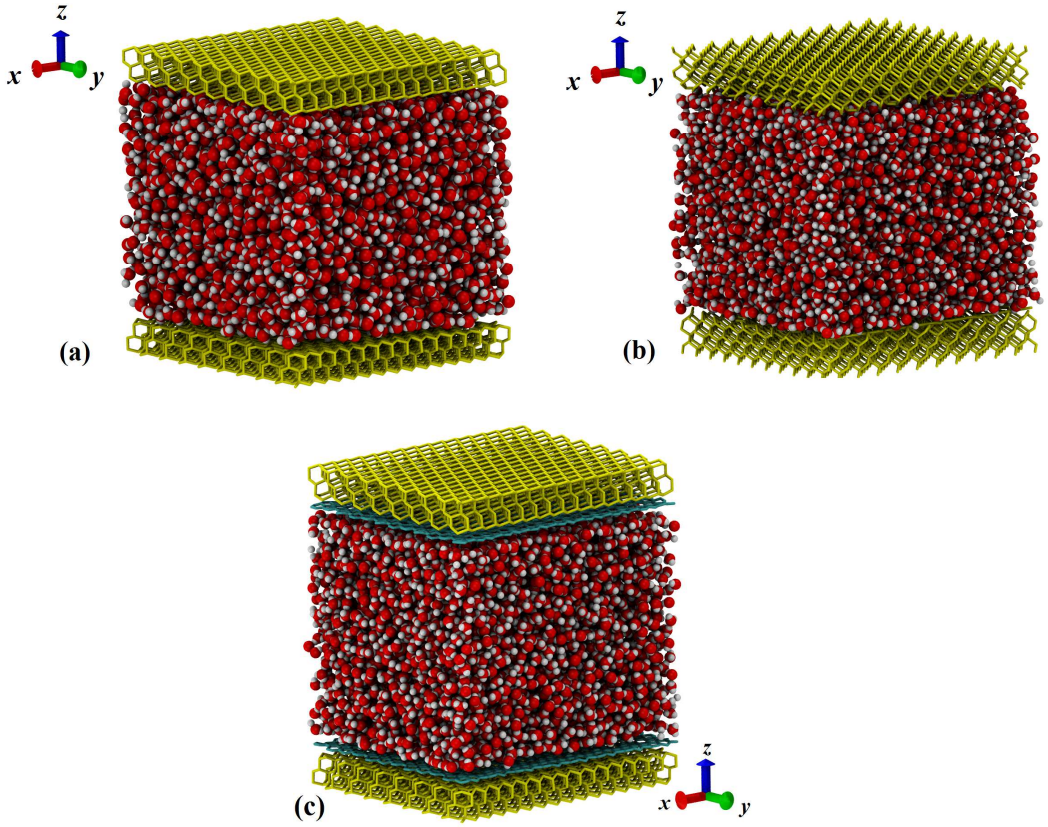

Figure 5.10: Water confined within (a) Si(111), (b) Si(100), and (c) graphene-coated silicon nanochannels.

5.2.1 Revisiting the wettability of silicon surfaces and the wettability transparency of graphene-coated silicon

The wettability of different silicon planes was characterized in Chapter 4 by the static contact angle calculated from the equilibrium geometry of cylindrical droplets. In

Chapter 4, the wettability of these surfaces was explained in terms of the interfacial liquid structure and the solid surface properties by means of the BCM. Here, the contact angles obtained are reported in Figure 5.11 as a function of the energy potential parameter, ε_{SiO}, which was used to artificially modify the wettability of the two silicon planes considered. Linear fits are depicted in each plot representing the scaling laws $\varepsilon \sim 1+\cos(\theta)$ and $\varepsilon \sim 180° - \theta$ proposed by Sendner et al. [46], in Figure 5.11(a) and 5.11(b), respectively. As shown, the points corresponding to each silicon plane fit both of the scaling laws, but at the same time and as indicated in [46], it is difficult to discriminate which one is the most physically sound scaling law due to the accurate matches observed. Additionally, it is noteworthy that there is difficulty in sampling the hydrophobic region (small ε_{SiO}) where $\varepsilon \sim 1+\cos(\theta)$ loses accuracy; namely, a purely repulsive wall exists at a finite value of ε_{SiO}. It is important to note that these scaling laws are not universal, as the linear fittings are different for each silicon wetted plane. It can be formulated that the anisotropy of the silicon crystal (atomic planar density and atomic interlayer distance) has a significant effect on the wettability of this material; this topic will be revisited in Chapter 6.

Figures 5.11(a) and 5.11(b) clearly indicate that although the silicon atoms and water molecules interact through the same energy potential, Si(100) is consistently more hydrophobic than Si(111). This can be explained by the different planar atomic densities for these two planes. The Si(111) plane is denser, hence, the interaction force per unit area is larger than that for the low density Si(100) surface. In addition that the underlying Si(111) structure is more closely packed due to its characteristic atomic triple bilayer periodic structure. These results were exhaustively analyzed in Chapter 4, where the BCM was used to describe the contact angles obtained from MD simulations. Theory and simulations matched and confirmed the intricate relationship among the interfacial liquid density, solid atomic planar density, and underlying solid structure anisotropy with the contact angle. The scaling laws presented here are simple approximations, but must be

considered as they constitute the origin of the slip-wettability scaling laws that will be discussed shortly.

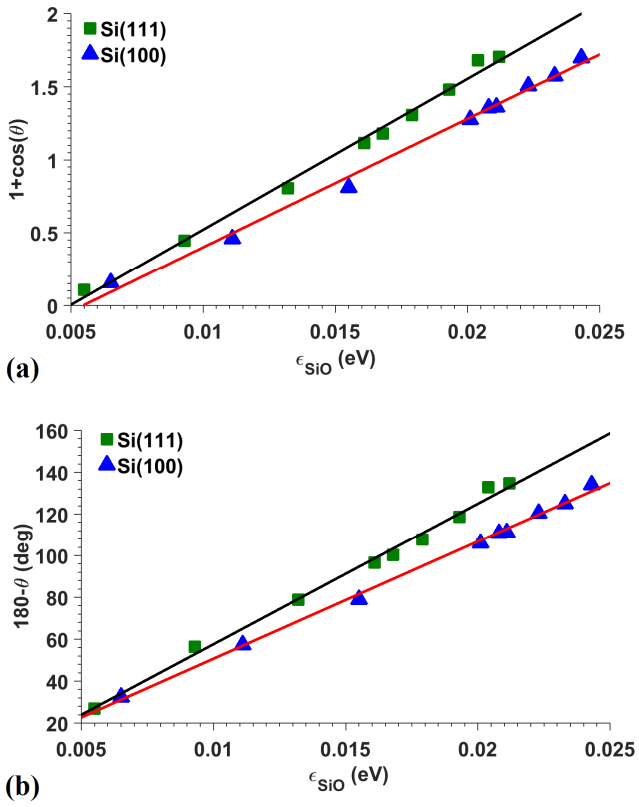

Figure 5.11: Wettability of different silicon planes expressed and the scaling laws correlating (a) ε ~ 1+cos(θ) and (b) ε ~ 180–θ.

In Chapter 4, the wettability of pristine (θ_S) and graphene-coated (θ_{GS}) silicon surfaces was theoretically and numerically investigated in order to determine the macroscopic conditions, substrate contact angle θ_S, required to observe wettability transparency for graphene-coated silicon. In this Section, the previous analysis was extended in order to obtain the conditions required to observe wettability transparency in graphene-coated silicon surfaces when the equilibrium separation between graphene and silicon is δ_{GS} = 2 Å, a more realistic equilibrium configuration of graphene supported on silicon as reported in [90-92]. The results illustrated in Figure 5.12, indicate that the BCM is sufficiently accurate to predict the wettability of graphene-coated silicon. Two

different values of δ_{GS} were considered and the numerical and theoretical prediction report a good match. δ_{GS} = 2 Å was enforced by defining the non-bonded Si-C interaction potential parameters as σ_{SiC} = 2.1 Å while ε_{SiC} was varied in a wide range. The results indicated no noticeable differences in the L_s calculations.

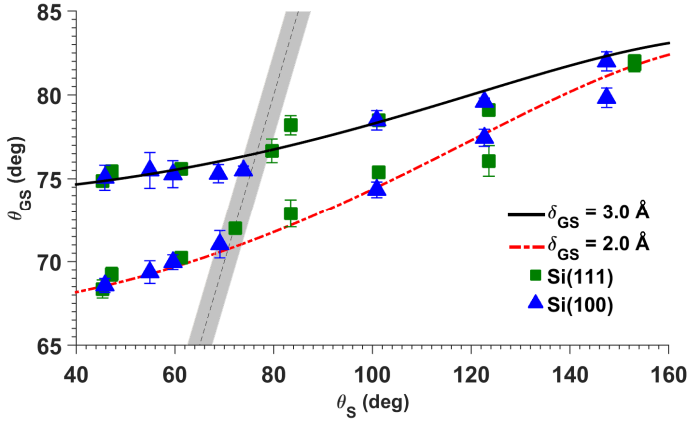

Figure 5.12: Wettability of pristine and graphene-coated silicon surfaces. The MD simulations results (symbols) verify the theoretical predictions (solid lines) of the wettability of graphene-coated silicon. Two different values for the equilibrium distance between graphene and silicon (δ_{GS}) were used for validation. The shaded region represents the wettability transparency condition with a ±2.5° deviation from $\theta_S = \theta_{GS}$.

The wettability of the nanochannels walls was varied as indicated in the previous section; hence, producing a change in the minimum pressure, P_0, required to push a liquid into a slit-like pore of width H as indicated in [42]. In order to achieve similar bulk properties for confinements with different wettability, the number of liquid particles within the confinement was adjusted (pressure is proportional to the number of particles at constant volume). The number of water molecules confined within 5 nm was varied as 5776–5668 to cover the range from hydrophilic to hydrophobic conditions, in that order. Figure 5.13 depicts the density profiles along the nanochannels height (z-direction) for two wettability conditions of the walls, Figure 5.13(a) hydrophilic and Fig. 5.13(b) hydrophobic, for both silicon structures. Similar bulk densities are observed in each case as well as a stronger liquid layering for hydrophilic surfaces and a weak layering for

hydrophobic surfaces, a typical characteristic. It is also noticeable that the Si(100) surface features a larger liquid density depletion, and this is due to the low atomic density of the Si(100) plane. A major goal of this investigation was to ensure that similar bulk properties were observed in every system while the wettability of the nanochannels varied. This is an important issue since the hydrodynamic slip is an interfacial phenomenon.

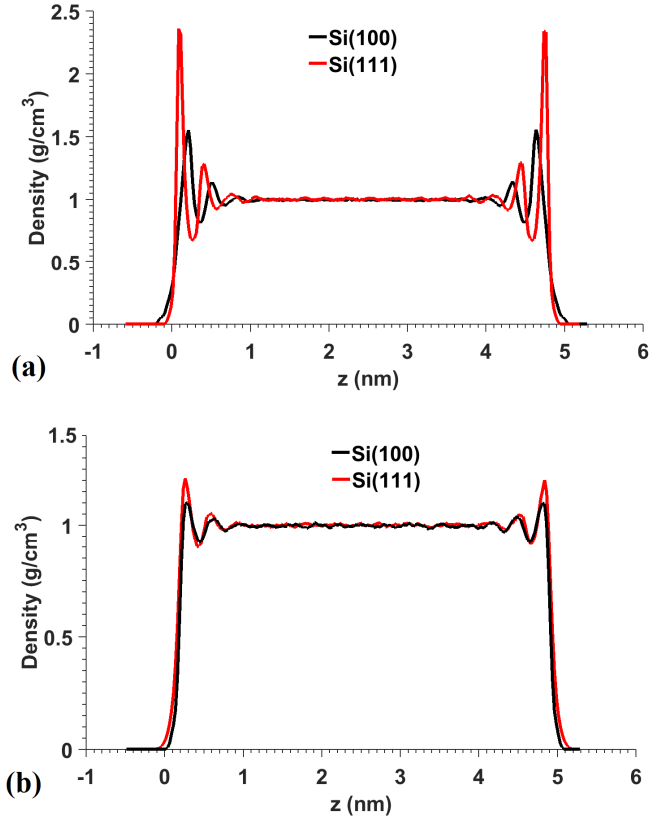

Figure 5.13: Density profiles along the nanochannels height with contact angles of (a) θ = 71° and (b) θ =150°.

5.2.2 Hydrodynamic slip and wettability

The first objective of this investigation was to verify the quasiuniversal relation between wettability and hydrodynamic slippage proposed by Sendner et al. [46]. Figure 5.14 illustrates L_s as a function θ, both obtained from EMD simulations for Si(111),

Si(100), and graphene-coated silicon nanochannels. It was observed that for $\theta < 100°$, L_s is practically zero for both silicon surfaces and therefore is similar. However, for $\theta > 100°$, noticeable differences begin to arise. L_s is consistently greater in Si(111) than in Si(100) nanochannels. This is understandable, since the Si(111) plane offers a smoother surface to the liquid particles than the rougher (lower planar atomic density) Si(100). The roughness effect at the nanoscale is essentially a corrugation of the solid-liquid interaction potential. Figure 5.14 depicts the two scaling laws reported in [46] to correlate L_s and θ. The scaling laws were obtained from a scale analysis performed on the equilibrium theory of Bocquet and Barrat [131], where $L_s \sim \varepsilon^{-2}$, and the observation of the wettability scaling laws reported in Figure 5.11. The fitted curves were obtained by a non-linear least squares algorithm using as input data for both silicon nanochannels. When the wettability transparency of graphene-coated silicon nanochannels is examined (both silicon surfaces have a contact angle of ~71° for δ_{GS} = 2.0 Å), a significant departure from the slip-wettability scaling laws is observed in Figure 5.14. These results suggest that the scaling laws that use the contact angle as a quasiuniversal parameter are not as robust as previously thought.

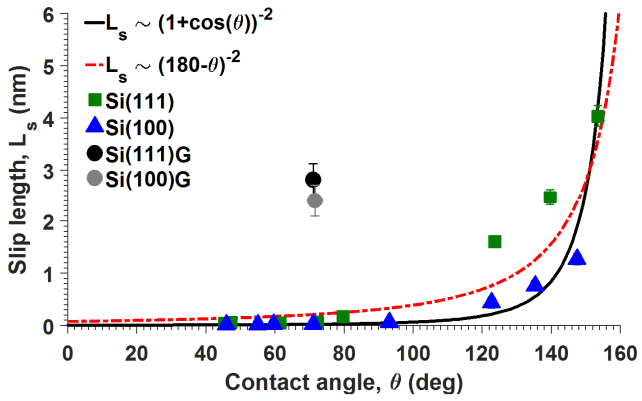

Figure 5.14: Relationship between hydrodynamic slip and wettability for silicon nanochannels having different wettability and graphene-coated silicon nanochannels under wettability transparency conditions.

NEMD simulations of Poiseuille flow were conducted for the silicon nanochannels under different wettability conditions and for the graphene-coated silicon nanochannels under wettability transparency. Unlike EMD, NEMD simulations are strongly affected by the noisiness of the calculations of the velocity profiles (statistical noise due to binning) in a single simulation and variations obtained between independent simulations. The velocity profiles obtained via NEMD are depicted in Figure 5.15 for Si(111) and Si(100) nanochannels under hydrophilic and hydrophobic conditions. Forces varying between 1×10^{-5} eV/Å and 8×10^{-5} eV/Å were applied to each water molecule for the hydrophilic and hydrophobic cases in order to identify the low shear rate limit for a proper comparison between NEMD and EMD simulations. Figures 5.15(a) and 5.15(b) depict a consistency with EMD calculations, i.e., no-slip, for Si(111) and Si(100) nanochannels for the given hydrophilic condition. For hydrophobic Si(100) nanochannels $L_s = 0.9 \pm 0.24$ nm was obtained from NEMD, a value consistent with the average 1.28 nm obtained from EMD . Alternatively, the hydrophobic Si(111) nanochannel featured a more noticeable discrepancy between methods for calculating slip. In the limit of low shear rate, $L_s = 2.1 \pm 0.83$ nm was calculated for hydrophobic Si(111). The larger margin of error arises from the noisiness of the calculations when the gradients imposed are too small, which was necessary for this nanochannel. A factor of two is observed in the difference between the NEMD and EMD calculations for this particular condition. Discrepancies between EMD and NEMD simulations of hydrodynamic slippage have been previously reported [52, 168, 177] as there is still a lack of consensus on the accuracy of the equilibrium theories for the calculation of hydrodynamic slip as indicated in Section 5.1.

Figure 5.16 illustrates a comparison between velocity profiles obtained for bare silicon and graphene-coated silicon nanochannels. The wettability conditions for both surfaces are the same, however, significant differences are observed regarding the hydrodynamic boundary conditions. The bare silicon nanochannels under the hydrophilic

condition of θ = 71° exhibits no-slip while the graphene-coated version of these nanochannels clearly shows a slip boundary condition. As it can be observed, these results are consistent with the EMD calculations reported in Figure 5.14.

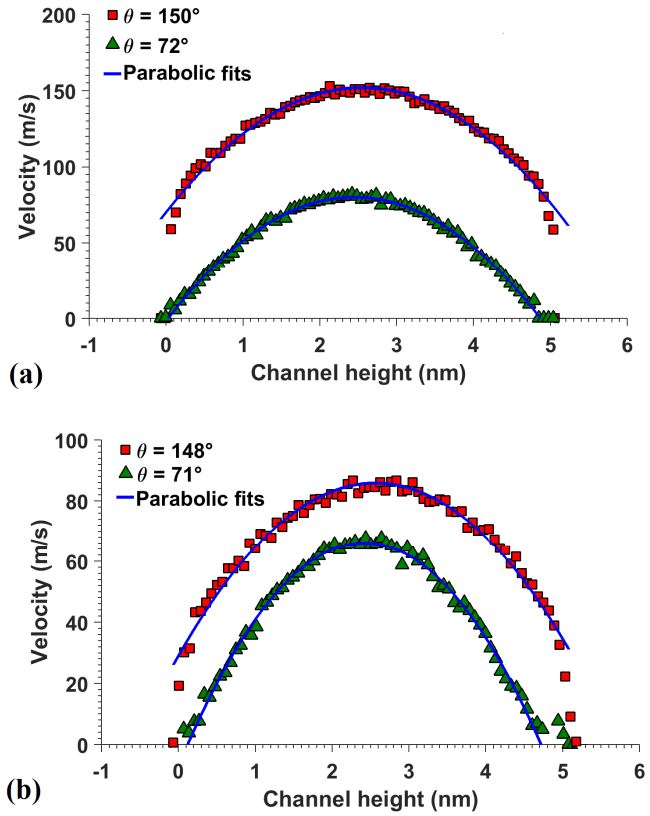

Figure 5.15: Velocity profiles obtained for (a) Si(100) nanochannels and (b) Si(111) nanochannels.

Recently, Li et al. [53] experimentally investigated the flow dynamics in a silicon nanochannels array, where each nanochannel had a cross-section of 100 nm by 100 μm. By varying the flow rate and recording the pressure drop of the array, the shear rate was determined from an analytical model taking into account hydrodynamic slip. From the data fitting, it was observed that there was no slip until a shear rate of 1×10^{5} s^{-1} was reached. This experimental observation is consistent with the calculations presented here for silicon nanochannels using EMD and NEMD calculations at low shear rate conditions. The wettability of pristine silicon is difficult to measure, but recent

experiments have determined that the contact angle for water on silicon is ~77° [174], a value included in the range of hydrophilic conditions investigated herein. Thus, by calibrating the silicon-water interaction potential to a contact angle of ~72°, it was possible to obtain the no-slip boundary condition at low shear rates (consistency between EMD and NEMD calculations) as reported from experiments.

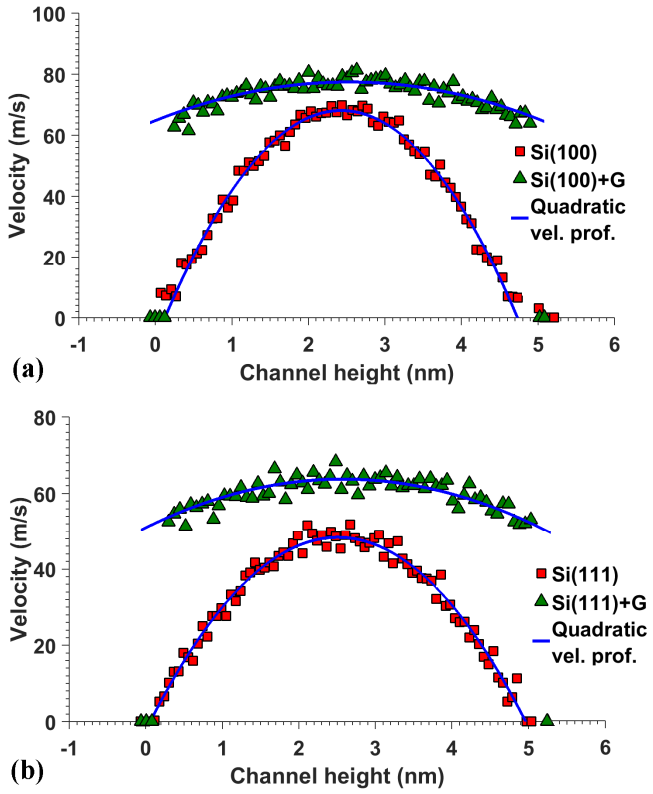

Figure 5.16: Velocity profiles obtained for (a) graphene-coated Si(100) nanochannels and (b) graphene-coated Si(111) nanochannels under wettability transparency conditions.

5.2.3 Hydrodynamic slip and the interfacial liquid structure

In addition to the quasiuniversal scaling laws of hydrodynamic slip, Huang et al. [45] observed the relationship $L_s \sim \delta^4$, which was derived from the observed dependence of δ on the solid-liquid interaction parameter ε and the scaling performed on the Bocquet and Barrat model, see Equation (3.10). Figure 5.17 illustrates L_s as a function of δ, obtained as

$$\delta = \int_0^{\infty} \left[1 - \frac{\rho_l(z)}{\rho_l^b} - \frac{\rho_s(z)}{\rho_s^b} \right] dz \tag{5.1}$$

where $\rho_s(z)$ and $\rho_l(z)$ are the solid and liquid densities along the z-direction (height) of the nanochannel, and ρ_s^b and ρ_l^b are the bulk solid and liquid densities. δ represents a measurement of the water depletion that exists due to the short-range repulsion between the solid and liquid atoms. It is clearly observed that the scaling law $L_s \sim \delta^4$ features a better prediction of the nature of the boundary condition, regardless of the contact angle or the characteristics of the channels walls. Figure 5.17 indicates that L_s is different between hydrophobic silicon nanochannels (θ > 100°) because the depletion length is more prominent in Si(111) than in Si(100) surfaces. Additionally, the reason that the graphene-coated slip is similar to the hydrophobic Si(111) can be explained by recognizing that both surfaces exhibit similar δ values. Thus, Figure 5.17 helps to reconcile the results reported in Figure 5.16 for the three different types of nanochannels and remark the strong correlation between Ls and δ.

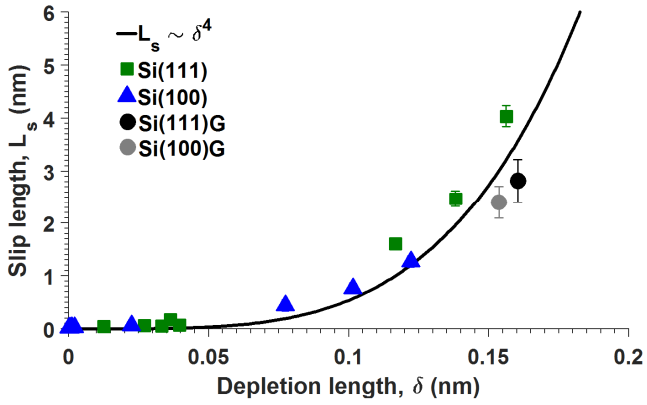

Figure 5.17: Reconciliation of the hydrodynamic slip length calculations in silicon nanochannels having different contact angles and graphene-coated silicon nanochannels.

Figure 5.18 illustrates the calculation of δ from the water density profiles within the confinement for Si(111), Si(100), and graphene-coated silicon nanochannels under wettability transparency conditions. As indicated in Chapter 4, the interfacial liquid

structure of Si(111) is very similar to that of graphene-coated silicon if the density peaks are shifted to coincide, see Figure 5.18(a). When the density profiles are integrated using Equation 5.1, the density depletion length can be obtained from the plateau of the running integral as illustrated in Figure 5.18(b).

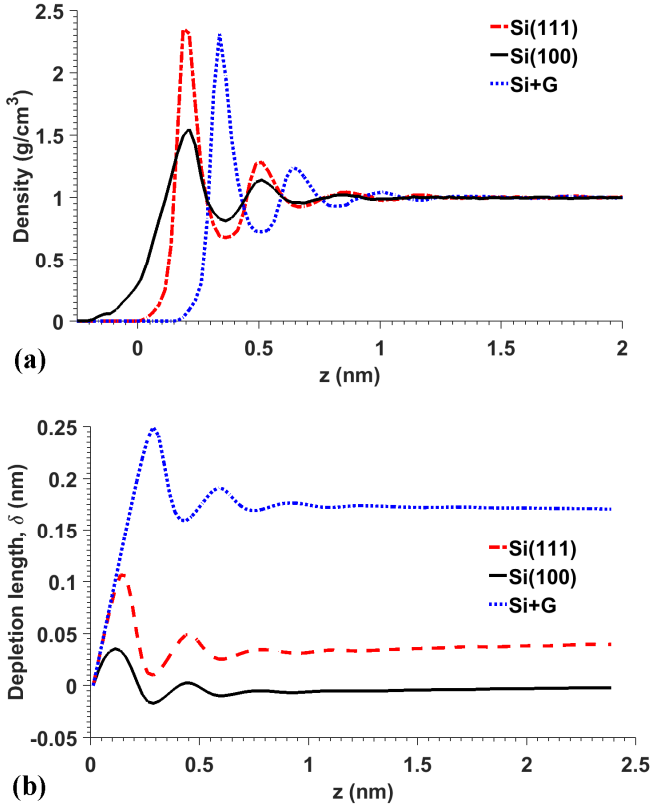

Figure 5.18: (a) Interfacial liquid water density profiles and (b) depletion length calculations.

During the derivation the slip-wettability quasiuniversal relationships, Huang et al. [45] and Sendner et al. [46] observed the scaling law $1+\cos(\theta) \sim \varepsilon$ after simplifying a mean-field-theory-based wettability model. This expression was fundamental in the development of the slip-wettability laws and is in fact correct, as has been previously demonstrated in Figure 5.11; however, this assumption is only applicable for specific situations. The robust wettability model based on the mean-field theory (the BCM), reported Section 4.1, indicates that the contact angle depends on the ε and σ parameters

of the non-bonded solid-liquid interaction potential, the interfacial liquid structure, the planar atomic density of the solid atoms, and the underlying structure of the wetted surface, i.e., the solid structure anisotropy also plays a role in nanoscale wettability. This functional dependence is coupled and no single effect can be isolated, with the exception of ε at some level. Therefore, the simplification made in [45] to obtain $1+\cos(\theta) \sim \varepsilon$ is valid only when the rest of the aforementioned variables are lumped into a single constant; hence, the quasiuniversal prefix of these laws is justified. Additionally, the process followed to obtain a given contact angle from MD simulations is one of calibration. The process consists of fixing one of the two non-bonded solid-liquid interaction parameters and varying the other until obtaining an objective contact angle for a given solid structure. This explains why the wettability of Si(100) is different than that of Si(111) when using the same silicon-water interaction potential, in addition that both planes feature different interfacial liquid structures when wetted due to the anisotropy of the silicon crystal.

The hydrodynamic slip phenomenon is one of interfacial nature. Thus, a better description of L_s can be obtained when the interfacial liquid structure is considered (δ). The density depletion length, δ, indicates that as the equilibrium separation between the solid and liquid atoms increases, hydrodynamic slippage is prone to occur due to the reduction of the momentum transfer between solid and liquid particles. For a non-bonded interaction, the equilibrium distance between a pair of atoms scales as $d_{eq} \sim \sigma$. Hence, the interfacial water depletion is directly affected while the calibration process for the calculation of the contact angle is merely adjusted. Likewise, the magnitude of σ affects the energy corrugation of the solid-liquid interaction potential, in combination with the atomic arrangement of the solid in contact with the liquid. In Figure 4.15, it was observed how the low atomic planar density Si(100) surface features a rough energy landscape with deep potential wells where liquid particles can be entrained. This explains the small values of δ, as illustrated in Figure 5.18(b). Alternatively, the Si(111) structure features a

smoother energy landscape, mainly due to the larger planar atomic density and the closely packed bilayer structure of this silicon plane. Finally, the closely packed structure of graphene in combination with a large value of the σ_{CO} parameter generates a flat energy landscape, above which the water molecules are only affected by the magnitude of the interaction strength and not the granularity of the underlying solid substrate. This smooth energy surface helps to explain the higher values of L_s under wettability transparency conditions.

The density contours of a liquid slab 1 Å thick, positioned at the first liquid layer, the highest density peak observed in Figure 5.13 for each nanochannel, were obtained to visualize the 2-D liquid structure under hydrophilic (θ = 72° for Si(111) and θ = 71° for Si(100)) nanochannels and the same conditions under wettability transparency in graphene-coated silicon nanochannels. Figure 5.19 illustrates the density contours under hydrophilic conditions for Si(111) and Si(100) nanochannels. Under the strong solid-liquid affinity conditions depicted in Figure 5.19(a), it is observed that the hexagon-like pattern of the Si(111) plane is imprinted onto the first atomic liquid layer. Likewise, the large interstitial spaces between the atoms of the Si(100) plane in the [111] direction form a potential well where liquid particles get trapped. As it can be observed, under strong solid-liquid affinity conditions, the granularity of the solid surfaces is imprinted on the interfacial water; thus, promoting a no-slip hydrodynamic condition. These observations add to the understanding of the no-slip boundary condition in Si(111) and Si(100) from an observation of the interfacial liquid structure normal to the walls, while the density depletion length provides information about the water structure in the normal direction to the walls. Interestingly, Ho et al. [44] indicated that interfacial structures like the ones depicted in Figure 5.19 represent density bridges, meaning that liquid particles can move throughout the interface causing slippage to occur. However, the results reported herein indicate that these connected interfacial structures represent a rather strong solid-liquid attraction that decreases or eliminates slip.

When the granular silicon surfaces are coated with graphene, see Figure 5.20, the interfacial liquid structure parallel to the walls surface is characterized by smooth density contours. Compared with the density contours of Figure 5.19, the granularity of the solid surface is no longer imprinted on the interfacial liquid structure. This indicates a less effective momentum transfer between the solid and liquid particles. Additionally, the uniform density contours observed in Figures 5.20(a) and 5.20(b) reveal the presence of a smooth barrier created by the closely packed structure of the carbon atoms in graphene, above which, the liquid particles are prone to slip due to the smoothness of the energy landscape. Lastly, these uniform density contours and the smooth energy barrier that leads to create them, help to explain the differences in the hydrodynamic slip observed between Si(100) and Si(111) for similar contact angles, i.e., in order to observe the same contact angle between these two different silicon surfaces, the Si(100)-water interaction potential is stronger than for Si(111) in order to compensate for the lower atomic planar density of the Si(100) surface; hence, L_s is smaller for Si(100).

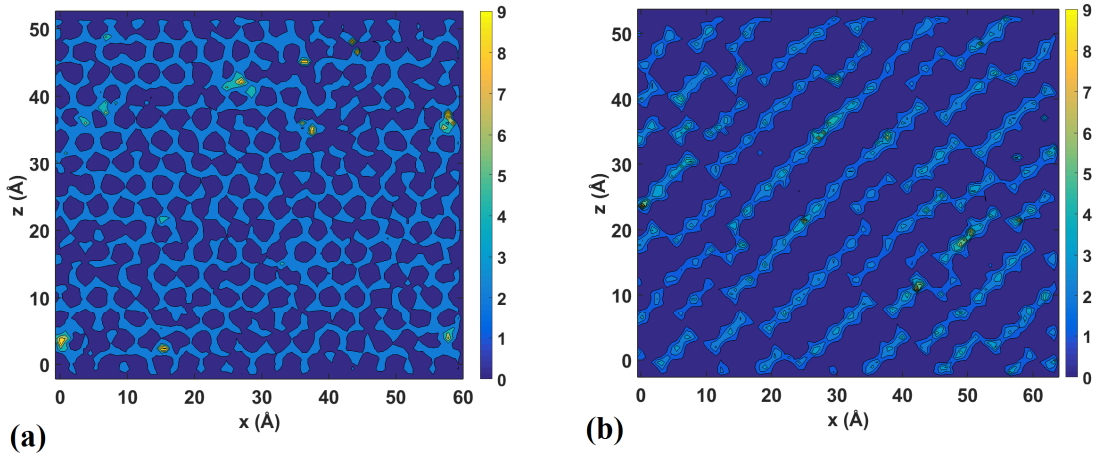

Figure 5.19: Interfacial density contours (g/cm^3) under hydrophilic conditions for (a) Si(111) and (b) Si(100) nanochannels.

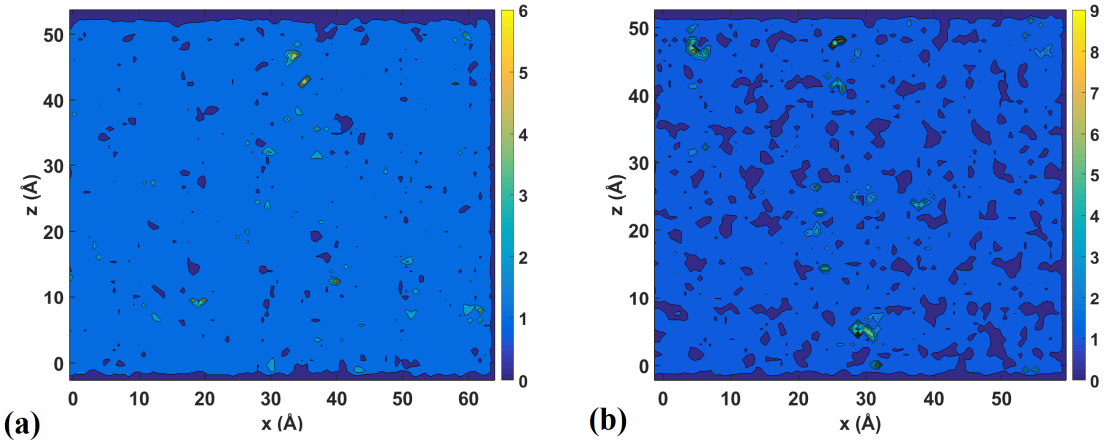

Figure 5.20: Interfacial density contours (g/cm^3) under wettability transparency conditions for (a) Si(111) and (b) Si(100) graphene-coated nanochannels.

5.3 Summary

The characterization of the silicon-water and carbon-water interactions performed in Chapter 4 was used as the foundation for the investigation of the relationship between hydrodynamic slip and wettability in this Chapter. As a first step, the most current theories used to calculate hydrodynamic slip from equilibrium simulations were critically evaluated and compared with the results obtained from non-equilibrium simulations of flow. In addition, the hypothesis that the hydrodynamic slip length is a surface property was evaluated after eliminating compressibility effects for a given wettability condition in different levels of confinement. It was obtained that the common slip theory by Bocquet and Barrat [131, 167] was hindered by noisy calculations of the friction coefficient caused by the evaluation of the time-correlation functions of the shear forces. The slip model that resulted in the most consistent calculations of slip was that reported in [168]. The calculations from this model were consistent with non-equilibrium simulation results in the low shear rate limit. It was consistently observed that the equilibrium models suffered from size-dependence if the confinement size was as small as 3 nm. An analysis of the trajectory of the liquid particles within the different

confinements indicated that the mobility of liquid particles was the major contributor to observe size effects. Thus, in order to obtain size-independent calculations of the hydrodynamic slip length, well defined particles concentration regions must be observed near the walls of the nanochannels. This is achieved if the size of the confinement is large enough to avoid particles to travel from one wall to the other.

The hydrodynamic slip-wettability dependence was investigated in silicon nanochannels having different wettability conditions, as reported in Chapter 4, and graphene-coated nanochannels under wettability transparency conditions. By doing this, two different systems with similar wettability were investigated. Unlike previous investigations where the wettability of the surfaces is artificially modified, the graphene-coated surfaces present a system that experimentally report similar contact angles as the bare silicon surfaces. The results indicated that the contact angle is not a universal parameter to correlate with the hydrodynamic slip length. A clear breakdown was found in the slip-wettability quasiuniversal relationships was found when slip was calculated in silicon channels with different atomic planar granularity, Si(100) and Si(111). A more drastic deviation from the slip-wettability quasiuniversal relationships was found for the graphene-coated silicon surfaces under wettability transparency conditions. The hydrodynamic boundary condition in hydrophilic silicon was that of no-slip, just as reported from recent experiments in silicon nanochannels. Thus, the numerical simulations conducted here after calibrating the solid-liquid interactions with experimental wettability data matched the experimental calculations of slip in silicon nanochannels. Alternatively, a graphene-coated nanochannel having the same wettability as the bare silicon presented a slip boundary condition. Lastly, it was found that the slip calculations for all kinds of nanochannels and wettability conditions were reconciled using the density depletion length as a parameter. The density depletion length characterizes the effectiveness of the momentum transfer between the solid and liquid phases and this parameter depends upon the solid-liquid affinity and the interfacial solid

structure. Thus, the density depletion length poses a better alternative than the contact angle to characterize the hydrodynamic boundary condition in nanoconfined liquids.

CHAPTER 6

THERMAL TRANSPORT IN NANOCONFINED WATER AND ITS WETTABILITY DEPENDENCE

Thermal transport across silicon and graphene-coated silicon surfaces in contact with water is reported in this Chapter. The wettability characterization of the different silicon surfaces reported in Chapter 4 was used in order to model the solid-liquid interactions in non-equilibrium molecular dynamics simulations (NEMD) of heat transfer. Likewise, the conditions required to observe wettability transparency were incorporated into these modeling efforts with the objective of assessing the effect of the contact angle on the solid-liquid thermal boundary conductance. An spectral analysis and a characterization of the interfacial liquid structure were carried out in order to explain the observed behavior of the interfacial thermal transport across solid-liquid interfaces having different surface roughness, observing liquid entrainment, and conducting to interface density depletion.

6.1 Thermal boundary conductance calculations

The thermal boundary conductance, *G*, across silicon-water and graphene-coated silicon-water interfaces was investigated using NEMD simulations as indicated in Section 3.5.1. A water block was confined between silicon and graphene-coated silicon slabs as depicted in Figure 6.1. The outermost silicon layers were kept fixed in order to constrain the system volume. Thermal energy was added and removed at the same rate from the silicon atoms enclosed in the extreme regions indicated in Figure 6.1, in such a way that a net heat flow was induced in the direction shown. The number of water molecules within the confinement was varied such that similar bulk density and pressure were observed, as indicated in Figure 5.2, for the different wettability conditions, as indicated in Figure

5.13. The observation of similar bulk properties is necessary so that compressibility effects can be discarded. The equilibrium distance between silicon and graphene was 2 Å [90-92] and the silicon-carbon interaction potential was that reported in Section 5.2.1.

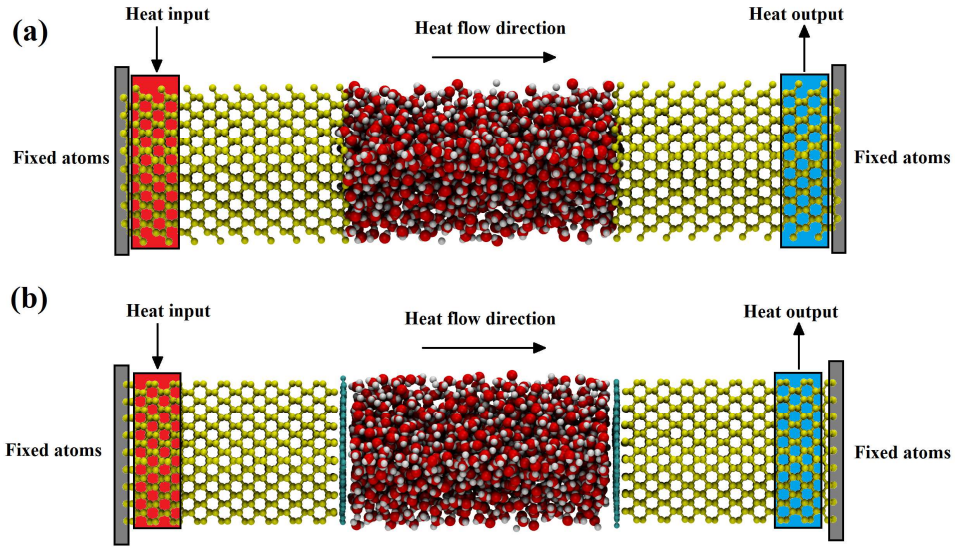

Figure 6.1: (a) silicon and (b) graphene-coated silicon systems used to investigate the thermal transport across bare surfaces with different wettability and under wettability transparency conditions.

After the system reached a quasiequilibrium condition, determined by tracking the temperature of the hot and cold baths, the average system temperature, and the conservation of energy, the temperature profiles were obtained using Equation (6.1)

$$T = \frac{1}{k_B}\frac{KE}{N_f/2} \tag{6.1}$$

where KE is the kinetic energy and N_f is the number of degrees of freedom. The silicon structure is organized in cubic diamond lattice with a well-defined number of atoms per atomic plane. The position of these atoms varies slightly as they only oscillate with respect to their lattice site. Therefore, the KE for the silicon atoms was calculated as the average per atomic layer for each slab and for these type of atoms $N_f = 3$. The calculation of the temperature profiles for the water slab was more elaborated. First, the slab was divided into bins and the number of water molecules was counted per time step and used

to average the total kinetic energy per bin. It is worth noting that the water molecules have 9 degree of freedom, but since the SPC/E water model is rigid, N_f = 6. This calculation gave the time-dependent temperature profile and many temperature profiles were averaged over time as indicated in Section 3.5.2. A sample of an equilibrium temperature profile is depicted in Figure 6.2. After obtaining the discrete temperature profile, indicated by symbols in Figure 6.2, linear fits were performed using a least-squares algorithm. For silicon, the non-linear regions consisting of the atoms receiving and giving away thermal energy, and also the first two atomic layers facing water were not considered for the linear fitting. As for water, the density layering and depletion observed at the interface (interfacial liquid structure), affected the local temperature calculation as illustrated in Figure 6.2. These regions were not included in the linear fitting. It was observed that hydrophobic surfaces did not present such a problem due to the negligible density layering observed for these surfaces. The temperature jump at the interface was calculated by extrapolating the silicon and water temperature profiles to the interface. From the many simulations conducted, it was possible to calculate the thermal conductivity of water at 300 K using Fourier's law as 0.827±0.083 W/m K, a value consistent with the thermal conductivity of SPC/E water 0.81 W/m K [158].

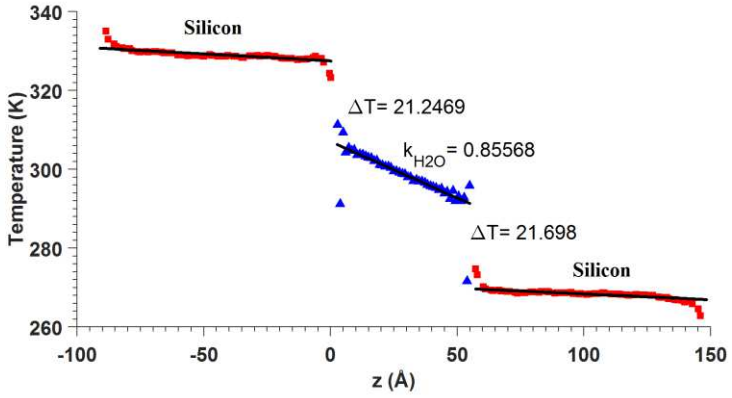

Figure 6.2: Temperature profiles obtained for hydrophilic silicon Si(111) and water with a heat flow of 20 nW.

Different heat fluxes were applied to the systems depicted in Figure 6.1 under different wettability conditions, and G was calculated using Equation (3.19) but not for individual simulations but as the slope of the line $J = G\Delta T_{int}$. Figure 6.3 depicts sample calculations of G for Si(100) and Si(111) under hydrophilic and hydrophobic conditions. From Figure 6.3 it can be observed that 1) the range of heat fluxes used are low enough to induce a linear response of the systems under investigation. Nanoscale systems are usually hindered by non-linear effects due to the significantly large temperature gradients generated in NEMD simulations and the large heat fluxes required to eliminate statistical noisiness in the calculation of the temperature profiles. 2) The linear fits performed extrapolate to $J = 0$ when $\Delta T_{int} = 0$ K, just as expected.

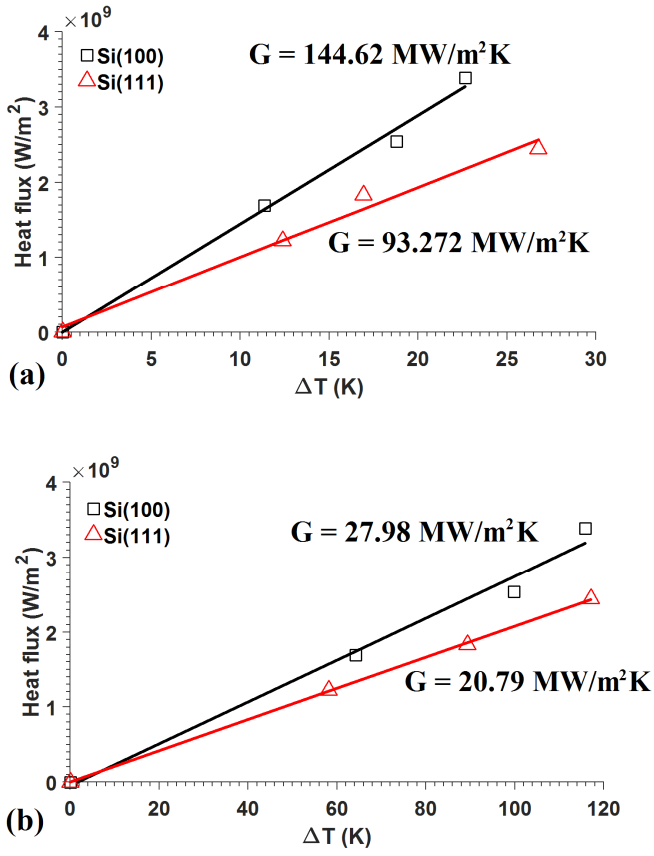

Figure 6.3: Thermal boundary conductance calculations for Si(100) and Si(111) under (a) hydrophilic and (b) hydrophobic wettability conditions.

The affordability of the nanoscale simulations of heat transfer is hindered by the size of the systems used for calculations. For example, different transport mechanisms are observed when the dimensions of the systems are smaller than the phonons mean free path. Therefore, an analysis of size effects was conducted prior to engaging in the objectives of this investigation. Originally, the silicon slab size was 5 nm and the water confinement 6 nm, the area of the Si(100) system was 2.7×2.2 nm and that of Si(111) was 3.1×2.7 nm. The different areas of the silicon structures were necessary in order to create a periodic structure matching the honeycomb structure of graphene, see Section 4.4. Figure 6.4 illustrates a summary of the assessment of the size effects on the calculations of *G* for the Si(100) system. First, a simulation where Si(100) had the same area as the Si(111) system was conducted and no significant changes were observed. Then, area was quadrupled and no change in the calculation of G was changes, as indicated in Figure 6.4. The most critical dimension was that in the heat flow direction. The original length was doubled and tripled and now drastic changes were observed. After further examination, it was concluded that a silicon slab of 10 nm was sufficient for performing reliable calculations of *G* at an affordable computational time.

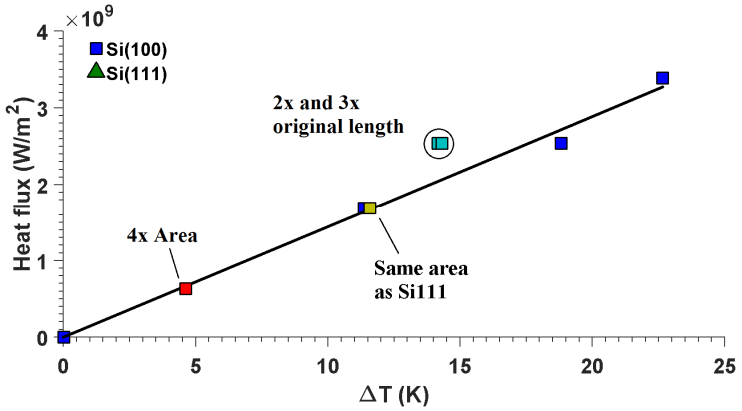

Figure 6.4: Analysis of the size effects on the calculation of the thermal boundary conductance.

The effects of the wall temperature on the calculation of G were previously discussed in Section 2.4.3. In summary, the concentration of phonons at the interfaces increases as the temperature increases. Thus, it is expected to obtain larger G values when the calculation is performed for the hot wall as indicated in Figure 6.2. The ratio G_{HOT}/G_{COLD} was calculated for every silicon system under a wide range of wettability conditions and the results are presented in Figure 6.5. It is consistently observed that $G_{HOT}/G_{COLD} > 1$ for both silicon surfaces, except for one single point, and no trends is observed as a function of the contact angle. Figure 6.5 also shows that G_{HOT}/G_{COLD} is smaller for the Si(100) system than for Si(111), this is due to the liquid interfacial structure effects and phonons density of states variations between both systems, this will be explained in Section 6.3. In general $G_{HOT}/G_{COLD} < 1.1$, thus the calculations of G presented in the following Sections are the average of the hot and cold wall calculations.

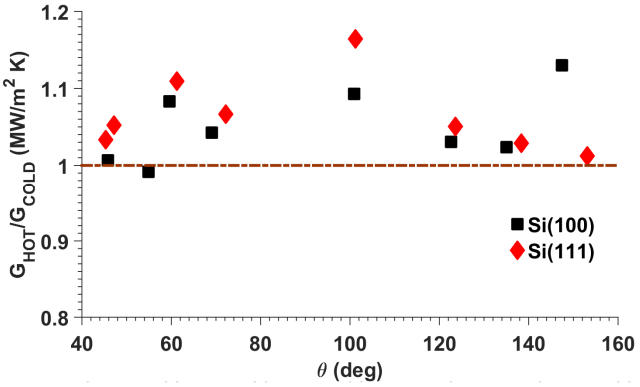

Figure 6.5: Ratio of the hot to cold thermal boundary conductance calculations for different wettability conditions.

6.2 Thermal boundary conductance between water and silicon under different wettability conditions

Figure 6.6 illustrates the characterization of the thermal transport properties of the different surfaces in contact with water as a function of wettability. The results reported in Figure 6.6 are the averages and standard deviations of G between hot and cold wall

calculations for different realizations. Consistent with the numerical investigation by Shenogina et al. [65] and the experimental findings by Harikrishna et al. [63], it was obtained that $G \sim 1+\cos\theta$ for both silicon surfaces, see Figure 6.6(a). It is clear that there is a lack of a universal relationship between the contact angle and *G*, since two curves are obtained for each silicon surface. The main difference between them is the atomic planar density ρ_s, being the Si(111) surface denser (7.83 nm^{-2}) and more closely packed in a bilayer structure than the Si(100) (6.87 nm^{-2}) with large interstitial spaces along the [111] direction. More noticeable, the two graphene-coated silicon surfaces exhibit a significantly lower *G* in comparison with the bare surfaces, even though the contact angle is the same. Figure 6.6(b) illustrates the direct dependence of *G* on the contact angle, a functional dependence presented for the first time for silicon and graphene-coated silicon surfaces. As expected, *G* increases as the surfaces become more hydrophilic, and just as in the previous case, the contact angle does not represent a universal parameter to correlate with the contact angle.

The linear dependences previously reported in Figure 6.6, namely, $G \sim 1+\cos\theta$ and $G \sim 180° - \theta$, can be partially deducted from the results reported in Figure 6.7, where the value of *G* is observed to increase as the silicon-water interaction strength (ε) increases and the fact that $\varepsilon \sim 1+\cos\theta$ and $\varepsilon \sim 180° - \theta$ [46]. These two scaling laws originate from a simplification performed on a mean-field model of wettability and have been previously verified for silicon in Figure 5.11. As in the case of the scaling laws depicted in Figure 6.6, two different linear relationships were found for the wettability of Si(111) and Si(100), being the Si(111) surface more hydrophilic than the Si(100) for the same value of ε. The different wettability of the Si(111) and Si(100) planes as a function of ε is understandable, since the lower atomic planar density of Si(100) demands for a larger value of ε to match the wettability of the Si(111) plane. From the comprehensive wettability model reported in Chapter 4, it is possible to realize that $\varepsilon\rho_s \sim 1+\cos\theta$, thus, the work of adhesion is scaled by the energy per unit area determined by the

concentration of solid atoms per plane. The application of this new scaling law to the wettability of different surfaces is depicted in Figure 6.8(a), where the difference in the wettability of different silicon planes reported in Figure 5.11 is no longer observed when the contact angle is characterized by the interaction energy per unit area ($\varepsilon\rho_s$). Results for the wettability of graphite reported in Figure 4.5 are also shown and the results for the graphene-coated surfaces were obtained by averaging the contribution of the silicon and graphene surfaces to the work of adhesion.

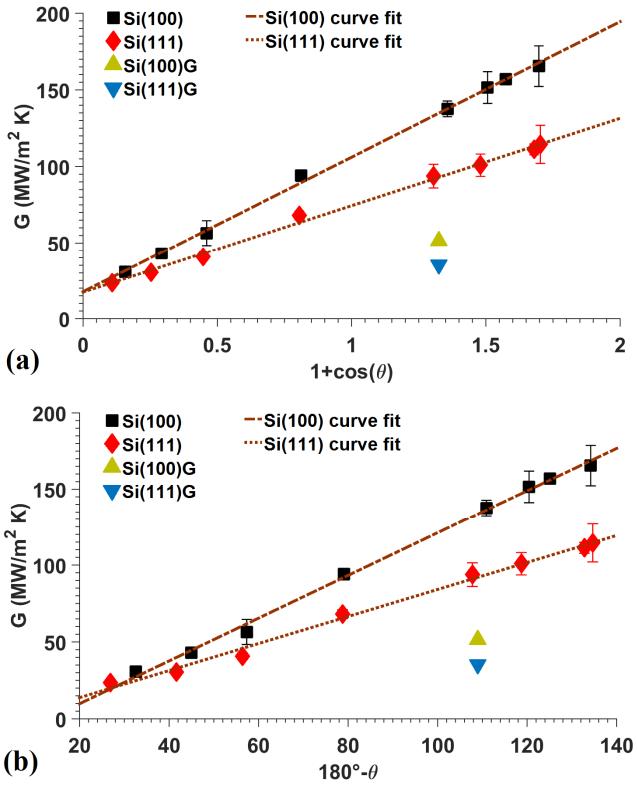

Figure 6.6: Thermal boundary conductance relationships for different silicon and graphene-coated silicon surfaces. (a) Thermal boundary conductance vs. the work of adhesion (1+cosθ) and (b) thermal boundary conductance vs. the contact angle.

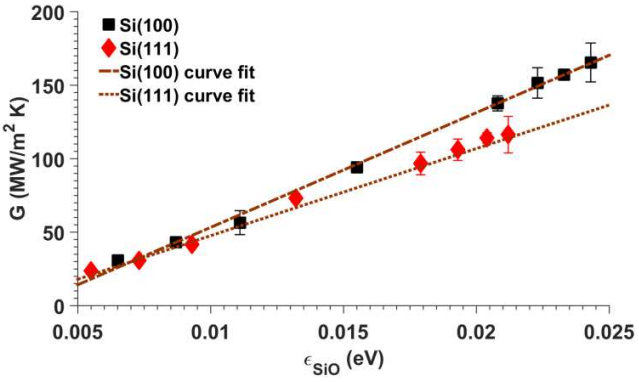

Figure 6.7: Thermal boundary conductance dependence on the silicon-water interaction strength.

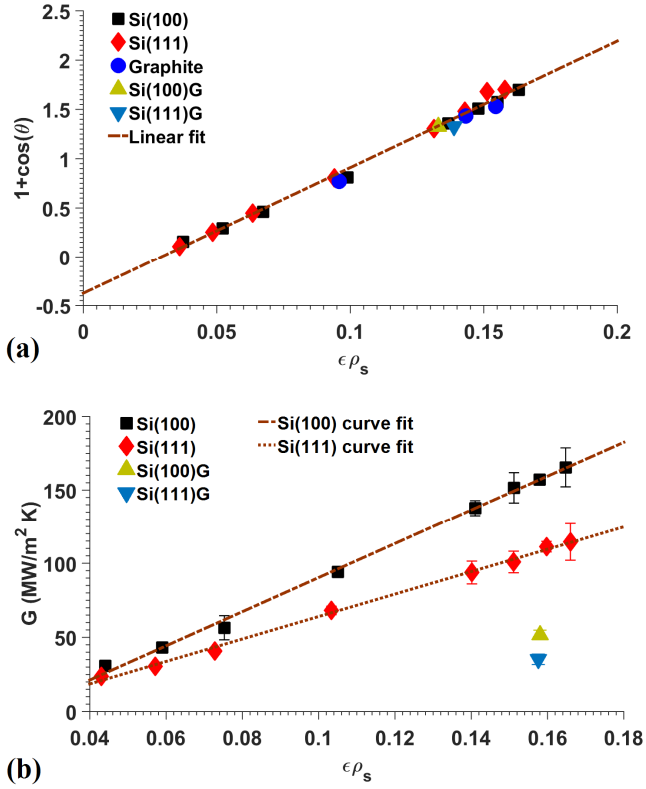

Figure 6.8: Reconciliation of the contact angle calculations using the solid-liquid interaction energy per unit area and (b) thermal boundary conductance vs. the solid-liquid interaction energy per unit area.

The reconciliation of the contact angle calculations brings an opportunity to test the dependence of *G* on the surface energy. Figure 6.8(a) illustrates that the behavior of *G*

is the same as that for the work of adhesion or $1+\cos\theta$. This is not surprising but was necessary to verify, since the wettability of the silicon surfaces was found to be crystallographic plane-dependent. Thus, by finding a unifying parameter able to reconcile the different contact angle calculations, but not the thermal transport, allows to conclude that the work of adhesion is not a universal parameter to explain the thermal transport across solid-liquid interfaces. The contact angle and surface energy correlations support this conclusion.

It is evident that having a large work of adhesion, or a hydrophilic surface, promotes an efficient solid-liquid thermal transport. However, the differences observed between the silicon and graphene-coated silicon surfaces calls for further analysis. As a first step, the phonons density of states (DOS) was obtained for an atomic monolayer in a region unaffected by the liquid (bulk) and for the atomic interfacial monolayers in contact with water. The fast Fourier transform of the velocity autocorrelation function of the solid atoms was used to obtain the DOS as indicated in Ref. [178]. Figure 6.9 illustrates the DOS in arbitrary units where the transverse (T), longitudinal (L), acoustic (A), and optical (O) modes are indicated. The DOS for the bulk monolayer features similar characteristics as those of the bulk material [179]. The TA modes for the interfacial monolayers for Si(100) and Si(111) feature similar properties as the bulk with a slight shift in frequency, something also reported in [80]. As for the LA and LO modes the bulk properties seem to be fairly preserved. The main difference exists in the high frequency transverse modes (TO). A drastic reduction of the DOS with respect to the bulk occurs in both silicon surfaces, indicating that the main mechanism of heat transfer is by high-frequency phonons being transmitted in the in-plane direction. In addition, and consistent with the results presented so far, a more noticeable reduction of the TO modes is observed for the Si(100) than for the Si(111) surface, indicating a more efficient heat transfer. Alternatively, Goicochea et al. [142] found that the low frequency phonons were the most significant modes for heat transfer in a quartz-water interface.

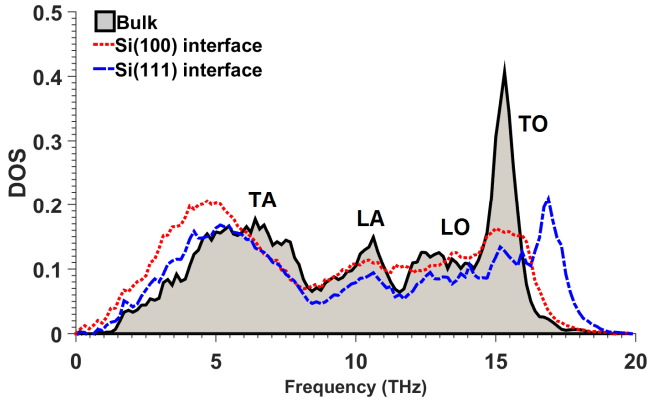

Figure 6.9: Phonon density of states (DOS) in arbitrary units of atomic layers in the bulk and interface of Si(100) and Si(111) in contact with water.

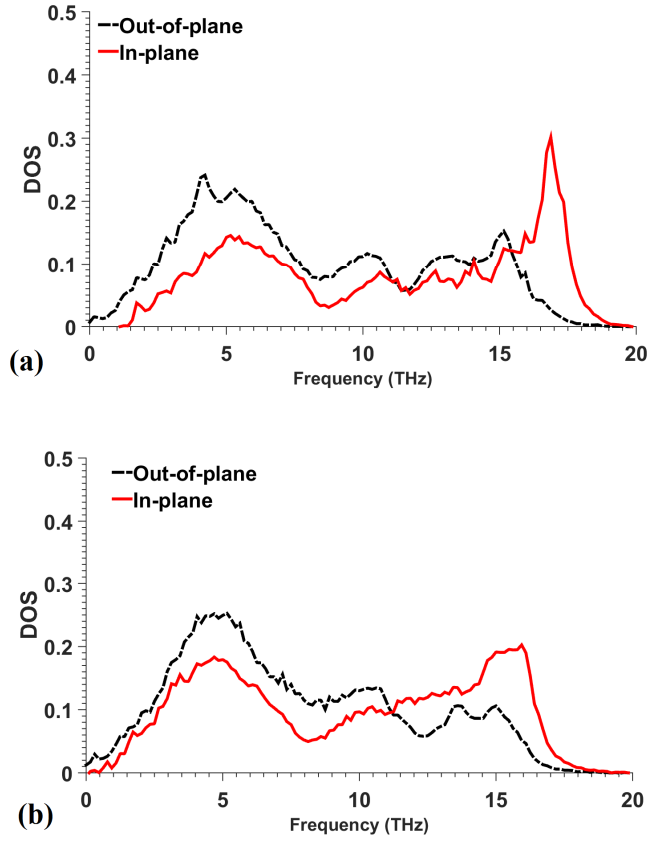

Figure 6.10: Decomposition in out-of-plane and in-plane phonon modes of interfacial (a) Si(111) and (b) Si(100) atoms.

In order to verify the nature of the phonons illustrated in Figure 6.9, a decomposition of the phonon modes in the out-of-plane and in-plane directions was performed and the results are illustrated in Figure 6.10. The sharp peak for the TO phonons modes coincides with the in-plane vibrational modes depicted in Figure 6.10(a) and a rather low concentration of out-of-plane phonons is observed at high frequencies. Figure 6.10(b) helps to verify that the low frequency phonon modes are comprised of transverse modes and that the small concentration of high frequency modes is mostly generated by the transmission of in-plane modes. A small contribution to the interfacial heat transfer is also observed from the reduction of the high frequency out-of-plane modes if the DOS between Si(111) and Si(100) are compared.

6.3 Thermal boundary conductance and the interfacial liquid structure

The results depicted in Figures 6.9 and 6.10 alleviate any concern about an improper characterization of the solid-liquid interactions as an explanation for the different thermal transport between silicon surfaces, and reaffirm the conclusion that the work of adhesion is not a universal parameter for describing the solid-liquid thermal transport. The fact that high frequency phonons transmitted in the in-plane direction account for most of the energy transfer between silicon and water, suggests an important effect of the interfacial liquid structure of water, which is a parameter strongly affected by the surface roughness. Water entrainment was observed in the large intersticia of the Si(100) plane in Figure 4.8, and in Section 5.2.3 the water entrainment was found to be of major importance in the description of the hydrodynamic boundary condition. As in the case of momentum transfer, thermal transport is affected by the effective contact between solid and liquid atoms. A quantification of the equilibrium distance between phases can be obtained by the density depletion length (Equation (5.1)). Figure 6.11 illustrates the correlation between the density depletion and the interfacial thermal transport. A unified description of the thermal transport phenomenon is achieved for the different surfaces

when the interfacial density depletion is used as a parameter. The water entrainment previously reported for the Si(100) surface is responsible for the small δ of this surface for the hydrophilic cases, hence explaining the larger values of *G*, as indicated also by the phonons DOS. In other words, if the density depletion is small and water entrainment is observed, the transmission of the transverse phonon modes is more effective, as indicated in Figure 6.9. The smaller *G* of the denser Si(111) plane is explained due to the larger δ observed for this surface due to the closely packed structure of this plane. Lastly and more importantly, the *G* for the graphene-coated silicon surfaces is properly matched with the bare surfaces having the same density depletion. A characterization of the solid-liquid potential energy corrugation of these surfaces was reported in Figure 4.15.

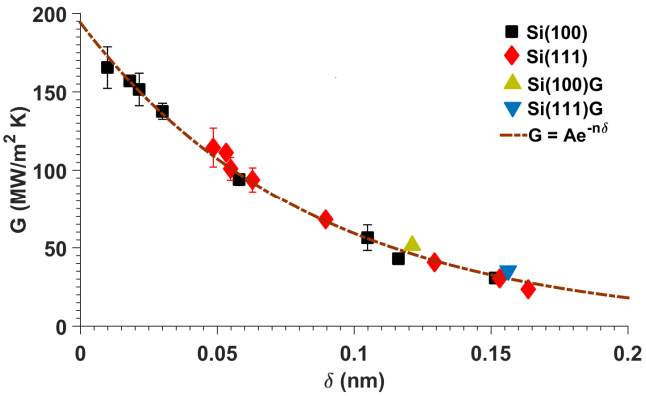

Figure 6.11: Reconciliation of the thermal boundary conductance calculated for different surfaces in contact with water using the density depletion length.

Xue et al. [137] determined that the liquid layering at the solid-liquid interface has a negligible effect on the liquid thermal properties, but it was suggested that the liquid depletion could have an effect on the interfacial thermal resistance. Torii et al. [138] investigated the directional heat transfer contributions to the interfacial thermal transport in simple systems. The roughness of the solid structure was modified in order to alter the corrugation of the energy potential between the solid and liquid phases. Torii et al. [138] found a strong contribution of the in-plane energy fluxes, consistent with the DOS depicted in Figure 6.9 and a from their results, a correlation between the density depletion

(concentration of liquid particles and equilibrium distance) and *G* could be formulated but was not quantified. Pham et al. [143] used a weak interpretation of the depletion length (position of the first liquid density peak) that suggested a correlation between thermal transport and the equilibrium distance between the phases. None of these previous investigations proposed or observed a correlation as that depicted in Figure 6.11, and to the best of our knowledge this is the first time the density depletion length has been used to explain the solid-liquid thermal transport. The best fit to the data reported in Figure 6.11 was an exponential function (R^2 = 0.99), where the upper limit of the conductance was extrapolated at 195 MW/m^{2}K and the parameter n = -0.5. The upper limit of G when $\delta \rightarrow 0$ encloses the maximum values of G experimentally reported by Ge et al. [62] and Harriskrishna et al. [63] for highly hydrophilic surfaces.

Lastly, and in an effort to provide visual aid for the interpretation of the results previously discussed, Figure 6.12 illustrates the water density layering at the interface of Si(100), Si(111), and graphene-coated silicon under the same wettability conditions θ = 71°, Figure 6.12(a), and snapshots of the interface of these surfaces in contact with water, Figures 6.12(b-d). The characteristic of the density layering and depletion length (interfacial liquid structure) for these surfaces was previously discussed in Chapter 4. It was indicated that when the spatial shift between density peaks is removed, the interfacial concentration of liquid particles is very similar between the three surfaces. But, when the density depletion length is calculated using Equation (5.1), the equilibrium separation between liquid particles gives origin to the differences observed in the hydrodynamic and thermal transport phenomena. Figure 6.12(b) clearly depicts water entrainment and a negligible density depletion length, thus, an effective thermal transport is expected and can be observed why the transverse phonon modes can be efficiently transferred to the water in this interface. Figure 6.12(c) illustrates how the more closely packed Si(111) interface generates a more noticeable water depletion, thus, suggesting a reduction in the efficiency of the thermal transport process in this interface. Figure 6.12(d) illustrates an

example of large density depletion on graphene-coated silicon. It must be remarked that this surface has the same wettability as the others. By having such a large separation between the water molecules and the interfacial solid atoms, a rather deficient thermal transport is in order for the graphene-coated surface as indicated in Figure 6.11. These arguments prove the lack of generality for correlating interfacial phenomena with the contact angle derived from size-independent MD simulations of wettability. While the contact angle can be calibrated to match a given experimental value in simulations, the magnitude of the density depletion is a function of the solid structure properties coupled with the granularity of the solid-liquid interaction potential, and this parameter governs the efficiency of momentum and thermal transport across interfaces.

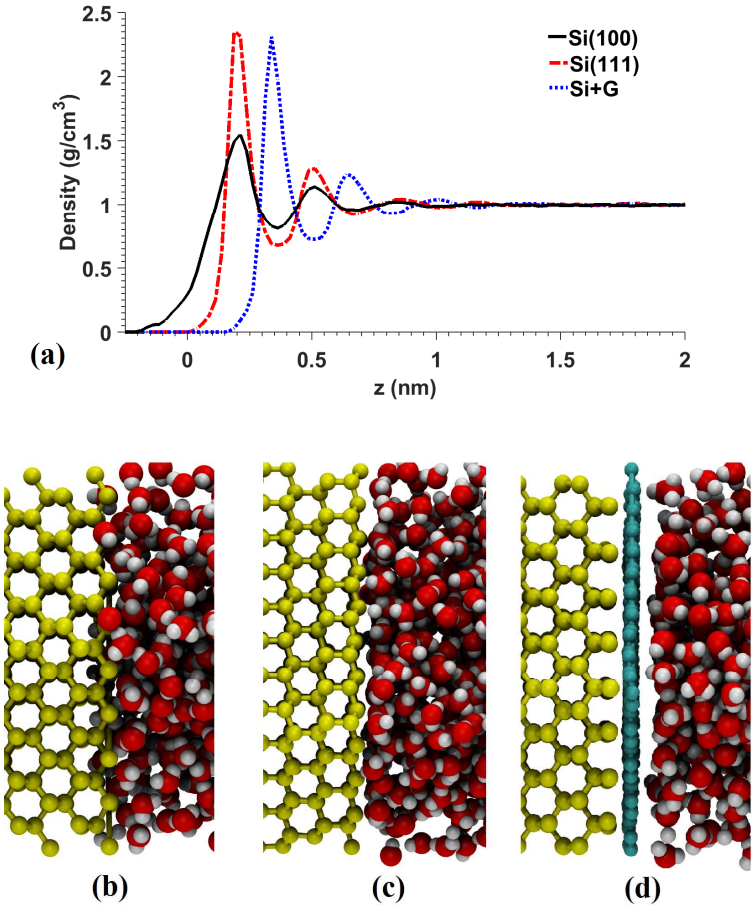

Figure 6.12: (a) Density layering and snapshots of the interfaces of (b) Si(100), (c) Si(111), and Si(100) coated with graphene under the same wettability conditions, $\theta = 71°$.

6.4 Summary

A critical assessment of the effects of surface wettability on the interfacial thermal transport was reported in this Chapter. The wettability of different crystallographic silicon planes in contact with water was previously characterized in Chapter 4, and that information was used as the foundation to conduct a sound investigation of the thermal transport between silicon and water. In order to bring an additional level of robustness to this investigation, the wettability transparency of graphene-coated silicon was considered in an effort to elucidate the relationship between wettability and the thermal boundary conductance. Two surfaces with the same wettability, as demonstrated by experiments, simulations, and theory, were used to investigate the heat transfer-wettability relationship, instead of the common artificial manipulation of the wettability conditions.

An agreement was found between the current numerical simulation results and previous simulation and experimental investigations, in terms of the magnitude and trend of the thermal boundary conductances calculated in a given range of wettability conditions. It was found that the heat transfer-wettability relationship loses generality when surfaces having different atomic surface roughness are investigated, and a more significant lack of consistency was observed when a complex surface with the same contact angle as a bare one is analyzed (graphene-coated silicon). Alternatively, the liquid density depletion length (an interfacial liquid structure property) was the parameter that reconciled the different thermal conductivity calculations between different bare silicon and graphene-coated silicon surfaces. These results were supported by an spectral analysis of phonons for the different silicon surfaces. Lastly, a visualization of the interfaces helped to give a physical sense of the meaning of the density depletion length as a parameter determining the effectiveness of thermal transport by closeness or coupling of the atomic vibrations at the solid-liquid interface.

CHAPTER 7

CONCLUSIONS

This Chapter contains a summary of the investigation reported in this dissertation and the conclusions drawn from the obtained results. Recommendations for future investigations and supportive concluding remarks are presented at the end of this dissertation. This Chapter constitutes the completion of this investigation.

7.1 Summary and conclusions

Momentum and thermal transport at solid-liquid interfaces were investigated by means of classical atomistic simulations and a strong theoretical background. In particular, this dissertation dealt with silicon-water systems due to the rising importance of silicon-based sensors and devices that operate in aqueous environments. The main objective of this investigation was to perform a critical assessment of the relationship between surface chemistry and momentum/heat transfer in nanoconfined water. The surface chemistry was characterized by means of calculations of the static contact angle using equilibrium simulations of droplet wettability. The wettability of two crystallographic silicon planes, Si(100) and Si(111), was investigated in order to introduce the effects of surface granularity. Additionally, the wettability of graphene-coated silicon surfaces was considered so that a broader the perspective of the effects of wettability on momentum and thermal transport.

On the specific contributions to the understanding and modeling of wettability, a formalized method was proposed for the calculation of the static contact angle from atomistic simulations and a simple but effective single-parameter theoretical model of wettability was developed. Molecular dynamics simulation of droplets wettability are commonly used to obtain the time-average positions of liquid particles and then define

the geometry of the droplets in order to calculate the contact angle. A methodology to perform these calculations was proposed, in which the contact angle, bulk density, and the quality indicators of the functional fits performed to calculate these parameters are tracked as a function of the data sets analyzed over time. By employing this method, any analysts can define the conditions required to determine whether or not the calculations of the contact angle are reliable. Likewise, this methodology can be easily used to determine the steadiness of the calculations over time. The application of this methodology led to accurate and repeatable calculations of the contact angle between independent simulations. From the theoretical point of view, a simple but effective calibration to the density distribution of liquid particles in contact with a solid was proposed in order to improve on the accuracy of mean-field theory models of wettability. By introducing a single fitting parameter and considering the discrete contributions to the solid-liquid interactions by every solid atomic layer, an accurate match between atomistic simulations and theory was found. Although this theoretical model required from fitting for individual solids, its predictive capabilities were significant for graphene-coated silicon surfaces. The physically sound derivation of this model led to not only obtain accurate calculations of the contact angle but also interfacial liquid properties, consistent with atomistic simulations.

The carbon-water non-bonded interaction potential was calibrated by means of matching the experimental contact angle measured on a free-of-contaminants graphite surface with atomistic simulations, a calibration performed for the first time since researchers found that atmospheric hydrocarbons get absorbed onto carbon surfaces, making them more hydrophobic. The wettability of Si(111) and Si(100) was different between these two planes when the same interaction potential between solid and liquid particles was used. Si(111) was more hydrophilic than Si(100) due to having a larger planar atomic density and a closely packed structure denoted by a periodic atomic bilayer in the normal direction to the (111) plane. The numerical simulation results were

theoretically supported regarding the anisotropy effect on wettability. Later on, it was discovered that in order to explain the anisotropy of wettability, the solid-liquid energy had to be normalized by the concentration of solid atoms per unit area. Once the individual wettability of silicon and graphitic carbon was numerically and theoretically characterized, an investigation of the conditions leading to wettability transparency was conducted. Numerical and theoretical calculations matched for a wide range of silicon wettability conditions and equilibrium configurations of the graphene-silicon surface. Thus, the macroscopic conditions (substrate contact angle) and microscopic conditions (interfacial concentration of liquid particles and energy potential granularity) required to observe wettability transparency were identified. It was found that the silicon-water interactions were neither blocked by the graphene layer, as proposed by the wettability opaqueness theory, nor fully transmitted, as suggested by the wettability transparency theory. Instead, a set of conditions encompassing the equilibrium distance between solid and liquid particles and the granularity of the solid-liquid potential energy field affected the wettability of coated surfaces.

Previous investigations have suggested that there is a strong correlation between the wettability of the solid surfaces and the nature of the hydrodynamic boundary condition in nanoconfined liquids. A critical assessment of these claims was performed by means of investigating hydrodynamic slip in silicon nanochannels with artificially modified wettability and in graphene-coated nanochannels under wettability transparency conditions. Thus, nanochannels with complex and simple surfaces having the same contact angle were used to investigate the relationship between the contact angle and the type of hydrodynamic boundary condition. The sound investigation of the surface chemistry and solid-liquid interfacial properties were used to provide a new perspective of the hydrodynamic slip problem.

Before conducting the slip-wettability investigation, a critical evaluation of the current available theories to calculate the hydrodynamic slip in nanoconfined liquids was

conducted, as there is a lack of consensus on whether or not the hydrodynamic slip length is a surface property and the reliability of the calculations of this parameter using Green-Kubo like expressions. Four theories were evaluated in terms of consistency of the calculations between independent simulations and reliability with respect to non-equilibrium calculations in the low-shear rate limit. Three of the four theories reported consistent calculations but different trends with respect to the magnitude of the slip length. Likewise, difficulties were found in the evaluation of the solid-liquid friction coefficient from two of the three remaining theories due to the nature of the Green-Kubo-like expressions used. On aspect was consistent between equilibrium theories of hydrodynamic slip, size effects were present and statistically noticeable in one of the models, the most reliable one. It was found that these size effects were caused by the high mobility of the water molecules within the confinement. Thus, it was found for the first time that in order for the slip length to be considered a surface property, the size of the confinement must be large enough such that the mobility of the liquid particles is constrained to the interface regions, which have a finite size. If these interface regions overlap between confining walls, then the definition of surface property breaks down.

Silicon and graphene-coated silicon nanochannels with dimensions large enough to avoid size dependence were used to assess the wettability effect on the hydrodynamic slip. Likewise, compressibility effects were eliminated by means of enforcing similar bulk density and pressure in the confined water. The results indicated that the slip-wettability quasiuniversal laws break down for silicon nanochannels having different crystallographic planes facing water even if the contact angle is the same. More significantly, a rather drastic break down was found when the wettability transparency phenomenon is introduced. Bare and graphene-coated silicon nanochannels showed different hydrodynamic boundary conditions even though the wettability of the surfaces was the same. Interestingly, the different results followed a universal trend once the slip length was plotted as a function of one interfacial liquid property, the density depletion

length. Essentially, the density depletion length determines how effective is the momentum exchange between the solid and liquid atoms by considering the distance between the two phases in equilibrium. The density depletion length is affected by the entrainment of liquid particles in the large intersticia of the Si(100) surface and the uniform layering caused by a highly dense graphene layer facing water. The Si(100) surface presented a rough attractive potential energy landscape to the water molecules, thus promoting a no-slip boundary condition, whereas the same surface coated with graphene presented a smooth landscape over which the liquid particles were prone to slip, even though the surface wettability was the same. It was concluded that the contact angle is not a universal parameter to explain the hydrodynamic boundary condition in nanoconfined liquids, but that an interfacial liquid property, like the density depletion length, is more effective as it encompasses the solid-liquid interaction potential granularity effect and the strength of the solid-liquid affinity.

The structure of these dissertation and that of the conclusions drawn so far followed the same path as the investigation conducted. Thus, by the time the effects of wettability on the solid-liquid thermal transport were investigated, much knowledge had already been gained from the strong chemical physics foundations used to characterize the wettability of silicon and graphite and then from the investigation on the interfacial momentum transport. The last objective within the scope of this dissertation was to evaluate the relationship between wettability and the thermal boundary conductance at the interface between silicon and water. Non-equilibrium atomistic simulations were used to determine the effectiveness of thermal transport between silicon and water and graphene-coated silicon and water under wettability transparency conditions. Previous investigations have numerically and experimentally reported a linear relationship between the work of adhesion (function of the static contact angle) and the thermal boundary conductance. The wettability of different substrates is commonly altered by means of chemical functionalization and it is assumed that the thermal resistance of these

chemical groups is negligible. Therefore, the purpose of this investigation was to critically assess if the work of adhesion could be used to universally characterize the interfacial thermal transport. A verification of the linear relationships previously reported was obtained; however, the Si(111) and Si(100) exhibited different thermal behavior, being the Si(100) interface more thermally conductive than the Si(111) under the same wettability conditions. More importantly, a significant break down of these tendencies was found for the graphene-coated silicon interfaces under wettability transparency conditions, being these systems significantly less thermally conductive than the bare silicon surfaces. At this point, the experience gained through the previous analyses, led to formulate the possibility of correlating all of the thermal boundary conductance calculations with the density depletion length. A remarkable and groundbreaking universal description of the interfacial thermal transport was found for the first time. Similar to the momentum transport process, the thermal energy transport at solid-liquid interfaces is governed by the availability of liquid particles at the interface as energy carriers. Therefore, the greater interfacial conductivity of the Si(100) surface was explained in terms of the water entrainment of observed in this surface and the poor conductance of graphene-coated systems due to the large gap between the solid and liquid phases in equilibrium. These results were supported by an spectral analysis of phonons at the interface and together make a compelling case of the findings reported herein.

7.2 Recommendations for future investigations

The interaction potential used in atomistic simulations for a single material is usually calibrated after matching numerical calculations of a given property with its corresponding experimental value. This practice is common and has shown to be successful in some cases and no so much in complex substances, like water. Mixing rules have been used to try to get an idea of the interaction of two different materials, but such

a practice has no experimental of theoretical justification. For the solid-liquid interactions, the calibration of the interaction potential is conducted such that an experimental contact angle can be matched by means of simulations. The effectiveness of this practice is still unknown, but can be determined by means of experimentally measuring other interfacial phenomena, such as the hydrodynamic slip and thermal transport in nanoconfined liquids, just as the numerical investigation reported here. However, the reliability of these measurements is limited by the current technology. Nevertheless, the following recommendations are proposed for future investigations:

1. Characterization of the solid-liquid interface. The reliability of the numerical simulations of interfacial phenomena can be improved if data is available about the average size of the liquid and solid particles. Additionally, the equilibrium distance between the solid and liquid atoms would be of great help in narrowing down a proper characterization of the solid-liquid interface. This information can be obtained from a limited number of experimental investigations or it can be obtained from first principles simulations.
2. *Ab-initio* simulations. The interaction potential between solids and a water molecule can be obtained from *ab-initio* simulations; likewise, the equilibrium distance can be calculated. Precaution is required if this approach is going to be undertaken. Investigations report a significant effect of the orientation of the water molecule on the interaction potential. Additionally, some investigations have reported the lack of effectiveness using ab-initio-derived potentials for applications in wettability simulations, but how about hydrodynamics and thermal transport simulations?
3. ELBA coarse-grain water model. Recently, the ELBA water model has shown promising predictive capabilities, since this is a coarse-grain model, only one parameter is used to calibrate the solid-liquid interaction potential.

4. Slip in nanochannels made of other anisotropic materials. The hydrodynamic slip relationship obtained herein could be further validates by investigating hydrodynamic slip in nanochannels having a directional structure dependence.
5. Wettability transparency of other 2D materials. The possibility of observing wettability transparency and similar thermal and hydrodynamic effects using other 2D materials could be an interesting area of research.
6. High-shear rate limit. The nature of the hydrodynamic boundary condition in the high-shear rate limit is still unknown and could be interesting to unravel the surface wettability effects in that regime.
7. Coupling thermal and momentum transport. This investigation was conducted in the low-shear rate limit where thermal and momentum transport are uncoupled. However, as the shear rate increases, the hydrodynamic boundary condition is modified and also the interfacial liquid structure as the liquid particles slip away from the surface; thus, the thermal transport is affected by the interfacial structure changes. At the same time, a deficient thermal transport alters the nature of the hydrodynamic boundary condition. This is a highly coupled problem.

Many more similar suggestions could be listed, but the main recommendation that can be made for future investigations is that the interfacial liquid structure properties must characterized as close as possible to the actual system, which is currently a major challenge.

7.3 Final remarks

This investigation demonstrated that the wettability of surfaces, characterized by the static contact angle obtained from atomistic simulations, is correlated with the momentum and thermal transport at solid-liquid interfaces, but only partially. The density depletion length, an interfacial liquid structure property, was proposed as a universal parameter to describe the hydrodynamic boundary condition and thermal transport at

solid-liquid interfaces. The generality of these findings is yet to be determined, but a solid foundation was established here in by means of a strong theoretical background consistently supported by atomistic simulations. The findings regarding the hydrodynamic boundary condition correlation had been previously reported and this investigation served to provide further validation employing the complex wettability transparency phenomenon. On the thermal transport analysis, a theory based on the framework of phonons thermodynamics was previously proposed to provide a good explanation of the wettability effect. In this investigation, the same problem was approached from a different perspective, based on the interfacial liquid properties, and groundbreaking results were obtained. The description of the thermal transport phenomena using the interfacial liquid structure lays the foundations for future investigations and it can be seen as the discovery of one piece of the interfacial heat transfer puzzle.

REFERENCES

[1] Guo, L.J., X. Cheng, and C.F. Chou, Fabrication of size-controllable nanofluidic channels by nanoimprinting and its application for DNA stretching. *Nano Letters*, 2004. **4**(1): p. 69-73.

[2] Sun, W., P. Qin, H.W. Gao, G.C. Li, and K. Jiao, Electrochemical DNA biosensor based on chitosan/nano-V2O5/MWCNTs composite film modified carbon ionic liquid electrode and its application to the LAMP product of Yersinia enterocolitica gene sequence. *Biosensors & Bioelectronics*, 2010. **25**(6): p. 1264-1270.

[3] Sunkara, V., B.J. Hong, and J.W. Park, Sensitivity enhancement of DNA microarray on nano-scale controlled surface by using a streptavidin-fluorophore conjugate. *Biosensors & Bioelectronics*, 2007. **22**(7): p. 1532-1537.

[4] Turley, A., Nanotechnology Nano-assembly line starts up with DNA workers. *Chemistry & Industry*, 2010(10): p. 9-9.

[5] Lee, W.H., C.Y. Loo, D. Traini, and P.M. Young, Nano- and micro-based inhaled drug delivery systems for targeting alveolar macrophages. *Expert Opinion on Drug Delivery*, 2015. **12**(6): p. 1009-1026.

[6] Lopez-Salazar, R., S. Camacho-Leon, L. Olivares-Quiroz, and J. Hernandez, Design and Simulation of a High Precision Drug Delivery System. *2012 Iberoamerican Conference on Electronics Engineering and Computer Science*, 2012. **3**: p. 334-341.

[7] Mazibuko, Z., Y.E. Choonara, P. Kumar, L.C. Du Toit, G. Modi, D. Naidoo, and V. Pillay, A Review of the Potential Role of Nano-Enabled Drug Delivery Technologies in Amyotrophic Lateral Sclerosis: Lessons Learned from Other Neurodegenerative Disorders. *Journal of Pharmaceutical Sciences*, 2015. **104**(4): p. 1213-1229.

[8] Sinha, P.M., G. Valco, S. Sharma, X.W. Liu, and M. Ferrari, Nanoengineered device for drug delivery application. *Nanotechnology*, 2004. **15**(10): p. S585-S589.

[9] Wang, G.H., W.B. Mao, R. Byler, K. Patel, C. Henegar, A. Alexeev, and T. Sulchek, Stiffness Dependent Separation of Cells in a Microfluidic Device. *Plos One*, 2013. **8**(10).

[10] Wang, G.H., W.B. Mao, C. Henegar, A. Alexeev, and T. Sulchek, Stiffness Dependent Separation of Cells in a Microfluidic Device. *Proceedings of the Asme Summer Bioengineering Conference, Pts a and B*, 2012: p. 241-242.

[11] Daiguji, H., P.D. Yang, A.J. Szeri, and A. Majumdar, Electrochemomechanical energy conversion in nanofluidic channels. *Nano Letters*, 2004. **4**(12): p. 2315-2321.

[12] Siria, A., P. Poncharal, A.L. Biance, R. Fulcrand, X. Blase, S.T. Purcell, and L. Bocquet, Giant osmotic energy conversion measured in a single transmembrane boron nitride nanotube. *Nature*, 2013. **494**(7438): p. 455-458.

[13] Nair, R.R., H.A. Wu, P.N. Jayaram, I.V. Grigorieva, and A.K. Geim, Unimpeded Permeation of Water Through Helium-Leak-Tight Graphene-Based Membranes. *Science*, 2012. **335**(6067): p. 442-444.

[14] Constantin, D. and Z.S. Siwy, Poisson-Nernst -Planck model of ion current rectification through a nanofluidic diode. *Physical Review E*, 2007. **76**(4).
[15] Fan, R., M. Yue, R. Karnik, A. Majumdar, and P.D. Yang, Polarity switching and transient responses in single nanotube nanofluidic transistors. *Physical Review Letters*, 2005. **95**(8).
[16] Karnik, R., R. Fan, M. Yue, D.Y. Li, P.D. Yang, and A. Majumdar, Electrostatic control of ions and molecules in nanofluidic transistors. *Nano Letters*, 2005. **5**(5): p. 943-948.
[17] Nguyen, G. and Z. Siwy, Rectification of a Modified Nanofluidic Diode Dependent on the pH. *Biophysical Journal*, 2010. **98**(3): p. 602a-602a.
[18] Paik, K.H., Y. Liu, V. Tabard-Cossa, M.J. Waugh, D.E. Huber, J. Provine, R.T. Howe, R.W. Dutton, and R.W. Davis, Control of DNA Capture by Nanofluidic Transistors. *Acs Nano*, 2012. **6**(8): p. 6767-6775.
[19] Vlassiouk, I. and Z.S. Siwy, Nanofluidic diode. *Nano Letters*, 2007. **7**(3): p. 552-556.
[20] Chen, Y.F., D.Y. Li, K. Jiang, J.K. Yang, X.H. Wang, and Y.J. Wang, Hydrodynamic lubrication in nanoscale bearings under high shear velocity. *Journal of Chemical Physics*, 2006. **125**(8).
[21] Majumder, M., N. Chopra, R. Andrews, and B.J. Hinds, Nanoscale hydrodynamics - Enhanced flow in carbon nanotubes. *Nature*, 2005. **438**(7064): p. 44-44.
[22] Thomas, J.A. and A.J.H. McGaughey, Reassessing fast water transport through carbon nanotubes. *Nano Letters*, 2008. **8**(9): p. 2788-2793.
[23] Bocquet, L. and E. Charlaix, Nanofluidics, from bulk to interfaces. *Chem Soc Rev*, 2010. **39**(3): p. 1073-95.
[24] Tretheway, D.C. and C.D. Meinhart, Apparent fluid slip at hydrophobic microchannel walls. *Physics of Fluids*, 2002. **14**(3): p. L9-L12.
[25] Bhushan, B., Y. Wang, and A. Maali, Boundary Slip Study on Hydrophilic, Hydrophobic, and Superhydrophobic Surfaces with Dynamic Atomic Force Microscopy. *Langmuir*, 2009. **25**(14): p. 8117-8121.
[26] Bonaccurso, E., M. Kappl, and H.J. Butt, Hydrodynamic force measurements: Boundary slip of water on hydrophilic surfaces and electrokinetic effects. *Physical Review Letters*, 2002. **88**(7).
[27] Zhu, Y.X. and S. Granick, Limits of the hydrodynamic no-slip boundary condition. *Physical Review Letters*, 2002. **88**(10).
[28] Bouzigues, C.I., P. Tabeling, and L. Bocquet, Nanofluidics in the debye layer at hydrophilic and hydrophobic surfaces. *Physical Review Letters*, 2008. **101**(11).
[29] Chan, D.Y.C. and R.G. Horn, The Drainage of Thin Liquid-Films between Solid-Surfaces. *Journal of Chemical Physics*, 1985. **83**(10): p. 5311-5324.
[30] Cottin-Bizonne, C., B. Cross, A. Steinberger, and E. Charlaix, Boundary slip on smooth hydrophobic surfaces: Intrinsic effects and possible artifacts. *Physical Review Letters*, 2005. **94**(5).
[31] Cottin-Bizonne, C., A. Steinberger, B. Cross, O. Raccurt, and E. Charlaix, Nanohydrodynamics: The intrinsic flow boundary condition on smooth surfaces. *Langmuir*, 2008. **24**(4): p. 1165-1172.
[32] Joseph, P. and P. Tabeling, Direct measurement of the apparent slip length. *Physical Review E*, 2005. **71**(3).

[33] Lasne, D., A. Maali, Y. Amarouchene, L. Cognet, B. Lounis, and H. Kellay, Velocity profiles of water flowing past solid glass surfaces using fluorescent nanoparticles and molecules as velocity probes. *Physical Review Letters*, 2008. **100**(21).
[34] Maali, A., T. Cohen-Bouhacina, and H. Kellay, Measurement of the slip length of water flow on graphite surface. *Applied Physics Letters*, 2008. **92**(5).
[35] Vinogradova, O.I., K. Koynov, A. Best, and F. Feuillebois, Direct Measurements of Hydrophobic Slippage Using Double-Focus Fluorescence Cross-Correlation. *Physical Review Letters*, 2009. **102**(11).
[36] Giannakopoulos, A.E., F. Sofos, T.E. Karakasidis, and A. Liakopoulos, Unified description of size effects of transport properties of liquids flowing in nanochannels. *International Journal of Heat and Mass Transfer*, 2012. **55**(19-20): p. 5087-5092.
[37] Liu, C. and Z. Li, Flow regimes and parameter dependence in nanochannel flows. *Physical Review E*, 2009. **80**(3).
[38] Liu, C. and Z. Li, On the validity of the Navier-Stokes equations for nanoscale liquid flows: The role of channel size. *AIP Advances*, 2011. **1**(3): p. 032108.
[39] Pahlavan, A.A. and J.B. Freund, Effect of solid properties on slip at a fluid-solid interface. *Physical Review E*, 2011. **83**(2).
[40] Xu, J. and Y. Li, Boundary conditions at the solid–liquid surface over the multiscale channel size from nanometer to micron. *International Journal of Heat and Mass Transfer*, 2007. **50**(13-14): p. 2571-2581.
[41] Zhang, Z., H. Zhang, and H. Ye, Pressure-driven flow in parallel-plate nanochannels. *Applied Physics Letters*, 2009. **95**(15): p. 154101.
[42] Barrat, J.L. and L. Bocquet, Influence of wetting properties on hydrodynamic boundary conditions at a fluid/solid interface. *Faraday Discussions*, 1999. **112**: p. 119-127.
[43] Barrat, J.L. and L. Bocquet, Large slip effect at a nonwetting fluid-solid interface. *Physical Review Letters*, 1999. **82**(23): p. 4671-4674.
[44] Ho, T.A., D.V. Papavassiliou, L.L. Lee, and A. Striolo, Liquid water can slip on a hydrophilic surface. *Proc Natl Acad Sci U S A*, 2011. **108**(39): p. 16170-5.
[45] Huang, D.M., C. Sendner, D. Horinek, R.R. Netz, and L. Bocquet, Water Slippage versus Contact Angle: A Quasiuniversal Relationship. *Physical Review Letters*, 2008. **101**(22).
[46] Sendner, C., D. Horinek, L. Bocquet, and R.R. Netz, Interfacial water at hydrophobic and hydrophilic surfaces: slip, viscosity, and diffusion. *Langmuir*, 2009. **25**(18): p. 10768-81.
[47] Voronov, R.S., D.V. Papavassiliou, and L.L. Lee, Boundary slip and wetting properties of interfaces: correlation of the contact angle with the slip length. *J Chem Phys*, 2006. **124**(20): p. 204701.
[48] Voronov, R.S., D.V. Papavassiliou, and L.L. Lee, Slip length and contact angle over hydrophobic surfaces. *Chemical Physics Letters*, 2007. **441**(4-6): p. 273-276.
[49] Zhang, H., Z. Zhang, and H. Ye, Molecular dynamics-based prediction of boundary slip of fluids in nanochannels. *Microfluidics and Nanofluidics*, 2011. **12**(1-4): p. 107-115.

[50] Thompson, P.A. and M.O. Robbins, Shear-Flow near Solids - Epitaxial Order and Flow Boundary-Conditions. *Physical Review A*, 1990. **41**(12): p. 6830-6837.
[51] Thompson, P.A. and M.O. Robbins, Origin of Stick-Slip Motion in Boundary Lubrication. *Science*, 1990. **250**(4982): p. 792-794.
[52] Kannam, S.K., B.D. Todd, J.S. Hansen, and P.J. Daivis, Slip flow in graphene nanochannels. *J Chem Phys*, 2011. **135**(14): p. 144701.
[53] Li, L., J. Mo, and Z. Li, Flow and slip transition in nanochannels. *Physical Review E*, 2014. **90**(3).
[54] Martini, A., H.-Y. Hsu, N.A. Patankar, and S. Lichter, Slip at High Shear Rates. *Physical Review Letters*, 2008. **100**(20).
[55] Martini, A., A. Roxin, R.Q. Snurr, Q. Wang, and S. Lichter, Molecular mechanisms of liquid slip. *Journal of Fluid Mechanics*, 2008. **600**.
[56] Priezjev, N.V., Effect of surface roughness on rate-dependent slip in simple fluids. *Journal of Chemical Physics*, 2007. **127**(14).
[57] Priezjev, N.V., Rate-dependent slip boundary conditions for simple fluids. *Physical Review E*, 2007. **75**(5).
[58] Sega, M., M. Sbragaglia, L. Biferale, and S. Succi, Regularization of the slip length divergence in water nanoflows by inhomogeneities at the Angstrom scale. *Soft Matter*, 2013. **9**(35): p. 8526-8531.
[59] Thompson, P.A. and S.M. Troian, A general boundary condition for liquid flow at solid surfaces. *Nature*, 1997. **389**(6649): p. 360-362.
[60] Zhu, Y.X. and S. Granick, Rate-dependent slip of Newtonian liquid at smooth surfaces. *Physical Review Letters*, 2001. **87**(9): p. art. no.-096105.
[61] Tocci, G., L. Joly, and A. Michaelides, Friction of water on graphene and hexagonal boron nitride from ab initio methods: very different slippage despite very similar interface structures. *Nano Letters*, 2014. **14**(12): p. 6872-7.
[62] Ge, Z.B., D.G. Cahill, and P.V. Braun, Thermal conductance of hydrophilic and hydrophobic interfaces. *Physical Review Letters*, 2006. **96**(18).
[63] Harikrishna, H., W.A. Ducker, and S.T. Huxtable, The influence of interface bonding on thermal transport through solid-liquid interfaces. *Applied Physics Letters*, 2013. **102**(25).
[64] Acharya, H., N.J. Mozdzierz, P. Keblinski, and S. Garde, How Chemistry, Nanoscale Roughness, and the Direction of Heat Flow Affect Thermal Conductance of Solid-Water Interfaces. *Industrial & Engineering Chemistry Research*, 2012. **51**(4): p. 1767-1773.
[65] Shenogina, N., R. Godawat, P. Keblinski, and S. Garde, How Wetting and Adhesion Affect Thermal Conductance of a Range of Hydrophobic to Hydrophilic Aqueous Interfaces. *Physical Review Letters*, 2009. **102**(15).
[66] Xue, L., P. Keblinski, S.R. Phillpot, S.U.S. Choi, and J.A. Eastman, Two regimes of thermal resistance at a liquid-solid interface. *Journal of Chemical Physics*, 2003. **118**(1): p. 337-339.
[67] Mante, P.A., C.C. Chen, Y.C. Wen, H.Y. Chen, S.C. Yang, Y.R. Huang, I.J. Chen, Y.W. Chen, V. Gusev, M.J. Chen, J.L. Kuo, J.K. Sheu, and C.K. Sun, Probing Hydrophilic Interface of Solid/Liquid-Water by Nanoultrasonics. *Scientific Reports*, 2014. **4**.

[68] Ge, S., Y. Gu, and M. Chen, A molecular dynamics simulation on the convective heat transfer in nanochannels. *Molecular Physics*, 2014.
[69] Khare, R., P. Keblinski, and A. Yethiraj, Molecular dynamics simulations of heat and momentum transfer at a solid-fluid interface: Relationship between thermal and velocity slip. *International Journal of Heat and Mass Transfer*, 2006. **49**(19-20): p. 3401-3407.
[70] Li, Z.G., Surface effects on friction-induced fluid heating in nanochannel flows. *Physical Review E*, 2009. **79**(2).
[71] Liu, C., H.B. Fan, K. Zhang, M.M.F. Yuen, and Z.G. Li, Flow dependence of interfacial thermal resistance in nanochannels. *Journal of Chemical Physics*, 2010. **132**(9).
[72] Nagayama, G. and P. Cheng, Effects of interface wettability on microscale flow by molecular dynamics simulation. *International Journal of Heat and Mass Transfer*, 2004. **47**(3): p. 501-513.
[73] Bernardi, S., B.D. Todd, and D.J. Searles, Thermostating highly confined fluids. *J Chem Phys*, 2010. **132**(24): p. 244706.
[74] De Luca, S., B.D. Todd, J.S. Hansen, and P.J. Daivis, A new and effective method for thermostatting confined fluids. *J Chem Phys*, 2014. **140**(5): p. 054502.
[75] Rafiee, J., X. Mi, H. Gullapalli, A.V. Thomas, F. Yavari, Y.F. Shi, P.M. Ajayan, and N.A. Koratkar, Wetting transparency of graphene. *Nature Materials*, 2012. **11**(3): p. 217-222.
[76] Raj, R., S.C. Maroo, and E.N. Wang, Wettability of Graphene. *Nano Letters*, 2013. **13**(4): p. 1509-1515.
[77] Shih, C.J., M.S. Strano, and D. Blankschtein, Wetting translucency of graphene. *Nature Materials*, 2013. **12**(10): p. 866-869.
[78] Shih, C.J., Q.H. Wang, S.C. Lin, K.C. Park, Z. Jin, M.S. Strano, and D. Blankschtein, Breakdown in the Wetting Transparency of Graphene. *Physical Review Letters*, 2012. **109**(17).
[79] Yang, H., J. Heo, S. Park, H.J. Song, D.H. Seo, K.E. Byun, P. Kim, I. Yoo, H.J. Chung, and K. Kim, Graphene Barristor, a Triode Device with a Gate-Controlled Schottky Barrier. *Science*, 2012. **336**(6085): p. 1140-1143.
[80] Caplan, M.E., A. Giri, and P.E. Hopkins, Analytical model for the effects of wetting on thermal boundary conductance across solid/classical liquid interfaces. *Journal of Chemical Physics*, 2014. **140**(15).
[81] Giri, A. and P.E. Hopkins, Spectral analysis of thermal boundary conductance across solid/classical liquid interfaces: A molecular dynamics study. *Applied Physics Letters*, 2014. **105**(3).
[82] Carey, V.P., Liquid-vapor phase-change phenomena : an introduction to the thermophysics of vaporization and condensation processes in heat transfer equipment. Series in chemical and mechanical engineering1992, Washington, D.C.: Hemisphere Pub. Corp. xvii, 645 p.
[83] L., N.C., Mémoire sur les lois du mouvement des fluides. *Mem. Acad. Sci. Inst. Fr.*, 1823. **6**: p. 389-416.
[84] Zhang, H.W., Z.Q. Zhang, Y.G. Zheng, and H.F. Ye, Corrected second-order slip boundary condition for fluid flows in nanochannels. *Physical Review E*, 2010. **81**(6).

[85] Kapitza, P.L., The study of heat transfer in helium II. *Journal of Physics-Ussr*, 1941. **4**(1-6): p. 181-210.
[86] Swartz, E.T. and R.O. Pohl, Thermal-Boundary Resistance. *Reviews of Modern Physics*, 1989. **61**(3): p. 605-668.
[87] Pollack, G.L., Kapitza Resistance. *Reviews of Modern Physics*, 1969. **41**(1): p. 48-&.
[88] Barisik, M. and A. Beskok, Temperature dependence of thermal resistance at the water/silicon interface. *International Journal of Thermal Sciences*, 2014. **77**: p. 47-54.
[89] Delhommelle, J. and P. Millie, Inadequacy of the Lorentz-Berthelot combining rules for accurate predictions of equilibrium properties by molecular simulation. *Molecular Physics*, 2001. **99**(8): p. 619-625.
[90] Ochedowski, O., G. Begall, N. Scheuschner, M. El Kharrazi, J. Maultzsch, and M. Schleberger, Graphene on Si(111)7x7. *Nanotechnology*, 2012. **23**(40).
[91] Tayran, C., Z. Zhu, M. Baldoni, D. Selli, G. Seifert, and D. Tomanek, Optimizing Electronic Structure and Quantum Transport at the Graphene-Si(111) Interface: An Ab Initio Density-Functional Study. *Physical Review Letters*, 2013. **110**(17).
[92] Xu, Y., K.T. He, S.W. Schmucker, Z. Guo, J.C. Koepke, J.D. Wood, J.W. Lyding, and N.R. Aluru, Inducing Electronic Changes in Graphene through Silicon (100) Substrate Modification. *Nano Letters*, 2011. **11**(7): p. 2735-2742.
[93] Nijmeijer, M.J.P., C. Bruin, A.F. Bakker, and J.M.J. Vanleeuwen, Wetting and Drying of an Inert Wall by a Fluid in a Molecular-Dynamics Simulation. *Physical Review A*, 1990. **42**(10): p. 6052-6059.
[94] Leroy, F., D.J.V.A. dos Santos, and F. Muller-Plathe, Interfacial Excess Free Energies of Solid-Liquid Interfaces by Molecular Dynamics Simulation and Thermodynamic Integration. *Macromolecular Rapid Communications*, 2009. **30**(9-10): p. 864-870.
[95] Werder, T., J.H. Walther, R.L. Jaffe, T. Halicioglu, and P. Koumoutsakos, On the water-carbon interaction for use in molecular dynamics simulations of graphite and carbon nanotubes. *Journal of Physical Chemistry B*, 2003. **107**(6): p. 1345-1352.
[96] Jaffe, R.L., P. Gonnet, T. Werder, J.H. Walther, and P. Koumoutsakos, Water-carbon interactions - 2: Calibration of potentials using contact angle data for different interaction models. *Molecular Simulation*, 2004. **30**(4): p. 205-216.
[97] Walther, J.H., T. Werder, R.L. Jaffe, P. Gonnet, M. Bergdorf, U. Zimmerli, and P. Koumoutsakos, Water-carbon interactions III: The influence of surface and fluid impurities. *Physical Chemistry Chemical Physics*, 2004. **6**(8): p. 1988-1995.
[98] Scocchi, G., D. Sergi, C. D'Angelo, and A. Ortona, Wetting and contact-line effects for spherical and cylindrical droplets on graphene layers: A comparative molecular-dynamics investigation. *Physical Review E*, 2011. **84**(6): p. 061602.
[99] Vanzo, D., D. Bratko, and A. Luzar, Wettability of pristine and alkyl-functionalized graphane. *Journal of Chemical Physics*, 2012. **137**(3).
[100] Li, X.Y., L. Li, Y. Wang, H. Li, and X.F. Bian, Wetting and Interfacial Properties of Water on the Defective Graphene. *Journal of Physical Chemistry C*, 2013. **117**(27): p. 14106-14112.
[101] Weijs, J.H., A. Marchand, B. Andreotti, D. Lohse, and J.H. Snoeijer, Origin of line tension for a Lennard-Jones nanodroplet. *Physics of Fluids*, 2011. **23**(2).

[102] Peng, H., G.R. Birkett, and A.V. Nguyen, The impact of line tension on the contact angle of nanodroplets. *Molecular Simulation*, 2014. **40**(12): p. 934-941.
[103] Barisik, M. and A. Beskok, Wetting characterisation of silicon (1,0,0) surface. *Molecular Simulation*, 2013. **39**(9): p. 700-709.
[104] Schimmele, L. and S. Dietrich, Line tension and the shape of nanodroplets. *European Physical Journal E*, 2009. **30**(4): p. 427-430.
[105] Wu, Y.B. and N.R. Aluru, Graphitic Carbon-Water Nonbonded Interaction Parameters. *Journal of Physical Chemistry B*, 2013. **117**(29): p. 8802-8813.
[106] Driskill, J., D. Vanzo, D. Bratko, and A. Luzar, Wetting transparency of graphene in water. *Journal of Chemical Physics*, 2014. **141**(18).
[107] Taherian, F., V. Marcon, N.F.A. van der Vegt, and F. Leroy, What Is the Contact Angle of Water on Graphene? *Langmuir*, 2013. **29**(5): p. 1457-1465.
[108] Taherian, F., F. Leroy, and N.F.A. van der Vegt, Interfacial Entropy of Water on Rigid Hydrophobic Surfaces. *Langmuir*, 2013. **29**(31): p. 9807-9813.
[109] Garcia, R., K. Osborne, and E. Subashi, Validity of the "Sharp-Kink Approximation" for water and other fluids. *Journal of Physical Chemistry B*, 2008. **112**(27): p. 8114-8119.
[110] Li, Z.T., Y.J. Wang, A. Kozbial, G. Shenoy, F. Zhou, R. McGinley, P. Ireland, B. Morganstein, A. Kunkel, S.P. Surwade, L. Li, and H.T. Liu, Effect of airborne contaminants on the wettability of supported graphene and graphite. *Nature Materials*, 2013. **12**(10): p. 925-931.
[111] Fowkes, F.M. and W.D. Harkins, The state of monolayers adsorbed at the interface solid-aqueous solution. *Journal of the American Chemical Society*, 1940. **62**: p. 3377-3386.
[112] Morcos, I., On contact angle and dispersion energy of the cleavage graphite/water system. *Journal of Colloid and Interface Science*, 1970. **34**(3): p. 469–471.
[113] Schrader, M.E., Ultrahigh-Vacuum Techniques in the Measurement of Contact Angles .5. Leed Study of the Effect of Structure on the Wettability of Graphite. *Journal of Physical Chemistry*, 1980. **84**(21): p. 2774-2779.
[114] Lai, C.Y., T.C. Tang, C.A. Amadei, A.J. Marsden, A. Verdaguer, N. Wilson, and M. Chiesa, A nanoscopic approach to studying evolution in graphene wettability. *Carbon*, 2014. **80**: p. 784-792.
[115] Wei, Y.Y. and C.Q. Jia, Intrinsic wettability of graphitic carbon. *Carbon*, 2015. **87**: p. 10-17.
[116] Egatz-Gomez, A., R. Majithia, C. Levert, and K.E. Meissner, Super-wetting, wafer-sized silicon nanowire surfaces with hierarchical roughness and low defects. *Rsc Advances*, 2012. **2**(30): p. 11472-11480.
[117] Shin, Y.J., Y.Y. Wang, H. Huang, G. Kalon, A.T.S. Wee, Z.X. Shen, C.S. Bhatia, and H. Yang, Surface-Energy Engineering of Graphene. *Langmuir*, 2010. **26**(6): p. 3798-3802.
[118] Rafiee, J., M.A. Rafiee, Z.Z. Yu, and N. Koratkar, Superhydrophobic to Superhydrophilic Wetting Control in Graphene Films. *Advanced Materials*, 2010. **22**(19): p. 2151-+.
[119] Kim, G.T., S.J. Gim, S.M. Cho, N. Koratkar, and I.K. Oh, Wetting-Transparent Graphene Films for Hydrophobic Water-Harvesting Surfaces. *Advanced Materials*, 2014. **26**(30): p. 5166-5172.

[120] Israelachvili, J.N. and G.E. Adams, Direct Measurement of Long-Range Forces between 2 Mica Surfaces in Aqueous Kno3 Solutions. *Nature*, 1976. **262**(5571): p. 773-776.
[121] Vinogradova, O.I., Coagulation of Hydrophobic and Hydrophilic Solids under Dynamic Conditions. *Journal of Colloid and Interface Science*, 1995. **169**(2): p. 306-312.
[122] Craig, V.S.J., C. Neto, and D.R.M. Williams, Shear-dependent boundary slip in an aqueous Newtonian liquid. *Physical Review Letters*, 2001. **87**(5).
[123] Vinogradova, O.I., H.J. Butt, G.E. Yakubov, and F. Feuillebois, Dynamic effects on force measurements. I. Viscous drag on the atomic force microscope cantilever. *Review of Scientific Instruments*, 2001. **72**(5): p. 2330-2339.
[124] Vinogradova, O.I. and G.E. Yakubov, Dynamic effects on force measurements. 2. Lubrication and the atomic force microscope. *Langmuir*, 2003. **19**(4): p. 1227-1234.
[125] Honig, C.D.F. and W.A. Ducker, No-slip hydrodynamic boundary condition for hydrophilic particles. *Physical Review Letters*, 2007. **98**(2).
[126] Lumma, D., A. Best, A. Gansen, F. Feuillebois, J.O. Radler, and O.I. Vinogradova, Flow profile near a wall measured by double-focus fluorescence cross-correlation. *Physical Review E*, 2003. **67**(5).
[127] Xue, Y.H., Y. Wu, X.W. Pei, H.L. Duan, Q.J. Xue, and F. Zhou, How Solid-Liquid Adhesive Property Regulates Liquid Slippage on Solid Surfaces? *Langmuir*, 2015. **31**(1): p. 226-232.
[128] Lichter, S., A. Roxin, and S. Mandre, Mechanisms for Liquid Slip at Solid Surfaces. *Physical Review Letters*, 2004. **93**(8).
[129] Lichter, S., A. Martini, R.Q. Snurr, and Q. Wang, Liquid Slip in Nanoscale Channels as a Rate Process. *Physical Review Letters*, 2007. **98**(22).
[130] Babu, J.S. and S.P. Sathian, Combining molecular dynamics simulation and transition state theory to evaluate solid-liquid interfacial friction in carbon nanotube membranes. *Physical Review E*, 2012. **85**(5).
[131] Bocquet, L. and J.-L. Barrat, Hydrodynamic boundary conditions, correlation functions, and Kubo relations for confined fluids. *Physical Review E*, 1994. **49**(4): p. 3079-3092.
[132] Pop, E., Energy Dissipation and Transport in Nanoscale Devices. *Nano Research*, 2010. **3**(3): p. 147-169.
[133] Cahill, D.G., W.K. Ford, K.E. Goodson, G.D. Mahan, A. Majumdar, H.J. Maris, R. Merlin, and P. Sr, Nanoscale thermal transport. *Journal of Applied Physics*, 2003. **93**(2): p. 793-818.
[134] Cahill, D.G., P.V. Braun, G. Chen, D.R. Clarke, S.H. Fan, K.E. Goodson, P. Keblinski, W.P. King, G.D. Mahan, A. Majumdar, H.J. Maris, S.R. Phillpot, E. Pop, and L. Shi, Nanoscale thermal transport. II. 2003-2012. *Applied Physics Reviews*, 2014. **1**(1).
[135] Maruyama, S. and K. T., A Study on Thermal Resistance over a Solid-Liquid Interface by the Molecular Dynamics Method. *Thermal Science & Engineering*, 1999. **7**(1): p. 63-68.
[136] Barrat, J.-L. and F. Chiaruttini, Kapitza resistance at the liquid—solid interface. *Molecular Physics*, 2003. **101**(11): p. 1605-1610.

[137] Xue, L., P. Keblinski, S.R. Phillpot, S.U.S. Choi, and J.A. Eastman, Effect of liquid layering at the liquid-solid interface on thermal transport. *International Journal of Heat and Mass Transfer*, 2004. **47**(19-20): p. 4277-4284.
[138] Torii, D., T. Ohara, and K. Ishida, Molecular-Scale Mechanism of Thermal Resistance at the Solid-Liquid Interfaces: Influence of Interaction Parameters Between Solid and Liquid Molecules. *Journal of Heat Transfer*, 2010. **132**(1): p. 012402.
[139] Kim, B.H., A. Beskok, and T. Cagin, Molecular dynamics simulations of thermal resistance at the liquid-solid interface. *J Chem Phys*, 2008. **129**(17): p. 174701.
[140] Murad, S. and I.K. Puri, Thermal transport across nanoscale solid-fluid interfaces. *Applied Physics Letters*, 2008. **92**(13).
[141] Merabia, S., S. Shenogin, L. Joly, P. Keblinski, and J.L. Barrat, Heat transfer from nanoparticles: a corresponding state analysis. *Proc Natl Acad Sci U S A*, 2009. **106**(36): p. 15113-8.
[142] Goicochea, J.V., M. Hu, B. Michel, and D. Poulikakos, Surface Functionalization Mechanisms of Enhancing Heat Transfer at Solid-Liquid Interfaces. *Journal of Heat Transfer-Transactions of the Asme*, 2011. **133**(8).
[143] Pham, A., M. Barisik, and B. Kim, Pressure dependence of Kapitza resistance at gold/water and silicon/water interfaces. *J Chem Phys*, 2013. **139**(24): p. 244702.
[144] Barisik, M. and A. Beskok, Temperature dependence of thermal resistance at the water/silicon interface. *International Journal of Thermal Sciences*, 2014. **77**: p. 47-54.
[145] Balasubramanian, G., S. Banerjee, and I.K. Puri, Unsteady nanoscale thermal transport across a solid-fluid interface. *Journal of Applied Physics*, 2008. **104**(6): p. 064306.
[146] Carlborg, C.F., J. Shiomi, and S. Maruyama, Thermal boundary resistance between single-walled carbon nanotubes and surrounding matrices. *Physical Review B*, 2008. **78**(20).
[147] Shi, Z., M. Barisik, and A. Beskok, Molecular dynamics modeling of thermal resistance at argon-graphite and argon-silver interfaces. *International Journal of Thermal Sciences*, 2012. **59**: p. 29-37.
[148] Frenkel, D. and F. Smit, Understanding Molecular Simulation: From Algorithms to Applications. 2 ed2001: Academic Press. 664.
[149] Tersoff, J., Empirical Interatomic Potential for Silicon with Improved Elastic Properties. *Physical Review B*, 1988. **38**(14): p. 9902-9905.
[150] Tersoff, J., Modeling Solid-State Chemistry - Interatomic Potentials for Multicomponent Systems. *Physical Review B*, 1989. **39**(8): p. 5566-5568.
[151] Hockney, R.W. and J.W. Eastwood, Computer Simulation Using Particles1988, New York, NY: CRC Press. 540.
[152] Hoover, W.G., Canonical Dynamics - Equilibrium Phase-Space Distributions. *Physical Review A*, 1985. **31**(3): p. 1695-1697.
[153] Nose, S., A Molecular-Dynamics Method for Simulations in the Canonical Ensemble. *Molecular Physics*, 1984. **52**(2): p. 255-268.
[154] Plimpton, S., Fast Parallel Algorithms for Short-Range Molecular-Dynamics. *Journal of Computational Physics*, 1995. **117**(1): p. 1-19.

[155] Humphrey, W., A. Dalke, and K. Schulten, VMD: Visual molecular dynamics. *Journal of Molecular Graphics & Modelling*, 1996. **14**(1): p. 33-38.
[156] Guillot, B., A reappraisal of what we have learnt during three decades of computer simulations on water. *Journal of Molecular Liquids*, 2002. **101**(1-3): p. 219-260.
[157] Chaplin, M. *http://www1.lsbu.ac.uk/water/water_models.html*. 2015.
[158] Sirk, T.W., S. Moore, and E.F. Brown, Characteristics of thermal conductivity in classical water models. *J Chem Phys*, 2013. **138**(6): p. 064505.
[159] Gonzalez, M.A. and J.L.F. Abascal, The shear viscosity of rigid water models. *Journal of Chemical Physics*, 2010. **132**(9).
[160] Orsi, M., Comparative assessment of the ELBA coarse-grained model for water. *Molecular Physics*, 2014. **112**(11): p. 1566-1576.
[161] Berendsen, H.J.C., J.R. Grigera, and T.P. Straatsma, The Missing Term in Effective Pair Potentials. *Journal of Physical Chemistry*, 1987. **91**(24): p. 6269-6271.
[162] Ryckaert, J.-P., G. Ciccotti, and H.J.C. Berendsen, Numerical integration of the cartesian equations of motion of a system with constraints: molecular dynamics of n-alkanes. *Journal of Computational Physics*, 1977. **23**(3): p. 327-341.
[163] Shen, M., P.K. Schelling, and P. Keblinski, Heat transfer mechanism across few-layer graphene by molecular dynamics. *Physical Review B*, 2013. **88**(4).
[164] de Ruijter, M.J., T.D. Blake, and J. De Coninck, Dynamic wetting studied by molecular modeling simulations of droplet spreading. *Langmuir*, 1999. **15**(22): p. 7836-7847.
[165] Petravic, J. and P. Harrowell, On the equilibrium calculation of the friction coefficient for liquid slip against a wall. *Journal of Chemical Physics*, 2007. **127**(17).
[166] Hansen, J.S., B.D. Todd, and P.J. Daivis, Prediction of fluid velocity slip at solid surfaces. *Physical Review E*, 2011. **84**(1).
[167] Bocquet, L. and J.L. Barrat, On the Green-Kubo relationship for the liquid-solid friction coefficient. *J Chem Phys*, 2013. **139**(4): p. 044704.
[168] Huang, K. and I. Szlufarska, Green-Kubo relation for friction at liquid-solid interfaces. *Physical Review E*, 2014. **89**(3).
[169] Nagayama, G., T. Tsuruta, and P. Cheng, Molecular dynamics simulation on bubble formation in a nanochannel. *International Journal of Heat and Mass Transfer*, 2006. **49**(23-24): p. 4437-4443.
[170] Ikeshojia, T. and B. Hafskjoldb, Non-equilibrium molecular dynamics calculation of heat conduction in liquid and through liquid-gas interface. *Molecular Physics*, 1994. **81**(2): p. 251-261.
[171] MullerPlathe, F., A simple nonequilibrium molecular dynamics method for calculating the thermal conductivity. *Journal of Chemical Physics*, 1997. **106**(14): p. 6082-6085.
[172] Barisik, M. and A. Beskok, Boundary treatment effects on molecular dynamics simulations of interface thermal resistance. *Journal of Computational Physics*, 2012. **231**(23): p. 7881-7892.
[173] Ramos-Alvarado, B., S. Kumar, and G.P. Peterson, Wettability of graphitic-carbon and silicon surfaces: MD modeling and theoretical analysis. *Journal of Chemical Physics*, 2015. **143**(4).

[174] Egatz-Gomez, A., R. Majithia, C. Levert, and K.E. Meissner, Super-wetting, wafer-sized silicon nanowire surfaces with hierarchical roughness and low defects. *Rsc Advances*, 2012. **2**(30): p. 11472-11480.
[175] Lindsay, L. and D.A. Broido, Optimized Tersoff and Brenner empirical potential parameters for lattice dynamics and phonon thermal transport in carbon nanotubes and graphene (vol 81, 205441, 2010). *Physical Review B*, 2010. **82**(20).
[176] Poularikas, A.D., Signals and Systems Primer with MATLAB. 1 ed. Electrical Engineering & Applied Signal Processing Series, ed. C. Press2006: CRC Press. 676.
[177] Liang, Z. and P. Keblinski, Slip length crossover on a graphene surface. *Journal of Chemical Physics*, 2015. **142**(13).
[178] Duda, J.C., T.S. English, E.S. Piekos, W.A. Soffa, L.V. Zhigilei, and P.E. Hopkins, Implications of cross-species interactions on the temperature dependence of Kapitza conductance. *Physical Review B*, 2011. **84**(19).
[179] Martin, P., Z. Aksamija, E. Pop, and U. Ravaioli, Impact of Phonon-Surface Roughness Scattering on Thermal Conductivity of Thin Si Nanowires. *Physical Review Letters*, 2009. **102**(12).